NANOSTRUCTURED THIN FILMS FOR SOLID OXIDE FUEL CELLS

A Dissertation

by

JONGSIK YOON

Submitted to the Office of Graduate Studies of
Texas A&M University
in partial fulfillment of the requirements for the degree of

DOCTOR OF PHILOSOPHY

December 2008

Major Subject: Electrical Engineering

NANOSTRUCTURED THIN FILMS FOR SOLID OXIDE FUEL CELLS

A Dissertation

by

JONGSIK YOON

Submitted to the Office of Graduate Studies of
Texas A&M University
in partial fulfillment of the requirements for the degree of

DOCTOR OF PHILOSOPHY

Approved by:

Chair of Committee,	Haiyan Wang
Committee Members,	Jim Ji
	Frederick Strieter
	Xinghang Zhang
Head of Department,	Costas N. Georghiades

December 2008

Major Subject: Electrical Engineering

ABSTRACT

Nanostructrued Thin Films for Solid Oxide Fuel Cells.

(December 2008)

Jongsik Yoon, B.S., Yonsei University, Korea;

M.S., University of Southern California

Chair of Advisory Committee: Dr. Haiyan Wang

The goals of this work were to synthesize high performance perovskite based thin film solid oxide fuel cell (TF-SOFC) cathodes by pulsed laser deposition (PLD), to study the structural, electrical and electrochemical properties of these cathodes and to establish structure-property relations for these cathodes in order to further improve their properties and design new structures.

Nanostructured cathode thin films with vertically-aligned nanopores (VANP) were processed using PLD. These VANP structures enhance the oxygen-gas phase diffusivity, thus improve the overall TF-SOFC performance. $La_{0.5}Sr_{0.5}CoO_3$ (LSCO) and $La_{0.4}Sr_{0.6}Co_{0.8}Fe_{0.2}O_3$ (LSCFO) were deposited on various substrates (YSZ, Si and pressed $Ce_{0.9}Gd_{0.1}O_{1.95}$ (CGO) disks). Microstructures and properties of the nanostructured cathodes were characterized by transmission electron microscope (TEM), high resolution TEM (HRTEM), scanning electron microscope (SEM) and electrochemical impedance spectroscopy (EIS) measurements.

A thin layer of vertically-aligned nanocomposite (VAN) structure was deposited in between the CGO electrolyte and the thin film LSCO cathode layer for TF-SOFCs. The VAN structure consists of the electrolyte and the cathode materials in the composition of $(CGO)_{0.5}(LSCO)_{0.5}$. The self-assembled VAN nanostructures contain highly ordered alternating vertical columns formed through a one-step thin film deposition using a PLD technique. These VAN structures significantly increase the interface area between the electrolyte and the cathode as well as the area of active triple phase boundary (TPB), thus improving the overall TF-SOFC performance at low temperatures, as low as 400^{o}C, demonstrated by EIS measurements. In addition, the binary VAN interlayer could act as the transition layer that improves the adhesion and relieves the thermal stress and lattice strain between the cathode and the electrolyte.

The microstructural properties and growth mechanisms of CGO thin film prepared by PLD technique were investigated. Thin film CGO electrolytes with different grain sizes and crystal structures were prepared on single crystal YSZ substrates under different deposition conditions. The effect of the deposition conditions such as substrate temperature and laser ablation energy on the microstructural properties of these films are examined using XRD, TEM, SEM, and optical microscope. CGO thin film deposited above 500 ºC starts to show epitaxial growth on YSZ substrates. The present study suggests that substrate temperature significantly influences the microstructure of the films especially film grain size.

DEDICATION

To my beloved parents and brother, to my teachers, and to my friends

ACKNOWLEDGMENTS

I would like to express my deepest gratitude to my graduate advisor Dr. Haiyan Wang for her invaluable advice, financial support, and especially for her academic guidance. I am deeply indebted to my advisor whose help, stimulating suggestions and encouragement helped me in all the time of research and writing this dissertation. Dr. Haiyan Wang is one of the best professors that I have met in my life. She sets high standards for her students and she encourages and guides us to meet those standards. Her teachings greatly inspired me during my graduate study.

I would like to thank Profs. Frederick Strieter, Jim Ji, Xing Cheng, and Xinghang Zhang for serving as my committee members. I acknowledge their helpful comments and suggestions in shaping this dissertation. I wish to thank Dr. Adriana Serquis in the Centro Atomico Bariloche, Argentina for the helpful discussion about impedance analysis and valuable contributions to the papers we wrote together. I wish to take this opportunity to acknowledge Dr. Susan Wang at the University of Houston for sharing her profound knowledge and experience about microstructure characterization and impedance measurement. I also thank Joon Hwan Lee for his late night presence whenever I did PLD depositions. I thank my girl friend Soonyoung for her constant support.

I would like to acknowledge financial support from the *Air Force Office of Scientific Research* and also from the State of Texas through the *Texas Engineering Experiment Station*. I am grateful to the University of Houston and Centro Atomico Bariloche, Argentina research group for measuring the ASR, and impedance data.

Finally, I want to thank my friends in the thin film characterization group, Ickchan Kim, Roy Araujo, Zhenxing Bi, Joyce Wang, Joonhwan Lee, Chen-Fong Cho, Song Du, and Sungmee Cho, for making my graduate years enjoyable and memorable. The facilities and resources provided by the Electrical and Computer Engineering Department, Texas A&M University, are gratefully acknowledged. I thank Texas A&M University, University of Southern California and Yonsei University for educating me in various ways.

TABLE OF CONTENTS

Page

LIST OF TABLES

LIST OF FIGURES

FIGURE Page

FIGURE Page

FIGURE Page

CHAPTER I

INTRODUCTION

This chapter presents the motivation and objectives of the research in this dissertation. Solid oxide fuel cell (SOFC) is one of the most promising energy sources which are clean and highly efficient. However due to the high operating temperature, developing cost effective SOFCs is a challenging task. Literature review in this chapter summarizes historical developments of the fuel cells with special emphasis on SOFC. Finally, future work is proposed.

1.1 Overview

Fuel cells are one of the most efficient, environmentally clean and effective energy sources which convert chemical energy of a fuel gas directly into electrical energy. It is now well understood that global warming is taking place mainly due to carbon dioxide (CO_2) gas emission from fossil fuel combustion. In the past century, global temperature has increased at a rate near 0.6°C/century [1]. For the past 25 years this trend has increased dramatically. According to the US Department of Energy (DoE), by 2015 world carbon emissions are expected to increase 54% more than 1990 emission and this

---

This dissertation follows the style and format of the Applied Surface Science.

will increase the global temperature by 1.7 to 4.9°C over the period 1990–2100, as shown in Fig. 1.1 [2].

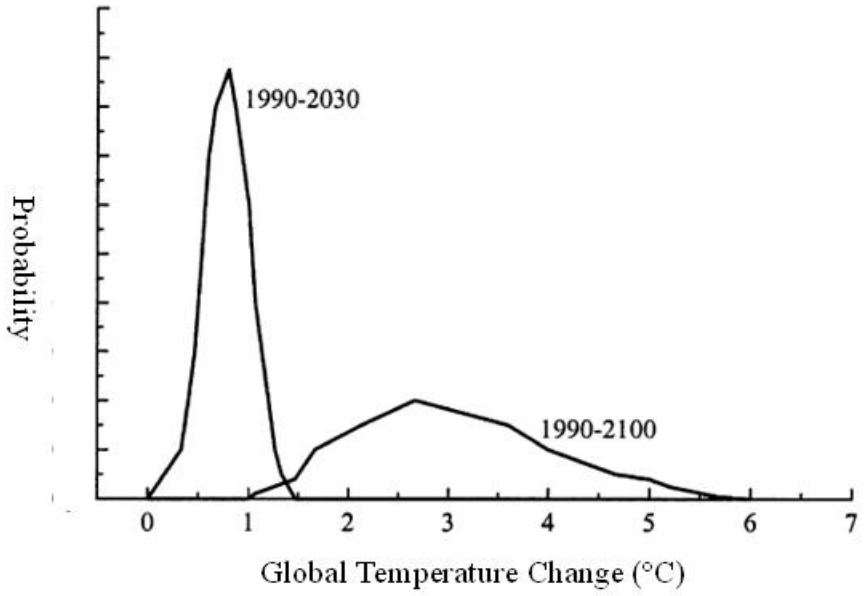

Fig.1.1. Global–mean temperature change over the period of 1990–2100 and 1990–2030

Problems with conventional fossil fuel energy are related not only to global warming but also to environmental concerns such as air pollution, acid precipitation, emission of radioactive waste, and ozone depletion. It is expected that world population will reach 12 billions by 2050 therefore; global demand for energy services is expected to increase ten times more than now by 2050, while energy supply can only be increased by 1.5 to 3 times [3]. As world wide oil supplies decrease (Fig. 1.2 [4]), the development of new energy sources which are renewable and environmentally clean will become more

important. In response to the demanding need for a cleaner and reusable energy sources, some potential solutions have emerged such as conserving energy through improving energy efficiency, reducing the fossil fuel consumption, and increasing the supply of environmental friendly energy sources such as fuel cells. Solid oxide fuel cells (SOFCs) are one of the most promising candidates which can meet most of the above conditions.

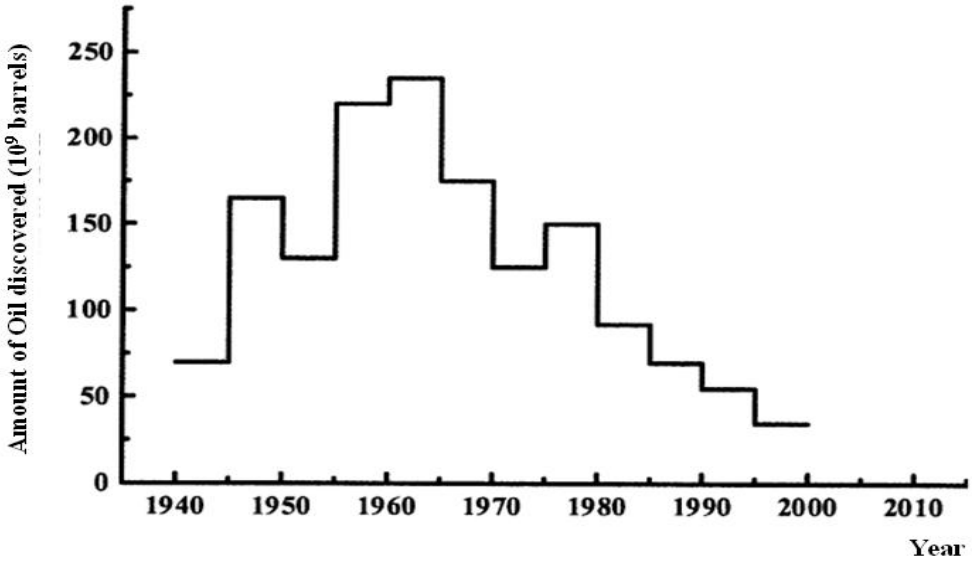

Fig.1.2. Volume of oil discovered world wide every five years

1.2 Fuel Cells

The operating mechanisms of fuel cells are electrochemical reaction between reactants to generate electricity. It does not require intermediate energy conversion steps unlike other

electric power generation devices such as internal combustion engines. Because of its simple direct energy conversion mechanism it shows much higher efficiency than conventional method. Fuel cells can operate as long as both fuel and oxidant are supplied to the electrodes.

1.2.1 Origin of Fuel Cells

Fuel cells have been known for more than 160 years and have been researched intensively since World War II. Alessandro Volta (1745–1827) was the first scientist who first observed the electrical phenomena. J. W. Ritter (1776–1810), also known as the founder of the electrochemistry, has continued to develop the understanding of electricity. In 1802, Sir Humphrey Davy created a simple fuel cell based upon a C/H_2O and $NH_3/O_2/C$ compounds delivering a week electric power. The fuel cell principle was discovered by Christan Friedrich Schonbein during 1829 to 1868. Sir William Grove (1811–1896) developed an improved wet cell battery (‘Grove cell’) in 1838. This cell type is based on the backward reaction of the electrolysis of water [5]. Nernst discovered solid oxide electrolytes much later in 1899 and this introduced ceramic fuel cells [6]. Ludwig Mond (1839–1909) spent most of his time in developing industrial chemical technology. Mond and his assistant Carl Langer developed a hydrogen–oxygen fuel cell that generated 6 amps per square foot of the electrode at 0.73 V. The theoretical understanding of how fuel cells operate was decribed by V. Friedrich Wilhelm Oswald (1853-1932). During the first half of the 20^{th} century Emil Baur (1873–1944) researched

many different types of fuel cells. Baur's work includes high temperature molten silver electrolyte devices and a unit that used a solid electrolyte of clay and metal oxides. Francis Thomas Bacon (1904–1992) initiated alkali electrolyte fuel cells research in the late 1930s. Since 1945, three research groups (US, Germany and the former USSR) took over the studies on some principal types of generators by improving their technologies for industrial development purposes [7]. In 1960, NASA supported hydrogen based fuel cell research and successfully developed to supply power to the electrical systems on the Apollo. Although it was discovered over 160 years ago with all the facts that it is environmentally clean and the efficiency is as high as over 70% only now fuel cell technology is close to commercialization because of its high cost components and high operating temperature. However due to the extensive research for the last two decades on materials science and process technologies now we are on the verge of its realization as a alternate, clean energy source. Today, fuel cells are widely adopted in many applications such as space shuttle, transportation, possible use as portable power system, remote power generation and intermediate size distributed power generation.

1.2.2 Fuel Cell Types

There is now many different types of fuel cells available. The main differences among them are their chemical characteristics of the electrolytes in the cell. However, the basic operating principle of all types of fuel cell is the same. Depending on the electrolyte, either protons or oxide ions are transported through the electrolyte. Electrons transported

through external circuit connecting anode and cathode. There are mainly five types of fuel cells as summarized in Table 1.1 [8]. All these five types of fuel cells share the same basic operating components. They are all composed of two electrodes separated by an electrolyte.

Table 1.1

Summary of the five main types of fuel cells and their characteristics.

Fuel Cell Type	Electrolyte	Operating Temperature	Fuel	Oxidant	Electrical Efficiency
Polymer Electrolyte Membrane (PEM)	Solid organic Polymer poly-perfluorosulfonic acid	50-100°C	Less pure carbon from hydrocarbon or methanol	O_2/air	53-58% (transportation) 23-35% (stationary)
Alkaline (AFC)	Aqueous solution of potassium hydroxide soaked in a matrix	90-100°C	Pure hydrogen or hydrazine liquid methanol	O_2/air	50-55%
Phosphoric Acid (PAFC)	Liquid phosphoric acid soaked in a matrix	150-200°C	Hydrogen from hydrocarbon or alcohol	O_2/air	40-50%
Molten Carbonate (MCFC)	Liquid solution of lithium, sodium, or potassium carbonates, soaked in a matrix	600-700°C	Hydrogen, carbon monoxide, natural gas, propane, diesel	O_2/air/CO_2	50-60%
Solid Oxide (SOFC)	Solid gadolinium oxide or zirconium oxide with small amount of cerium or yttrium	600-1000°C	Natural gas, hydrogen, or propane	O_2/air	45-60%

All these five types of fuel cells share the same basic operating components. They are all composed of two electrodes separated by an electrolyte. Ions move in from one direction and this direction depends on the electrolyte. While the electrons flow through an external circuit connected between the electrodes. Each type of fuel cell is characterized by the electrolyte. It is generally considered that the two types of fuel cells, the polymer electrolyte membrane (PEM) and the solid oxide fuel cell, are most likely to succeed in commercial application.

The most obvious difference between the different types of fuel cell is their operating temperature. Molten carbonate and solid oxide fuel cells have the highest operating temperatures of 800–1000 °C compared to the much lower operating temperatures of around 100 °C for alkaline and PEM fuel cells and around 200 °C for phosphoric acid fuel cells (PAFC). PEMFCs have low operating temperature and can be used in cars and portable devices. SOFCs are competitive to other fuel cell types because they are the most efficient fuel cell type currently under development, they have fuel flexibility, and cost effective when a certain industrially mature process technology such as thin film process is applied. They are also quiet systems which can be used as indoor applications.

1.3 Solid Oxide Fuel Cells (SOFCs)

SOFCs can be characterized with its solid ceramic components especially solid electrolyte which is a composite oxide. SOFCs consist of the cathode where oxygen is

reduced to oxygen ions, electrolyte where those oxygen ions pass through toward the anode, and the anode where the oxygen ions react with fuel. This electrochemical reaction mechanism inside the fuel cell is shown schematically in Fig. 1.3. The theoretical maximum efficiency is over 80%. Multiple cells can be connected to produce larger output power. Conventional SOFCs operate at high temperatures between 800-1000 °C. This high operating temperature allows internal reforming, promotes rapid electro catalysis without the need for precious metals such as platinum, and produces high quality heat which can be used for combined heat processor to increase the efficiency even further [9]. The hydrocarbon fuel is catalytically converted into carbon monoxide and hydrogen in the SOFC and then electrochemically reacts to produce CO_2 and water at the anode. But there is some draw back in using high temperature environment. Only a few materials can withstand that high temperature and most of them are economically not suitable for mass production.

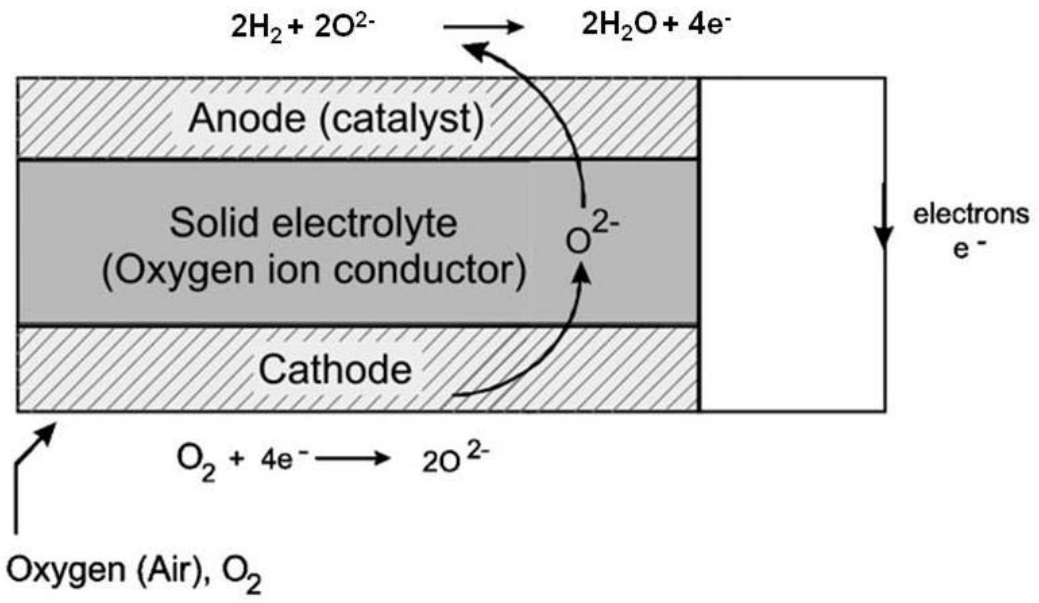

Fig.1.3. Schematic diagram of SOFC operating on hydrogen fuel

1.3.1 History of SOFCs

Solid oxide electrolytes were first investigated by Emil Baur and his colleague H. Preis in the late 1930s using lanthanum, yttrium, cerium, tungsten, and zirconium oxide. The operating temperature of the first ceramic fuel cell was 1000°C in 1937 [10]. Davtyan experimented on increasing mechanical stability and ionic conductivity of electrolyte by adding sand to a mixture of sodium carbonate, tungsten trioxide, and soda glass in the 1940s. However, Davtyan's composition ended up with unwanted chemical reactions and short life cycles. In 1959, a discussion of fuel cells in New York announced that the problems of solid electrolytes include relatively low ionic conductivity inside of the

electrolyte, melting, and short-circuiting between electrodes due to conductivity of electrolyte at high temperature.

More recently, advances in materials technology and climbing energy prices have opened the possibilities that SOFC can replace some fossil fuel based power generation. In 1962 researchers at Westinghouse, for example, experimented on cells which are using zirconium oxide and calcium oxide as electrolyte materials. Another example is a 140 kW peak power SOFC cogeneration system, supplied by Siemens Westinghouse, which is presently operating in the Netherlands. This system has been operated for over 16,000 hours and becoming the longest running fuel cell in the world [11]. DoE and Siemens Westinghouse are planning to place a 1 MW fuel cell cogeneration plant in near future [12].

1.3.2 SOFC Operating Mechanism

SOFCs differ in many respects from other fuel cell technologies. First, they are composed of all solid-state materials. Second, the normal operating temperature range of SOFCs is 600-1000°C which is significantly higher than other major types of fuel cells. Third, because its component materials are all ceramics there is no need for precious metals. Many different shapes of SOFCs are possible such as tubular, disk, and planar shapes. Among those different shapes planar shape cells are adopted more recently by

many developers and widely used today by industries. Schematic SOFC operating mechanism is shown in Fig.1.4.

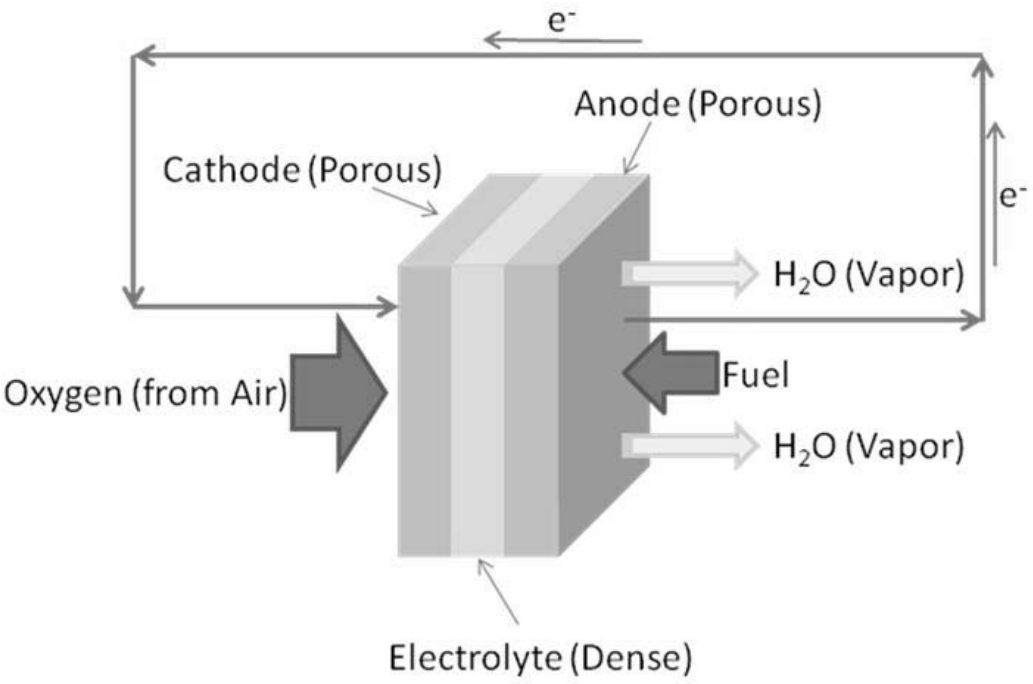

Fig.1.4. Schematic diagram showing the general operating principles of SOFC

Fuel is supplied to the anode side and oxygen is supplied to the cathode side of the fuel cell. At the anode surface oxidation of oxygen ions occurs in the process of reaction between fuel gas and oxygen ions, thereby electrons are released. In this process oxygen concentration gradient created. This oxygen concentration gradient created across the electrolyte attracts oxygen ions from the air side to the anode across the electrolyte. Electrical connection between the cathode and the anode allows electrons to flow from

the anode to the cathode and oxygen ion conductions from cathode to anode through electrolyte maintains overall electrical charge balance. The only byproduct of this process is a pure water vapor (H_2O) and heat in case of hydrogen fuel, as illustrated in Table 1.2. The SOFC reactions at each electrode are summarized in table 1.2. Unlike other types of fuel cells moderately high operating temperature eliminates the need for an expensive external reformer.

Table 1.2

The electrochemical reactions on each electrode in SOFC

Electrode	Chemical Reaction
Cathode	$O_2 + 4e^- \rightarrow 2\ O^{2-}$
Anode	(1) $H_2 + O^{2-} \rightarrow H_2O + 2e^-$,
	(2) $CO + O^{2-} \rightarrow CO_2 + 2e^-$,
	(3) $CH_4 + 4O^{2-} \rightarrow 2H_2O + CO_2 + 8e^-$ (*for hydrocarbon fuels*)

1.4 Materials for SOFC Components

SOFCs are composed of an anode, a cathode, and a electrolyte. The main function of the electrodes is working as a reaction site of the reactants (fuel or oxygen) along with the electrolyte without being consumed or corroded. Electrochemical reaction site is limited

only to the triple phase boundary (TPB) where electrode, fuel, and electrolyte come into contact. Supplied fuel gas disperses through the anode and frees out electrons to the anode when they meet oxygen ions at the anode side and form water molecules. Oxygen molecules enter into the cathode side and combine with electrons supplied from anode side to form oxygen ions then pass across the electrolyte to meet the fuel gas at the anode side. The electrolyte is where the main power loss of SOFC occurs because of its low ionic conductivity at low temperature. It also acts as a gas tight membrane which prevents the fuel gas and oxygen from intermixing. Another important function of electrolyte is the separation of the two electrodes. If current flows between the two electrodes through the electrolyte considerable power loss of the fuel cell can happen. It can either be an hydrogen ion conductor or a oxygen ion conductor as shown in Figs. 1.5 and 1.6 respectively.

High operating temperature of the SOFC places strict limitations on its component materials used as electrolytes, anodes, cathodes, and interconnects. Each component must meet multiple requirements and must have more than one function. For example, all components must be chemically stable in reducing and oxidizing conditions as well as physically stable to avoid cracking or delamination during operation. Currently, the most widely used electrode materials are perovskite type materials where “A” and “B” sites are doped with divalent cations for increased performance as shown in Fig. 1.7a.

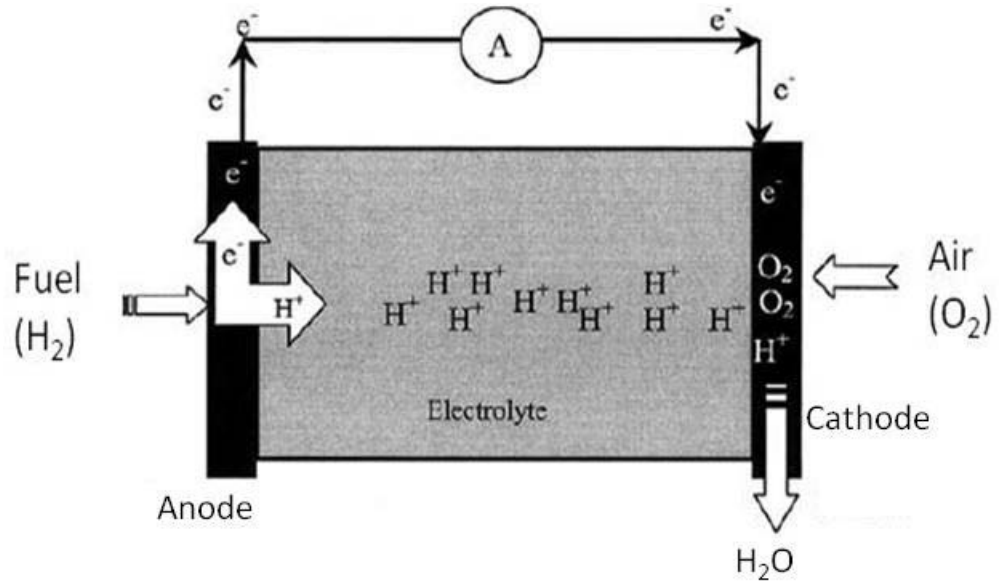

Fig.1.5. Schematic diagram of SOFC based on proton (hydrogen ion) conductors

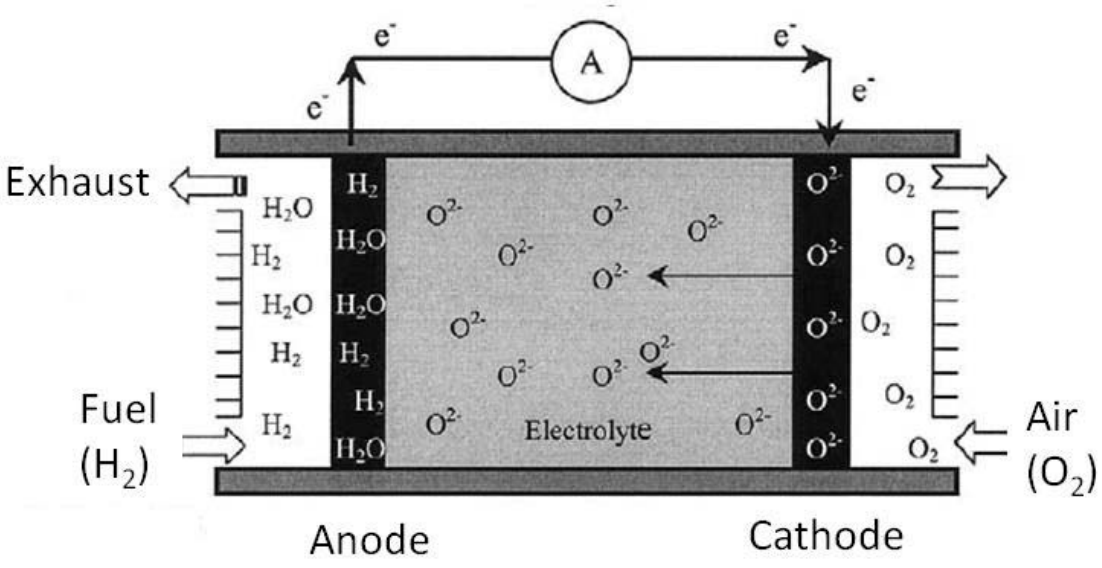

Fig.1.6. Schematic diagram of SOFC with oxygen ion conductors

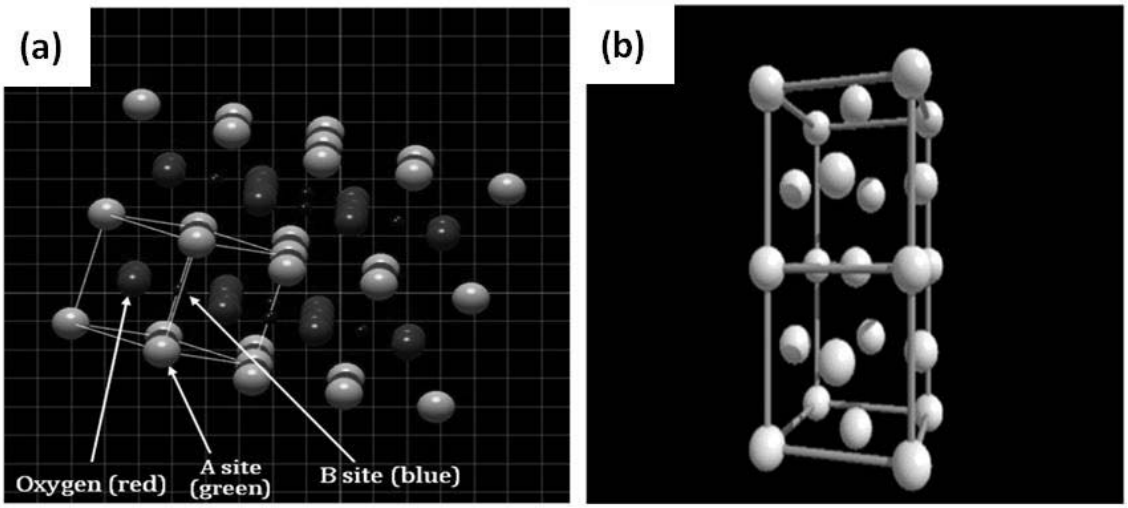

Fig.1.7. (a) Perovskite (ABO_3) structured electrode and (b) face centered cubic structure of CGO electrolyte

On the other hand YSZ and CGO electrolyte has face centered cubic (FCC) structure as shown in Fig. 1.7b. At room temperature the crystal structure of zirconium oxide is tetragonal. Once heated the crystal structure of zirconium oxide undergoes structural transformation from tetragonal to cubic via monoclinic intermediate structure. By adding small amount of yttria zirconium oxide can be stabilized into cubic structure. Physical properties of selected SOFC component materials are described in Table 1.3.

Table 1.3

Physical properties of selected SOFC components

Parameter	Electrode		Electrolyte	
	$La_{0.2}Sr_{0.8}Co_{0.2}Fe_{0.8}O_{3-\delta}$ (LSCFO)	$La_{0.5}Sr_{0.5}CoO_3$ (LSCO)	CGO	YSZ
Lattice Structure	Perovskite	Perovskite	FCC	FCC
Lattice Parameter (a)	0.389nm	0.381nm	1.08(2x5.04)nm	1.02(2x5.1)nm
Melting Point	1350ºC<	1850ºC<	2100ºC<	2600ºC<

1.4.1 Cathode

Because of the high operating temperature of the SOFCs there is strict constraint for cathode materials to meet. Only some oxides and noble metals can satisfy this constraint but because of the high price and short life cycle, noble metals are not suitable for practical applications as cathode materials [13]. The choice of the electrode material mainly depends on its applications such as operating temperature range, cell configurations, its other component materials, and fabrication method. And they should be porous in structure in order to facilitate rapid mass transport of reactant gas to the reaction site. Numerous doped oxides have been studied for zirconia based SOFCs and the most common materials for cathodes are perovskite-type lanthanum strontium manganite, $La_{1-x}Sr_xMnO_3$ (LSMO) [14, 15]. LSMO shows excellent thermal expansion

coefficient match with zirconia electrolytes such as YSZ and provide good performance in the operating temperatures range of 800-1000°C.

Cation vacancies inside LSMO enable the conductivity of LSMO and this conductivity can be improved by using lower valence ions as dopants for either the A or B sites. The alkaline earth metals, magnesium, calcium, and strontium have all been used as dopants, together with nickel [14, 16]. The conductivity of LSMO varies with strontium content, with an optimum strontium level. La^{3+} can be replaced with divalent cations to increase the electric conductivity through the increased Mn^{4+} ratio inside and the conduction happens by small polaron jumping. Although LSMO is an excellent cathode materials LSMO is not chemically compatible with zirconia electrolyte in high temperature applications because above 1300 °C manganese can diffuse into the zirconia electrolyte and diminish the performance both of the cathode and the electrolyte [17].

Doped lanthanum cobaltite, $LaCoO_3$ (LCO) is another promising perovskite material that has been widely studied and used as a cathode material for SOFCs [14, 18]. LCO also shows very good p-type conductivity and at high temperatures it shows a large oxygen deficiency [19]. By doping a divalent cation such as strontium on the La^{3+} site $La_{1-x}Sr_xCoO_3$ (LSCO) the conductivity can be improved [20]. Further improvements in performance have been found by substituting iron on the cobalt site such as $La_{1-x}Sr_xCo_{1-y}Fe_yO_3$ (LSCFO). LSCO generally shows even higher conductivity than LMO under the same conditions [17, 18]. For even higher overall fuel cell performance composite

electrodes can be used. Composite electrodes consist of electrode and electrolyte materials. The addition of electrolyte materials to the cathode has improves the electrochemical performance of the cathode at lower temperature regime by increasing the effective reaction sites [21].

1.4.2 Anode

Anode side is where reduction of fuel is taking place and because of this condition metals can be used as anode materials. But the anode metals must be oxidizing resistant because the composition of the fuel can be changed during the operation. Similar to cathodes, anodes can also be fabricated as composite mixtures of electrolyte materials and nickel oxide (NiO) but unlike the electrolyte the anode must have porous structure and this should be maintained during high temperature operation [21]. Those electrolyte materials mixed with nickel oxide can inhibit sintering of the nickel particles and can ease the thermal expansion coefficient mismatch between the anode and the electrolyte.

In addition, the anode must be electrically conducting to be functional as an electrode. The nickel content in nickel/solid electrolyte cermet decide conductivity of the Ni cermet anode. The minimum amount of nickel necessary for electrical conductivity is about 30 vol%. Below this amount the conductivity of the anode is about the same as that of the solid electrolyte which is electronically not conducting. Above this amout the conductivity increases by about three orders of magnitude. The conductivity of the anode

depends on its microstructure, the size and particle size distribution of the solid electrolyte and nickel particles, and the inter-connectivity of the nickel particles in the cermet. The proportion of nickel used in the anode cermet also influences the thermal expansion mismatch between the solid electrolyte and the anode. As the nickel content in nickel/yttria stabilized zirconia increases the thermal expansion coefficient of a nickel/yttria stabilized zirconia cermet increases linearly. This increased thermal expansion coefficient will cause greater thermal mismatch at the interface of electrolyte and electrode. This will result in cracking of the electrolyte or delamination of the anode during the fabrication or thermal cycling.

Because of all these drawbacks of Ni cermet, electrically conducting oxides, which are stable under both oxidizing and reducing conditions, have been actively studied in recent years as potential alternative anode materials to nickel [22, 23]. The use of oxide anodes would solve many problems associated with nickel cermet anodes used in direct reforming SOFCs such as sulfur poisoning, carbon deposition, and sintering. Nickel oxide formation also can be avoided. As possible anode materials $LaCrO_3$ (LCO), strontium titanate, SrTiO3 (STO), doped LCO, and doped STO have been studied. In the case of LCO calcium (Ca), strontium (Sr) and titanium (Ti) dopants have been used. From recent studies anodes which are capable of direct hydrocarbon reforming without the need for any oxidant have been developed [24, 25]. One of these anodes is copper-based anode.

There is currently much interest in developing alternative anode materials to the nickel/YSZ cermet. Nickel-ceria cermet anodes is being studied by many researchers for gadolinia doped ceria based SOFCs as well as for zirconia based SOFCs. Nickel/ceria cermet anodes have been shown to give sufficiently good performance in especially ceria based SOFCs operating at temperatures around 500 °C. Ceria has also been added to nickel/YSZ anodes to improve both the electrical performance and the resistance to carbon deposition.

1.4.3 Electrolyte

Major power loss and efficiency degradation of SOFC is closely related to electrolyte characteristics and the operating temperature is strongly depends on the ionic conductivity and the thickness of the electrolyte layer. There are two possible approaches to these problems. Finding alternate electrolyte materials which have higher ionic conductivity is one solution and the other one would be decreasing electrolyte thickness. To decrease the electrolyte layer thickness some of the current SOFCs adopted electrode supporting configuration. In this case the minimum dense electrolyte thickness that can be produced reliably is 10 to 15μm and the typical thickness is 30 μm.

Current technology employs yttria stabilized zirconia (Y_2O_3 stabilized ZrO_2 or YSZ, $(ZrO_2)_{0.92}(Y_2O_3)_{0.08}$) as solid electrolyte materials because of its low material cost, high temperature stability and moderately high oxygen ion conductivity from intermediate to

high temperature regime. YSZ shows pure oxygen ion conduction with no electrical conductivity. The ZrO_2 crystal structure includes two oxide ions for every zirconium ion but in Y_2O_3 crystal structure there are only 1.5 oxide ions to every yttrium ion. This results in vacancies in the crystal structure where oxide ions are missing. Using these vacancies oxide ions generated from the TPB at the cathode side can pass through electrolyte to reach the anode side. The most commonly used zirconia stabilizing dopants are Y_2O_3, Sc_2O_3, CaO, MgO, and certain rare earth oxides such as Nd_2O_3, Sm_2O_3. But despite of its relatively high oxygen ion conductivity it is not suitable for low temperature applications below 600°C furthermore it shows interface diffusion and second phase formation problem after some cycles. Gadolinia-doped ceria (CGO) exhibits superb performance in low temperature regime (400-600°C). However in a reducing high temperature environment in anode ceria undergoes partial reduction. This reduction leads to electronic conduction between anode and cathode and significantly lowers the efficiency of the SOFC. It can also bring an undesirable structural change at the interface. Other oxide based ceramic electrolytes candidates which can replace CGO for even low temperature operation are samarium doped cerium oxide $(Ce_{0.85}Sm_{0.15})O_{1.925}$ (SDC), and Calcium doped cerium $(Ce_{0.88}Ca_{0.12})O_{1.88}$ (CDC)[26].

1.5 SOFC Cell Configurations

Many different kinds of SOFC configurations have been adapted to increase power output and efficiency. The maximum voltage output a single cell can generate is 0.5 to

0.9 volts of DC electricity with maximum efficiency of 60% since they are small in size and considerable ohmic loss occurs inside of the cell. To address maximum power output stacked cell configuration has been used. There are two major types in SOFC, a tubular type and a planar type as shown in Fig. 1.8 and 1.9.

In tubular configuration the tube itself consists of the electrolyte and electrodes. Fuel gas usually supplied to the outside of the pipe and the oxygen through the inside. Each tube is connected through interconnect with each other to increase output power.

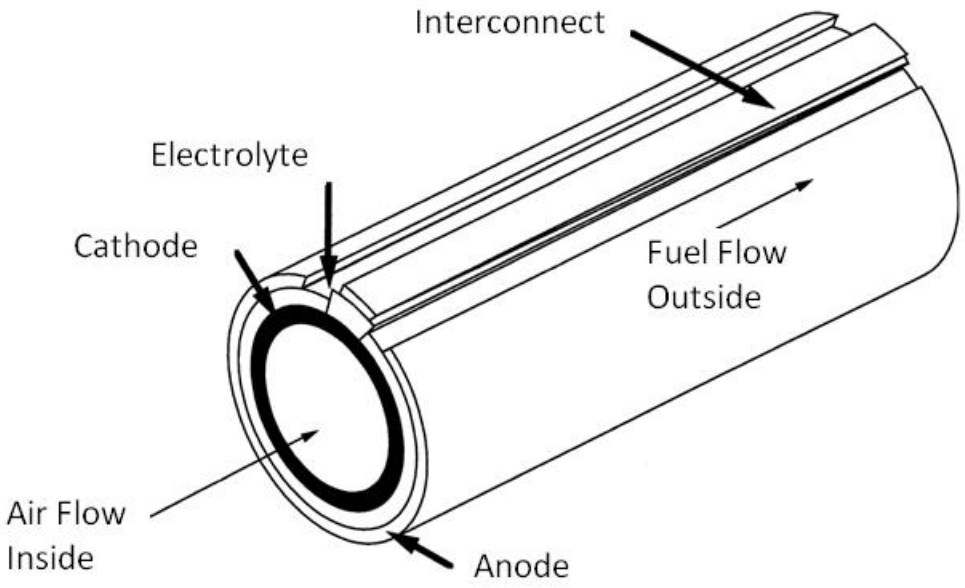

Fig.1.8. Tubular type SOFC configuration

The most common configuration among several different stack designs is the planar SOFC as illustrated in Fig. 1.9. Main advantages of this planar design over other types are its easiness of manufacture and low ohmic resistance of electrolyte which will bring less energy loss during operation. During operation fuel gas and air flow down channels in the bipolar interconnects and diffuse into electrodes.

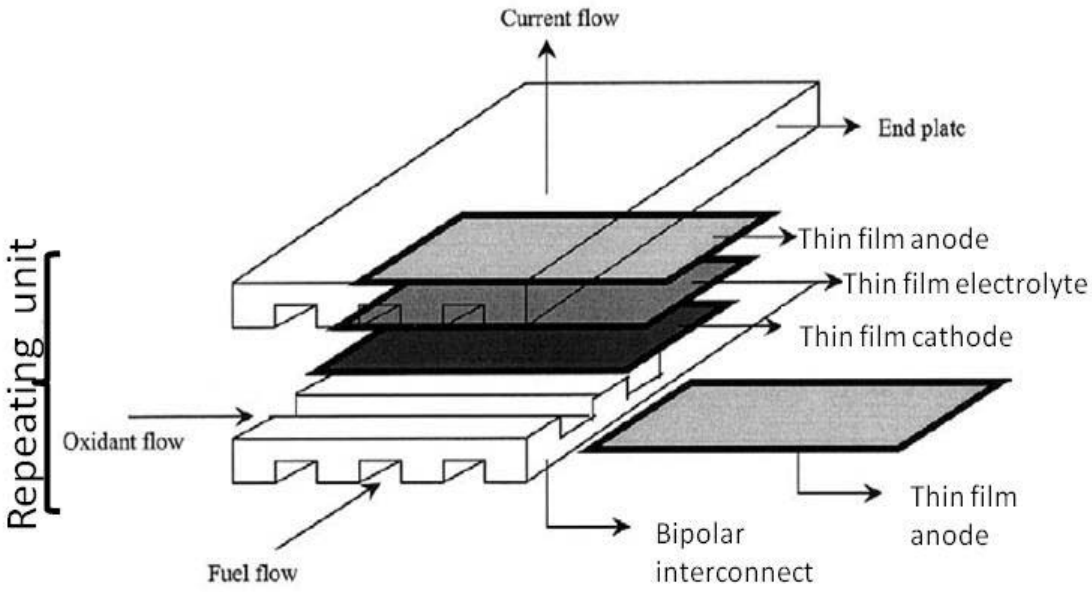

Fig.1.9. Planar unit cell design of SOFC single stack with bipolar interconnects

For low to intermediate temperature (400-600°C) applications thin film configuration has been developed. Cost effective thin film fabrication processes can be applied to this configuration. Completed cells can then be integrated into a manifold that would protect and support the thin film structure, supply fuel and oxidizer, and collect the current [27].

To produce desired amounts of power output, single cell elements are assembled into a stack. Stack is a basic building block of the fuel cell power plant in which all the cell components are stacked with interconnecting plates between them. Interconnects are generally made of doped lanthanum chromate $LaCrO_3$, particularly suitable from its high electronic conductivity, its stability in the fuel cell environment and its compatibility with other cell components. Interconnects are shaped to allow flow of the hydrogen and oxygen to the repeating unit. Early SOFCs used doped $CoCr_2O_4$ as interconnect material [28]. Recently, $YCrO_3$ compound, having great stability in the fuel cell environment, has been evaluated as an alternative material to $LaCrO_3$ [29]. However, all these materials are not cost effective. The main problem for using low cost interconnect material, such as high temperature alloys are a thermal expansion mismatch with other SOFC components, cost, and long term instability during cell lifetime. Various efforts have been made to reduce SOFC operating temperature so that low cost materials can be used along with flexible cell design. Lowering cell operating temperature can bring many advantages other than cost. At low operating temperature thermal stress between electrodes and electrolyte due to different thermal expansion coefficient can be greatly relieved. The cells are connected in electrical series to build a desired output voltage and can be configured in many different forms depending on their applications. The total voltage is determined by the number of cells in a stack and the surface area determines the total current.

1.6 SOFC Limitations and Thin Film Approach

Due to high operating temperature the only performance issues related to SOFCs are ohmic losses during charge transfer process across components and between component interfaces [30]. Around 1000°C SOFCs are the most fuel-efficient energy sources but this high temperature place constraints on selecting fuel cell materials and this increases cost. Moreover this high operating temperature decreases the cell lifetime significantly due to high thermal stress. High operating temperature also means longer start up time. For these constraints lowering operating temperature is the best solution to ensure structural integrity of SOFC, expand life time, and reduce cost since in reduced temperature environment cheaper interconnect, gasket, and cell component materials can be utilized.

For many years researchers have been working on reducing this high operating temperature of SOFCs without diminishing performance. Since the cell performance is very sensitive to operating temperature 10% drop in temperature will bring 12% drop in overall performance, due to the increase in internal resistance to the oxygen ion conduction [31]. Replacing cell component materials with good ionic conductivity at low temperature has been a solution to this problem. Recently researchers are focusing on reducing resistance and increasing ionic conductivity of electrolyte by applying thin film technology. Thin film process is a mature, proven, and cost effective technology. Thin film SOFC also has other benefits in miniaturization and stacking than easiness of

process. Schematic diagram of three possible types of thin film SOFC configurations are shown in Figure 1.10. In order to ensure the structural integrity of the fuel cell at least one component of the SOFC should be thicker than 30μm.

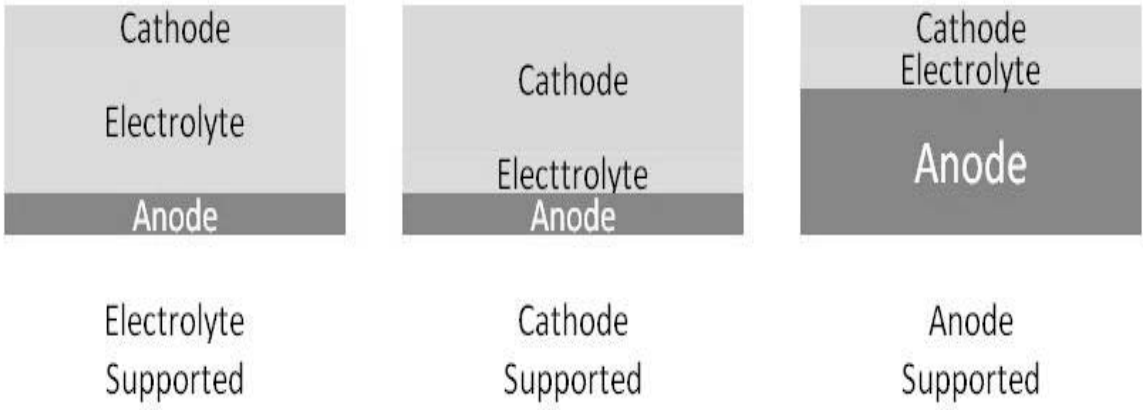

Fig.1.10. Schematic diagram of thin film SOFC

1.7 Future Work for SOFCs

The global SOFC making company continues to make very significant improvements in basic fuel cell design. These changes in cell composition and design have resulted in improved power densities [32]. Higher power densities enable fuel cells to be lighter, smaller, and cost effective. If ultimate cost goals of $1000/kW can be realized SOFCs could be suitable for small scale residential power applications [33]. Table 1.4 shows the SOFC application goals of California for the period of 2005–2010 with a power density

target of 300 mW/cm^2 and an installation of 50,000 units/year [34]. The main technical challenges in developing low temperature SOFCs are insuring ionic conductivity in electrolyte during low temperature operation. Researchers are making an effort in developing suitable materials which can replace the current high temperature materials and engineering microstructures of the materials to improve the efficiency.

Table 1.4

SOFC application goals until year 2010

Parameter	Target	Goal	Notes
Capital cost, installed ($/kW)	800	400	2005 - 2010 5000 units per year
Power degradation	Less than 1% /hr	Less than 0.5% /hr	
Power density (mW/ cm^2)	300	500	bigger than 4-cell stack with 25 cm^2 or larger electrode

One such an effort is modifying the electrode-electrolyte interface through microstructure engineering and developing a thin film electrolyte which can decrease the cell resistance, double the power output and significantly reduce the cost of SOFCs. Another important approach is improving materials properties of current materials by using various dopants. There is also a current effort in integrating the SOFCs and developing a novel stacking geometry. The success of low temperature SOFC which

operates directly on hydrocarbon fuel can open an important new opportunity for making simple, cost-effective power plants [35].

1.8 Summary

Constantly growing world population strongly demands alternate energy sources. SOFCs appear to be one of the most promising energy sources for the future because of their high efficiencies and fuel flexibility. Their efficiency and performance has been proven by successful operation throughout the world. Efficiencies of over 70% are possible these days if they are combined with heat processors.

Despite the fact that SOFC is the ideal energy source for the future, its high operating temperature delays its technological advances. Profound efforts have been made in reducing temperature and this will lead to reduce cell resistance and regain power loss at low temperature regime. One of such efforts are finding alternate materials such as gadolinia-doped ceria (CGO) or lanthanum gallate based structures for low temperature cell components and applying the current thin film technology to reduce electrolyte resistance such as ultra-thin dense, impermeable CGO electrolyte films. SOFC operating temperature can be lowered greatly by reducing electrolyte thickness since thin film electrolyte can perform well even at low temperature because of its increased ionic conductivity in thin film electrolyte and this will result in many other benefits such as longer cell life time and shorter start up time. Other benefits from using thin film

components can be found in cell design and configuration. Cell stacking is easier with thin film SOFC components and cell miniaturization is possible for the use of mobile applications.

CHAPTER II

RESEARCH METHODOLOGY

2.1 Pulsed Laser Deposition (PLD) Technique

Because of its narrow frequency bandwidth, coherence and high power density laser is used in many scientific research works and experiments especially in material processing. The laser beam is intense enough to vaporize the hardest and most heat resistant materials. Its high precision, reliability and spatial resolution enabled laser to be used widely in material processing industry. Thin film processing and micro patterning is some of the examples [36,37]. Apart from these, complex materials can be deposited onto desired substrates maintaining its original stoichiometric compositions of the target. This procedure is called Pulsed Laser Deposition (PLD).

In general, the method of pulsed laser deposition is simple in its procedure. Only limited numbers of parameters need to be controlled during the process. PLD utilizes small targets compared with other targets used in other thin film deposition techniques. By controlling the number of pulses and targets, a fine control of film thickness and multi layer film can be achieved. Thus a fast prototyping a new material system is a unique feature of PLD among other deposition methods. The most important feature of PLD is that the stoichiometry of the target can be reproduced in the deposited films. This is the result of non equilibrium process originated from an extremely high heating rate of the

target surface (108 K/s) due to high energy pulsed laser irradiation. It leads to the harmonious evaporation of the target compounds. And because of the high heating rate epitaxial film growth using PLD requires a much lower temperature than other mentioned film growth techniques [38].

In spite of mentioned advantages of PLD there are some drawbacks in using PLD technique. One of the major problems is the particulates deposition on the film. This happens because of surface boiling, expulsion of the liquid layer by shock wave recoil pressure and exfoliation. Such particulates will greatly affect the growth of the subsequent layers as well as the electrical properties of the film and should be eliminated [39]. Another problem is the substrate surface coverage of the plum which is generated by the adiabatic expansion of laser produced plasma. These features limit the use of PLD in mass production. Recently new techniques such as inserting a shadow mask to block the particulates and rotating both target and substrate in order to produce a larger uniform film, have been developed to overcome the PLD problems mentioned earlier.

Fig. 2.1 shows a schematic diagram of a typical experimental setup. The system consists of a multiple target holder and a substrate holder in a high vacuum chamber maintained by a turbo-molecular pump. The target consists of bulk material oriented at an angle of 45^{o} toward the incident laser beam. A high power laser is used as an external energy source to vaporize materials and to deposit thin films. A set of optical components is used to focus and raster the laser beam over the target surface. The evaporated material

is deposited onto a substrate facing target separated by the distance of 3 to 5cm. The substrate temperature can be varied from room temperature to 800^{o}C. The film microstructure depends on various parameters such as substrate temperature, laser energy density, pulse repetition rate, pressure inside the chamber, and substrate to target distance. The separation of the vacuum hardware and the evaporation method makes this technique so flexible that it can be easily adaptable to different operational modes without difficulties unlike the system with internally powered evaporation sources. Film growth can be carried out in a reactive environment containing any kind of gas with or without plasma excitation. It can also be operated in conjunction with other types of evaporation sources in a hybrid approach [40].

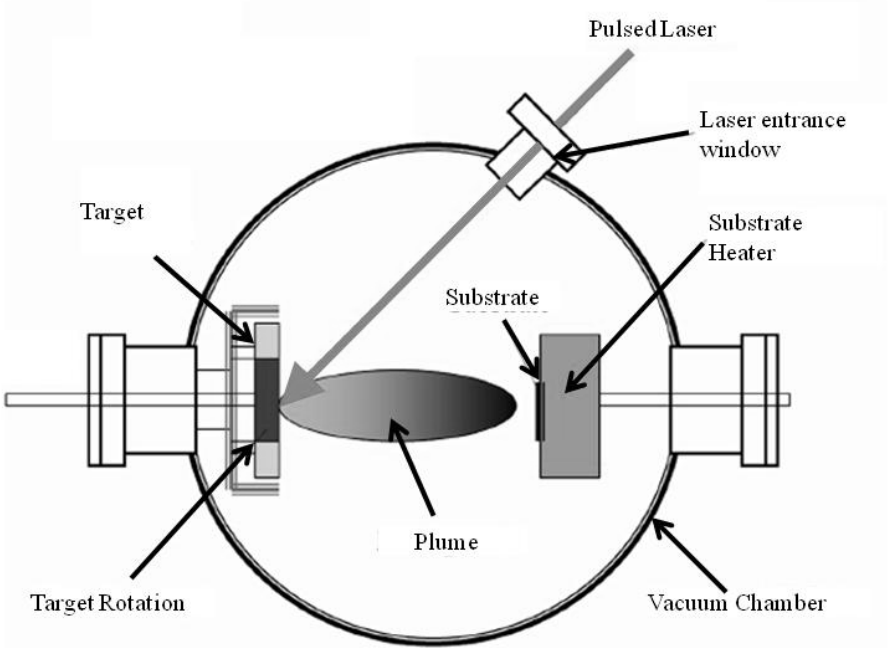

Fig.2.1. Schematic diagram of the pulsed laser deposition system

In contrast to the simple hardware set up, the laser-target interaction is a very complex physical phenomenon and it includes both equilibrium and nonequilibrium processes. The mechanism that leads to material ablation depends on laser characteristics, as well as the optical, topological, and thermodynamic property of target. When the laser energy is absorbed by a target surface, electromagnetic energy is converted first into electronic excitation and then into thermal, chemical, and even mechanical energy to cause evaporation, ablation, excitation, plasma formation, and exfoliation. Evaporations results in a 'plume' consisting of a mixture of energetic species including atoms, molecules, electrons, ions, clusters, micron sized solid particulates, and molten globules. Inside the dense plume the collision mean free path is very short. As a result, immediately after the laser irradiation, the plume rapidly expands into the vacuum from the target surface to form a nozzle jet with hydrodynamic flow characteristics. With the proper choice of the laser PLD can be used to grow thin film of any kind of material.

Each of the nanosecond laser pulse and target interaction can be divided into three stages as shown schematically in figure 2.2. Depending on the type of interaction of the laser beam with the target laser-target interactions can be categorized into three different regimes. First, interactions of the laser beam with the target materials which results in evaporation of the surface layers. Second, interaction of the evaporated material with the incident laser beam resulting in isothermal plasma formation and expansion, and the third, anisotropic adiabatic expansion of the plasma and subsequent deposition. The first

two interactions start with the laser pulse and continue through out the laser pulse duration. The third regime starts after the termination of the laser pulse [41].

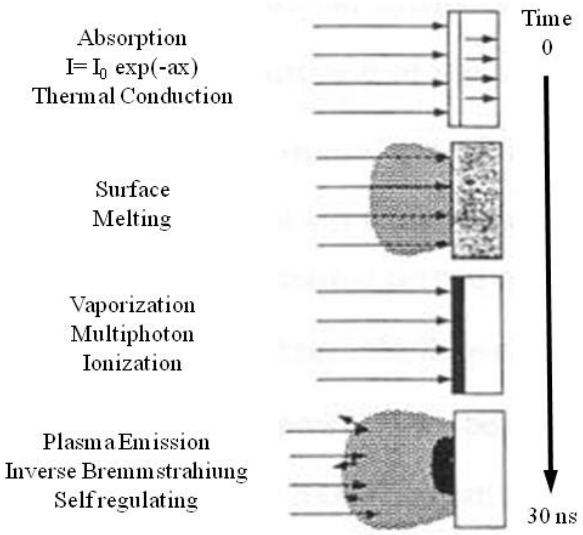

Fig.2.2. Schematic representation of the stages of laser target interactions during short pulse high power laser interaction with a solid [41]

2.1.1 Interaction of the Laser Beam with the Target

Surface layers exposed to intense heat of the high power nanosecond laser pulses results in melting and evaporation of the. Laser parameters such as pulse energy density (E), pulse duration (*t)*, wavelength (λ) and shape of the laser pulse and materials properties such as reflectivity, absorption coefficient, heat capacity, density, thermal conductivity decide the heating rate, melting and evaporation of the target material during pulsed

laser irradiation. The free carrier (hole) collisions provide the pathway of the phonon energy in the bulk surface. The heating and melting effects of pulsed laser irradiation on materials constitute a three dimensional heat flow problem. In nanosecond laser processing, the thermal diffusion distances are short, and the dimensions of the laser beam are large compared to the melt depth. Hence, the thermal gradients parallel to the interface are many orders of magnitude less than the thermal gradients normal to the interface. This makes the problem for heat flow during PLD one dimensional governed by:

$$\rho_{i(T)C_P(T)}\frac{\partial T(x,t)}{\partial t}=\frac{\partial}{\partial t}\left[K_i(T)\frac{\partial T(x,t)}{\partial x}\right]+I_0(t)\left[1-R(t)\right]e^{-a(t)x} \qquad (2.1)$$

Where x refers to the direction normal to the plane of the sample and t refers to the time. The subscripts i=1, 2 refer to the solid and liquid phase respectively. The terms $\rho_i(T)$ and $C_p(T)$ are respectively the temperature dependent density and thermal heat capacity per unit mass of the target material. $R(t)$ and $a(t)$ are the temperature dependent reflectivity and absorption coefficient of the material corresponding to laser wavelength. The term $I_0(t)$ is the time dependent incident laser intensity hitting the surface which depends on the intensity and shape of the laser pulse. The term K_i refers to thermal conductivities of the solid and liquid phases at the interface. The last term on the right hand side of the equation (2.1) is the heat generation term. Accurate numerical solution to this equation by finite method gives the evaporation characteristics of the pulsed laser irradiated

materials. Using this method, the thermal histories of the laser irradiated materials can be predicted. Thus the effects of the variations in the pulse energy density E, pulse duration t, and substrate temperature T on the maximum melt depths, solidification velocities and surface temperatures can be computed. Although the presence of a moving surface formed as a result of melting or evaporation, and time-dependent optical and material properties make the analytical solution difficult, simple energy balance considerations can be taken into account to assess the effects of interaction of the laser irradiation with the materials. By using energy balance method the amount of material evaporated per pulse can be calculated. The energy irradiated by the laser beam on the target is equal to the energy needed to vaporize the surface layers plus losses due to the thermal conduction by the substrate and the absorption by the plasma. The energy threshold E_{th} represents the minimum required energy above which appreciable evaporation is observed. Since the losses in plasma and substrate change with pulse energy density, E_{th} varies with energy density too. Thus the heat balance equation is given by:

$$\Delta x_i = \frac{(1-R)(E-E_{th})}{\Delta H + C_v \Delta T} \tag{2.2}$$

where Δx_i, R, ΔH, Cv and ΔT are the evaporated thickness, reflectivity, latent heat, volume heat capacity, and the maximum temperature rise, respectively. This equation is valid for conditions where the thermal diffusion distance ($\sqrt{2Dt}$) is larger then the absorption length, or attenuation distance of the laser beam in the target material ($1/a_t$).

In the above expression, D is the thermal diffusivity of the target, and t is the laser pulse duration. In equation (2.2) the energy threshold depends on laser wavelength, pulse duration, plasma losses, and the thermal and optical properties of the material.

2.1.2 Interaction of the Laser Beam with Evaporated Materials

The interaction of the high power laser beam with the bulk target materials leads to very high temperature (>2000K), resulting in emission of positive ions and electrons from the free surface. The emission of electrons and positive ions from a target surface increase with temperature exponentially. The thermionic emission of positive ions can be calculated by Langmuir-Saha equation:

$$i_+ / i_0 = \left(g_+ / g_0 \right) e^{\left[(\phi - I) kT \right]} \tag{2.3}$$

where i_+ and i_0 represent positive and neutral ion fluxes leaving the surface at temperature T. g_+ and g_0 are the statistical weights of the ionic and neutral states, Φ is the electron work function, and I is the ionization potential of the materials. The fraction of ionized species increases with the temperature since $I > \Phi$. The interaction of laser beam with evaporated plasma increases the plasma temperature even higher than the target surface temperature. The penetration and absorption of the laser beam by the plasma depend on the electron / ion density, temperature, and the laser wavelength. The

plasma frequency, $\nu_p = 8.9 \times 10^3 n_e^{0.5}$, where n_e is the electron concentration in the plasma decides the penetration or reflection of the incident laser beam. In order for the laser energy to be transmitted or absorbed the plasma frequency should be lower than the laser frequency. For example, for $XeCl_2$ excimer-laser with 308 nm wavelength the laser frequency is 9.74×10^{14} sec with critical electron density for reflection given by $n_e = 1.2 \times 10^{22}/cm^3$.

The material evaporated from the target is further heated by absorption of laser radiation. Although the laser evaporation for deposition of thin films occurs at much lower temperatures, the plasma temperatures are further increased by the absorption of incident laser beam. Different mechanisms become important in the ionization of the laser generated species such as impact ionization, photo ionization, thermal ionization and electronic excitation.

The primary absorption mechanism for plasma is the electron-ion collisions. The absorption occurs primarily by a process, which involves absorption of a photon by free electron. The absorption coefficient a_p of the plasma is given by:

$$\alpha_p = 3.69 \times 10^8 \left(z^3 n_i^2 / T^{0.5} \nu^3 \right) \left[1 - e^{\frac{-h\nu}{kT}} \right] \qquad (2.4)$$

where Z, n_i, and T are the average charge, ion density, and temperature of the plasma, reflectively, and h, k, and v are the Plank constant, Boltzmann constant, and frequency of the laser light respectively. The term $\left[1-e\frac{-h\nu}{kT}\right]$ in equation (2.4) represents the losses due to stimulated emission. For KrF excimer laser (λ=248nm), the exponential term becomes unity for T<<40,000K and can be approximately by hv/kT for T>>40,000K. The absorption term shows a $T^{0.5}$ dependence for low temperature (T<<40,000K for λ=248nm, T<<40,000K for λ=1.06nm) and $T^{1.5}$ for high temperatures. As it is seen, the heating of the evaporated materials depends on the concentration of the ionized species, plasma temperature, wavelength, plasma temperature, wavelength, pulse duration, etc.. Also the particle density in the plasma depends on the degree of ionization, evaporation rate, and the plasma expansion velocities. Because of the high expansion velocities of the leading plasma edge, the electron and ion densities decrease very rapidly with time. This makes the plasma transparent to the laser beam for larger distances away from the target surface. The inner edge of the plasma in a thin region close to the surface of the target it constantly absorbing laser radiation due to the constant augmentation of the plasma with evaporated particles. A schematic diagram of the laser interaction with the plasma target is shown in figure 2.3.

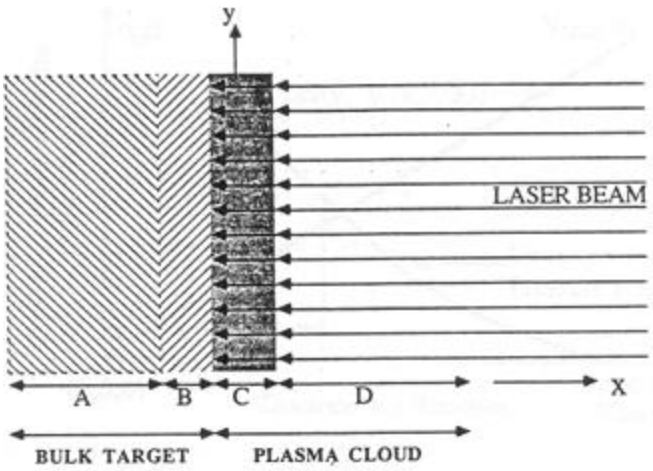

Fig.2.3. Schematic diagram representing the different phases present during irradiation of a laser on a bulk target: (A) unaffected bulk target, (B) evaporated target materials, (C) dense plasma absorbing the laser radiation, and (D) expanding plasma transparent to the laser beam [41]

The diagram shows four separate regions which can be distinguished during the laser pulse. Those are unaffected bulk target, evaporating target surface, area near the surface of the target absorbing the laser beam, and rapidly expanding outer edge which is transparent to the laser beam. A dynamic equilibrium exists between the plasma absorption and the rapid transfer of thermal energy into kinetic energy. These are two mechanisms controlling the isothermal temperature of the plasma. The initial dimensions of the plasma are in the millimeter range in the transverse direction, while they are less than 1μm in the perpendicular direction. In the isothermal regime and assuming an initial expansion velocity of 10^5-10^6 cm/sec, the perpendicular dimension of the plasma is in the order of 10 to 100μm at the end of a 30 nsec laser pulse. The large density gradients

cause the rapid plasma expansion in vacuum. The plasma absorbing the laser energy can be simulated as a HT-HP gas which is initially confined in small dimensions and is suddenly allowed to expand in a vacuum. The gas dynamic equations governing the expansion of the plasma consist of the equation of continuity and the equation of motion. The velocity, density, and the pressure profiles in the plasma are shown schematically in figure 2.4. It shows that the density is maximum while the velocity is minimum at the inner edge of the plasma. The plasma density and the pressure gradients decreases non linealy from the surface of the target while the velocity increases linearly. In the initial stages of expansion the acceleration is very high when the expansion velocities are low. When the expansion velocities increase, the acceleration starts to decrease and ultimately becomes zero, resulting in the elongated plasma shape.

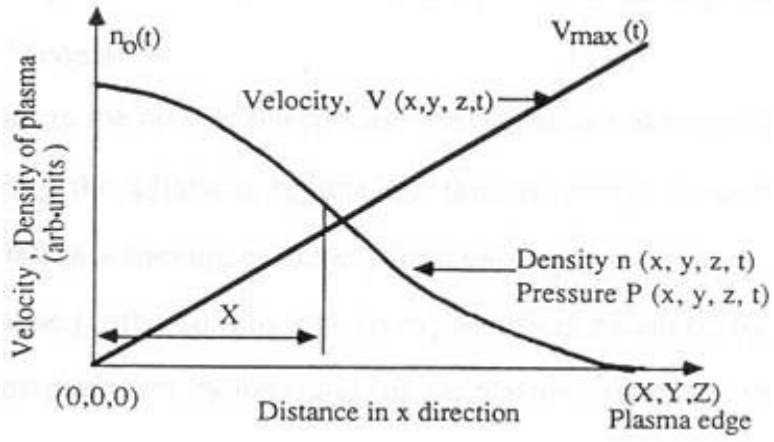

Fig.2.4. Schematic profile showing the density (n), pressure (P), and velocity (v) gradients in the plasma in x direction, normal to the target surface. [41]

2.1.3 Adiabatic Plasma Expansion and Film Deposition

After the termination of the laser pulse in vacuum there is no additional input of particles from the target into the plasma because there is no absorption of laser energy. Thus an adiabatic expansion occurs with a thermodynamic relation given by:

$$T\left[X(t)Y(t)Z(t)\right]\gamma^{-1} = const \qquad (2.5)$$

where the γ corresponds to the ratio of the specific heat capacities at constant pressure C_p and volume C_v. In the adiabatic regime, the thermal energy is converted to kinetic energy while the plasma achieving extremely high expansion velocities. The temperature drop is slow because the cooling caused by expansion is balanced by energy regained from recombination processes by ions and the plasma expands in one direction. The initial dimensions of the plasma are much larger in the transverse directions (y and z) which are in the order of millimeter, while in perpendicular direction (x) is in the order of 20-100μm. In the adiabatic expansion regime the velocity of the plasma increases in the direction of the smallest dimension.

2.2 Characterization Methods of Thin Films

Thin film properties are determined by their chemical composition, the content and type of impurities in the thin film or on the surface, crystal structure of the thin film and on the surface, and the types and density of structural defects. In addition, as the applications of thin films extend to microelectronics, optoelectronics, storage devices and other areas, electrical, optical and magnetic properties also need to be monitored and optimized. In particular to $La_{0.5}Sr_{0.5}CoO_3$ (LSCO) and $Ce_{0.9}Gd_{0.1}O_{1.95}$ (CGO) thin films as cathode and electrolyte in solid oxide fuel cells, electrical, chemical, and structural analysis should be monitored. For electrode materials such as LSCO, electrical and micro/nano-structural information are the main properties need to be studied in detail. While for electrolyte materials such as CGO, electrochemical and structural characteristics are the major requirement. Most experimental procedures including thin film characterizations are introduced in the experimental part in each chapter. In the following, several important techniques which have been extensively used during this research are discussed in detail. This study is focused on structural analysis, X-ray, TEM, STEM, and EIS techniques will be discussed in detail including basic principles and applications in thin film microstructure analysis.

2.2.1 X-ray Diffraction (XRD: Structural Analysis)

X-ray diffraction is one of the most important nondestructive structural analysis techniques used to probe and analyze the crystal structure of solids, including lattice constant, orientation of single crystals, preferred orientations of thin films, identification of unknown materials, defects, stress, etc. Basic mechanism of X-ray analysis is based on that, when a parallel and monochromatic X-ray beam with a wavelength λ and angle of incidence θ is diffracted by a set of planes which are oriented in specific directions sharp peaks corresponding to the spacing between the planes appear when the Bragg's law conditions are satisfied:

$$2d \sin\theta = n\lambda \tag{2.6}$$

These peaks are characteristic to materials and crystal structures. The crystal structure of a specific material determines the diffraction pattern, and in particular the shape and size of the unit cell determine the relative intensities of these lines. In the structural analysis by using X-ray of known wavelength λ, and measuring θ, we can determine the "d" spacing of various planes in the crystal. The essential features of an X-ray spectrometer are shown in figure 2.5. It should be noted that the incident beam, normal to the reflecting plane, and the diffracted beam are always coplanar; and the angle between the diffracted beam and the transmitted beam is always 2θ.

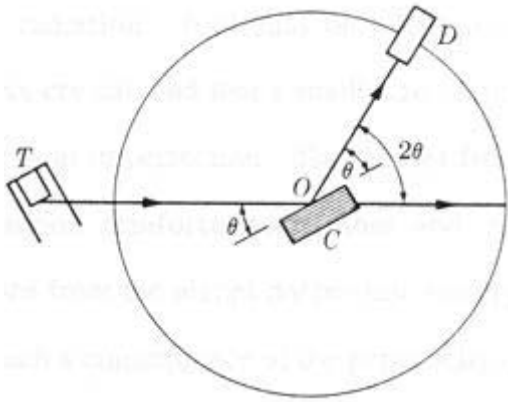

Fig.2.5. Schematic of X-ray spectrometer [42]

Incident X-rays from the tube T on a crystal C which can be set to any desired angle with respect to the incident beam by rotation about an axis O at the center of the spectrometer circle are diffracted from the crystal and detected at the detector D. D is a counter which measures the intensity of the diffracted x-rays, it can rotate around center axis O and set at any desired angular position. Thus by measuring the peak positions, one can determine the shape and lattice parameters of the unit cell, and by measuring the intensities of the diffracted beams one can determine the positions of atoms within the unit cell. Conversely, if the shape and the lattice parameters of the unit cell of the crystal are known, we can predict the positions of all the possible peaks of the film [42].

In the application of the Bragg's Law, certain ideal conditions are assumed, for example, the crystal is perfect and the incident beam consists of strictly parallel and purely monochromatic radiation. It should be noted that only an infinite crystal can be considered as a perfect crystal. This comes from the fact that the waves involved in

diffraction reinforce each other and there is a contribution for the destructive interference from the planes deeper into crystal. Destructive interference is therefore a consequence of the periodicity of atom arrangement just as much as it is the constructive interference. As a result the width of the diffraction curve increases as the thickness of the crystal decreases. Schematic representation of the effect of the fine particle size on diffraction curves is shown in figure 2.6. The following expression gives the estimate of the particle size of very small crystals from the measured width of their diffraction curves: $t = \frac{0.9\lambda}{B\cos\theta_B}$, where $B = \theta_1 - \theta_2$, (from figure 2.6) is the width i.e. the difference between the two extreme angles at which the intensity is zero.

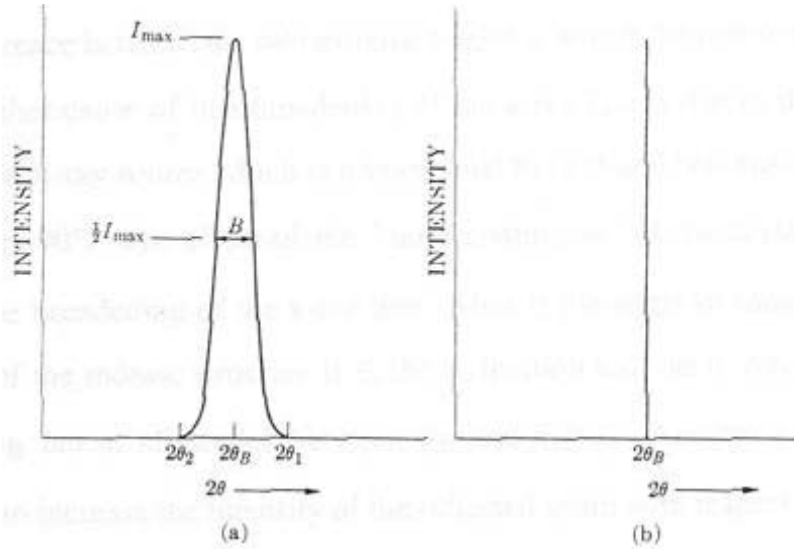

Fig.2.6. Effect of fine particle size on diffraction curve [42]

Another possible cause of line broadening of the x-ray line is the natural "spectral width" of the x-ray source which is proportional to tanθ and becomes quite obvious as θ

approaches 90^o. The existence of the mosaic structure of the crystal or film can also influence the line broadening of the X-ray. Thus if the angle of misorientation between the blocks of the mosaic structure is ε , the diffraction will occur not only at an angle of incidence θ_B but also it will appear in all the angles between θ_B and $\theta_B + \varepsilon$. Another effect of the mosaic structure is an increase in the intensity of the reflected beam with respect to theoretically calculated value for an ideally perfect crystal.

The diffracted beam is stronger than the sum of all the rays scattered in the same direction, because of the reinforcement (strengthening) of the diffracted beams, but extremely weak compared to the incident beam. If the scattering atoms are not arranged in a regular and periodic way then the diffracted x-rays will have a random phase relationship to one another and neither constructive nor destructive interference will happen under such conditions. Then the intensity of a beam scattered in a particular direction is simply the sum of intensities of all X-rays scattered in that direction. If there are N scattered rays and each ray has amplitude A and therefore with intensity A^2 in arbitrary units, then the intensity of the scattered beam is NA^2. However, if the rays are scattered by atoms of a crystal to a direction satisfying the Bragg's Law, then they are all in the same phase and the amplitude of the scattered beam will be N times the amplitude A of each scattered X-ray or NA. Therefore the intensity of the scattered beam is N^2A^2, or N times larger than the case where no reinforcement occurred. This explains why the X-ray intensity of a crystal is much higher than that of an amorphous solid.

As mentioned earlier the intensities of the diffracted beams are determined by the positions of the atoms in the unit cell. Since the X-rays are scattered by electrons and all the atoms in the unit cell establishing an exact relationship between intensity and atomic positions is a complex problem because of many variables involved in the scattering process. When a monochromatic beam of X-rays strikes an atom, two scattering processes occur. Tightly bound electrons go into oscillation and radiate X-rays of same wavelength as that of the incident beam (coherent scattering). More loosely bound electrons scatter part of the incident beam and slightly increase their wavelength to a certain extent depending on the scattering angle (incoherent angle). Since the intensity of the coherent scattering is inversely proportional to the square of the mass of the scattering particle, the net effect of the coherent scattering by an atom occurs only from the scattering by the electrons contained in the atom. The atomic scattering factor f, describes the efficiency of scattering of a given atom in a given direction, where $f \sim \sin\theta/\lambda$, and the values for f for various atoms and various values of $\sin\theta/\lambda$ are tabulated. A typical variation for f in the case of Cu is shown in Fig. 2.7. The coherently scattered radiation from all the atoms undergoes reinforcement (constructive interference) to certain directions, and thus produces diffracted beams.

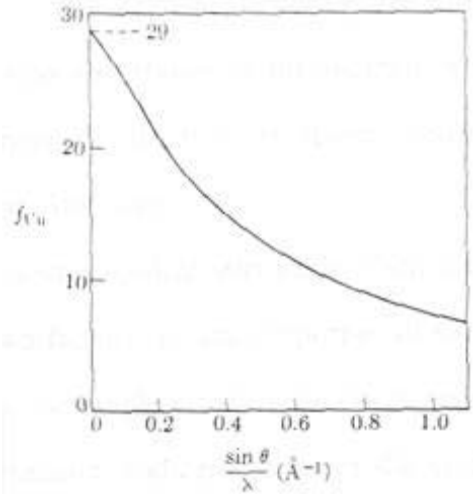

Fig.2.7. The atomic scattering factor of copper [42]

There are six factors affecting the relative intensities of the diffraction lines: (1) polarization factor, (2) structure factor, (3) multiplicity factor, (4) Lorenz factor, (5) absorption factor, and (6) temperature factor. Thus, the equation for the relative intensity of a diffraction line can be described as:

$$I = |F|^2 \, p \left[\left(1 + \cos^2 2\upsilon\right) \Big/ \left(\sin^2 \theta \cos\theta\right) \right] \tag{2.7}$$

In equation 2.7, F is the structure factor accounting for the resulting contribution of a unit cell for a specific (*h, k, l*) reflection, and it is a dimensionless value. It is the ratio of the 100 amplitudes scattered by the unit cell to the amplitude scattered by one electron in the same direction. The multiplicity factor p denotes the relative proportion of the planes contributing to the same diffraction, and can be defined as the number of different planes

having same spacing. (Example: p=6 for {100} planes in a cubic crystal, and p=8 for the {111} planes; for a tetragonal crystal p=4 for {100} planes and p=2 for {001} planes). The expression in the numerator part inside the bracket of Equation 2.7 is so called polarization factor, and it arises from the fact that the incident X-ray beam is not polarized. The term in denominator is called Lorenz factor and it is a sum of three factors. First, the value of maximum intensity I_{max} depends on the angular range of crystal rotation over which the energy diffracted in the direction 2θ is appreciable, and depends on $\sim 1/\sin\theta$, and therefore I_{max} is large at low scattering angles, and small at large scattering angles. Second, the number of micro crystallites favorably oriented for diffraction is proportional to $\cos\theta$ and is quite small for high angles of diffractions. Third, geometrical factor which gives the length of any diffraction line is proportional to $R\sin 2\theta$, where R is the radius of the camera, and hence the relative intensity per unit length of the line is proportional to $1/\sin 2\theta_B$. The whole term in brackets in Equation 2.7 is called Lorentz polarization factor and it is plotted in Fig. 2.8. The overall effect of these geometrical factors is the reduction of diffraction intensities at intermediate angles compared to those in forward or backward directions. The absorption factor resulting in a decreased intensity of a diffraction beam due to absorption of the incident beam and the temperature factor due to the thermal vibration of atoms cancels each other since the two factors depend on the scattering angle in opposite ways.

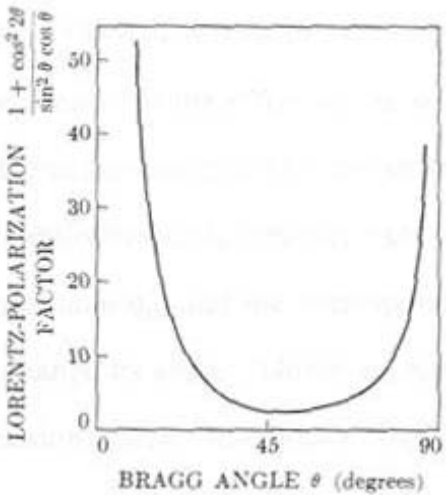

Fig.2.8. Lorentz-polarization factor vs. Bragg angle [42]

The properties (mechanical, electrical, chemical, etc.) of a single phase aggregate are determined by two factors, the properties of the single crystal of the material and the way in which the single crystals are put together to form composite mass. Thus the relative size, perfection, and orientation of the grains make up the aggregate or the film determine the properties of the materials.

The size of grains in a polycrystalline material has a distinct effect on many of its properties, such as increase in strength and hardness with the reduction of the grain size. X-ray diffraction can give semi-quantitative information about the grain size along with the information about the crystal perfection and orientation. X-ray diffraction line broadening can occur because of the size effect of the crystal grains. The diameter of the crystal particle 't' is then measured as $0.9\lambda/B\cos\theta$, where B is the line broadening. The crystal perfection or the effect of both uniform and non-uniform strain also determines

the diffraction line position and shape as shown in Fig. 2.9. If the grain or film is under uniform tensile strain at right angles to the reflecting planes, their spacing become larger than d_0, and the corresponding diffraction line shifts to lower angles, but the shape does not change. However, under non-uniform strain (on the top tension, one the bottom compression) line broadening occurs.

And finally, intensity distribution of lines parallel to the substrate surface can give the information about the presence or absence of a preferred orientation in the film. In such a case the only grains which can contribute to the hkl reflection are ones with (hkl) planes parallel to the substrate surface. If a texture has only a few such grains then the intensity of the hkl reflection will be very low. Film planes which are preferentially oriented as parallel or nearly parallel to the film surface would show extremely high intensity of the hkl planes.

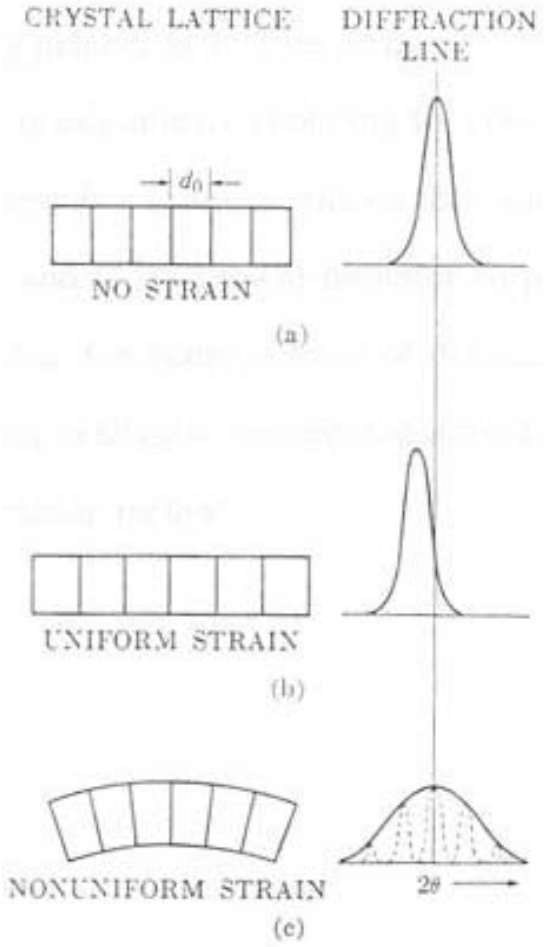

Fig.2.9. Effect of lattice strain on the line width and position [43]

2.2.2 Transmission Electron Microscopy (Structural: TEM)

Transmission electron microscopy (TEM) is a method used in obtaining structural and morphological information of specimens which are thin enough for electrons to transmit through. This technique can help our understanding of materials by providing us with the detailed micro structure down to the atomic levels. Application of TEM is not only limited in materials science research. It can also be used in the semiconductor device technology, biotechnology, and other material or microstructure related field. For example, TEM has been extensively used in device fabrication to provide information about the geometry of patterned films, the uniformity of thickness and coverage, in addition to surface morphology and topography, including size and shape, and presence of compounds. Especially ever since the nano-technology has been introduced to the device fabrication, the resolution of SEM and other normal surface probing techniques can not satisfy the requirements of detailed atomic structure study. TEM has become the most important technique which can probe detail structural and defect information. Additionally, TEM can also give cross-sectional view of interface regions which can give information about the interfacial reactions, perfection of devices, and diffusion study. When it is combined with other analytical techniques, such as STEM, EELS, and EDX TEM is a very powerful material characterization technique which can combine imaging and chemical compositional study down to a single atom(or a column of atoms, strictly speaking). For example, JEOL 2010FEG has point to point resolution of 0.18 nm. In this section, major parameters of TEM are listed. Several important imaging and

diffraction techniques are discussed and related examples for different techniques are presented.

Resolution and Aberration

The main parameter of a transmission electron microscope is its resolution and magnification. Magnification can be increased easily by increasing acceleration voltage of TEM but increasing resolution is rather a hard work due to many related parameters. When there is no aberration of lenses classical Raleigh criterion describes the smallest distance that can be resolved approximately by:

$$\delta = 0.61\lambda / \mu \sin\beta \qquad (2.8)$$

where λ is the wavelength of the radiation, μ the refractive index of the viewing medium, and β is the semi-angle of collection of the magnifying lens. Due to the coherency of electron beam in TEM and the short wavelength of the accelerated electrons (λ is in the order of hundredths of an Å), the resolution limit is down to 1 Å (for 1MeV electrons λ=0.0087 Å, and a=5x10^{-3} radian).

Along with the chromatic aberration and the stigmatism, spherical aberration is one of the main electromagnetic lens defects that limit the resolution of the electron microscope as shown in figure 2.10 a. The spherical aberration is a lens defect arising from the non-paraxiality of the electron beam which cause electrons to leave the point P at higher

angles with respect to the optic axis of the microscope and to focus before the image plane, while electrons left the objective lens closer to the optic axis are focused on the image plane. Thus instead of a point focus a disk with a radius r_s is formed, where $r_s=C_s \beta^2$, β is the angular aperture of the lens.

Chromatic aberration arises from the non-chromaticity of the electron beam. Non chromaticity is the energy difference among electrons. Electrons leaving the electron gun have slightly different energies and the difference ΔE is a bout 3eV. This causes the faster electrons to be less refracted from the objective lens than the lower energy electrons, as shown in figure 2.10 b. The higher energy electrons thus are brought in focus beyond the image plane.

Astigmatism arises from the asymmetric magnetic field and it occurs when the lens exhibits different focal lengths, depending on the plane of the ray paths. Thus in the figure 2.10 c the rays traveling plane A are focused at PA while the rays in plane B focused at point PB. Because of this astigmatixm a point on the object is imaged as a disk with radius $r_A=\beta\Delta f_A$, where Δf_A is the maximum difference in focal length arising from astigmatism. If all the astigmatisms can be corrected, the sample is thin enough, and chromatic aberration is negligible then the resolution is limited by the spherical aberration error. The resolution is governed by the combination of Rayleigh criterion and the aberration error.

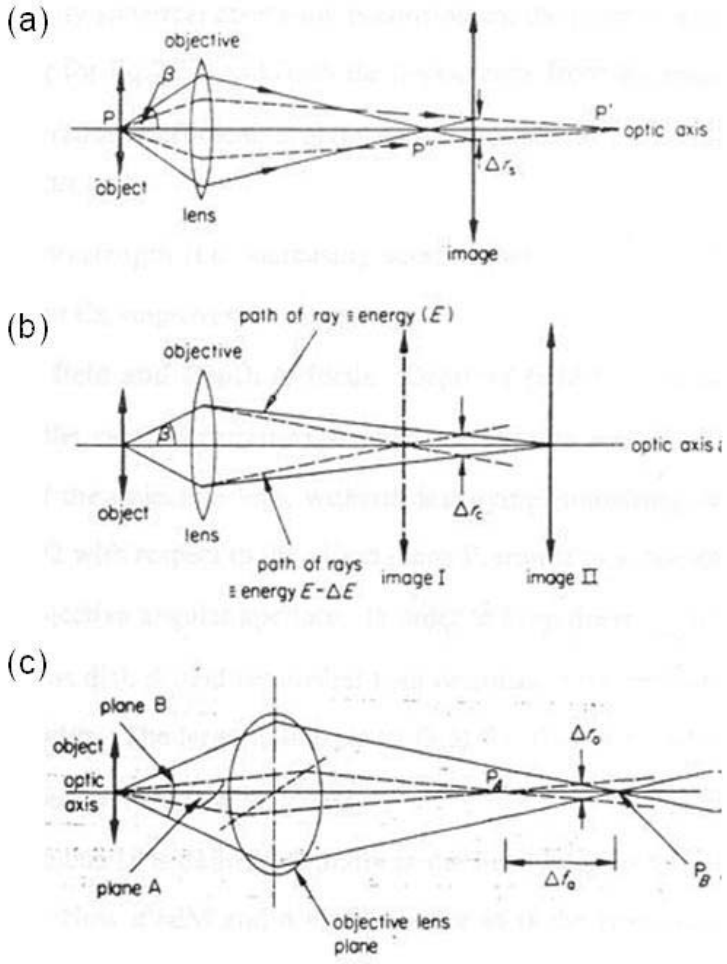

Fig.2.10. Objective aberration (a) Spherical, (b) chromatic, (c) astigmatism [44]

$$r_{\min} = 0.91\left(C_s\lambda^3\right)^{0.25} \tag{2.9}$$

This equation describe the practical resolution of the microscope. Where ‘r’ is the spherical aberration error, and Cs is the spherical aberration, λ is the wavelength of electron.

Depth of Field and Depth of Focus

Depth of field D is the value on both sides of the theoretical object plane P of the objective lens within which the resolution can be maintained. A specimen shift of D/2 with respect to the object plane P results in a disc of radius $r = \frac{aD}{2}$ where 'a' is the objective angular aperture. In order to keep the resolution from diminishing, the diameter of this disk should be smaller than or equal to the resolution distance'd', so that aD = d. The larger depth of focus (D~500Å) means the better focusing over a larger range of the specimen thickness. Depth of focus 'D' is defined similarly in the final image plane as depth of field in the object plane. Now d'=dM and $a' = \frac{a}{M}$, where M is the final magnification. Thus depth of focus $D'=DM^2$. Magnification of the order of 10^5 would give about 500m depth of focus.

Image and Diffraction Modes

The objective lens takes the electrons exiting from the exit surface of the specimen, disperses them to create a diffraction pattern (DP) in the back focal plane, and recombines them to form an image in the image plane. To see the diffraction pattern you have to adjust the imaging system lenses so that the back focal plane for the intermediate lens can be the image plane. Then the diffraction pattern is projected onto the viewing screen, see figure 2.11 A. For imaging mode, you readjust the intermediate lens so that its object plane is the image plane of the objective lens. Then the image is projected onto the viewing screen, as shown in 2.11 B.

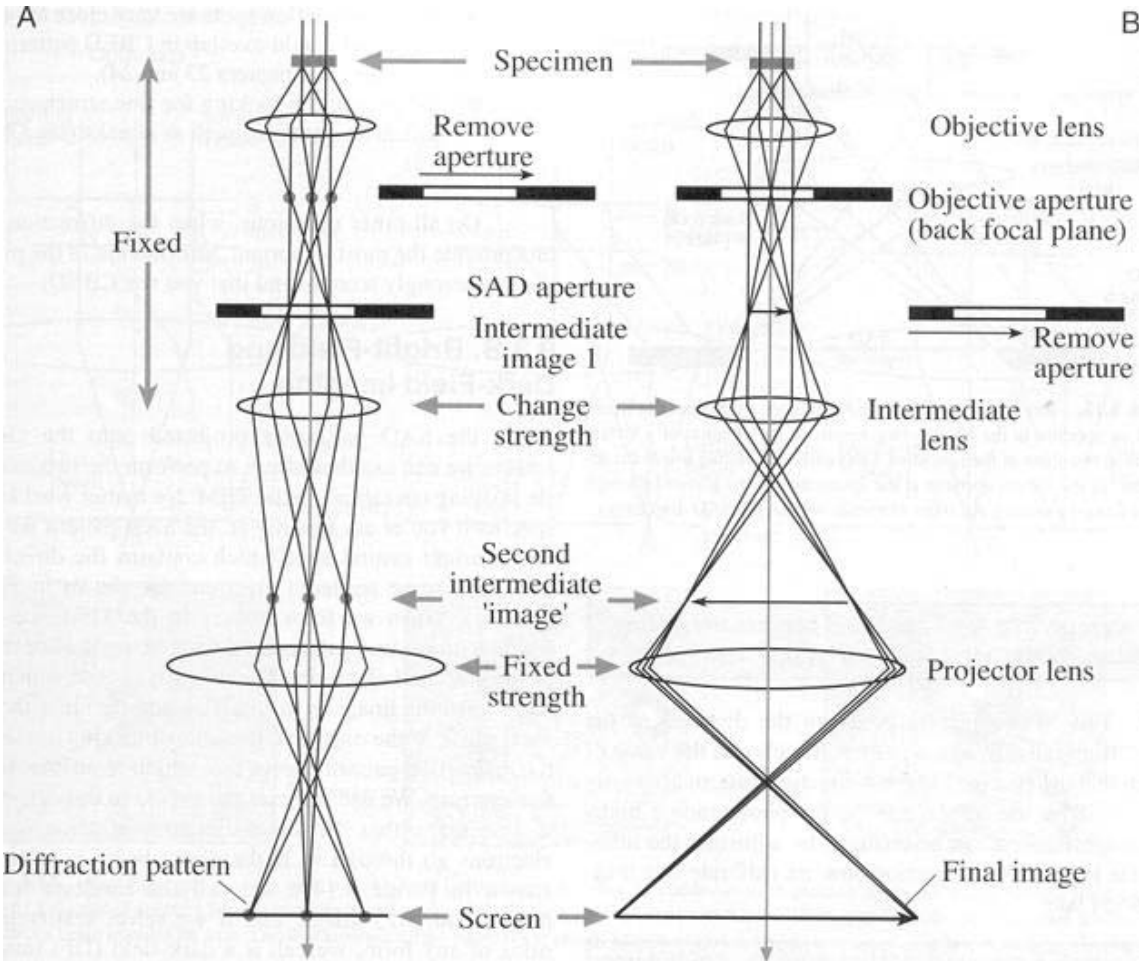

Fig.2.11. The two basic operations of the TEM imaging system involve (A) Projecting the diffraction pattern on the viewing screen and (B) projecting the image onto the screen. In each case the intermediate lens selects either the back focal plane or the image plane of the objective lens as its objects [45]

Image Mode and Image Contrast

The image contrast in TEM arises because of the scattering of the incident beam by the specimen. As the electron beam transverse the specimen it changes both its amplitude and phase and the image contrast occurs because of these changes. There is a fundamental distinction between amplitude contrast and phase contrast which can both contribute to the image. The amplitude contrast can be divided into mass-thickness contrast and diffraction contrast according to Williams and Carter's descriptions.

Diffraction contrast is most widely used in identifying defects and distinguishing different types of crystal defects. Diffraction contrast occurs because of coherent elastic scattering at special (Bragg) angles. The intensity in a diffracted beam depends strongly upon the deviation parameter 's'. Since the crystal defects distort the diffracting planes the diffraction contrast from regions close to the defect depends on the properties of the defects such as strain field. The specimen has to be tilted into two-beam conditions in order to get good interpretable diffraction contrast. Mass-thickness contrast arises from incoherent Rutherford elastic scattering of electrons. Any scattered beam can contribute to the formation of the image.

Two-Beam Conditions, Bright Field and Dark Field

Bright field and dark field are specific imaging conditions when the specimen is tilted so that only one diffracted beam is strong. When the electrons in the strongly excited beam have been diffracted by a specific set of hkl planes the area that appears bright in the

dark field (DF) mode is the area where the hkl planes are at Bragg condition. Therefore, the DF image contains specific orientation information. Bright field (BF) image is obtained when only the directly transmitted beam is used for the formation of the image. However, the dark field image appears when the image is created using only diffracted beam. The specimen can be tilted to set up several different two beam conditions. After tilting the specimen the DF images can be formed from each strongly diffracted beam and each of which will give a different image. BF and DF images show almost complementary contrast under two-beam conditions. Further enhancement of the contrast from defects can be achieved by slightly tilting the specimen away from the exact Bragg condition, where s=0, towards positive value of 's'. In this way the interpretable images under kinematical diffraction conditions are obtained. Parameter 's' is called "deviation from Bragg Condition".

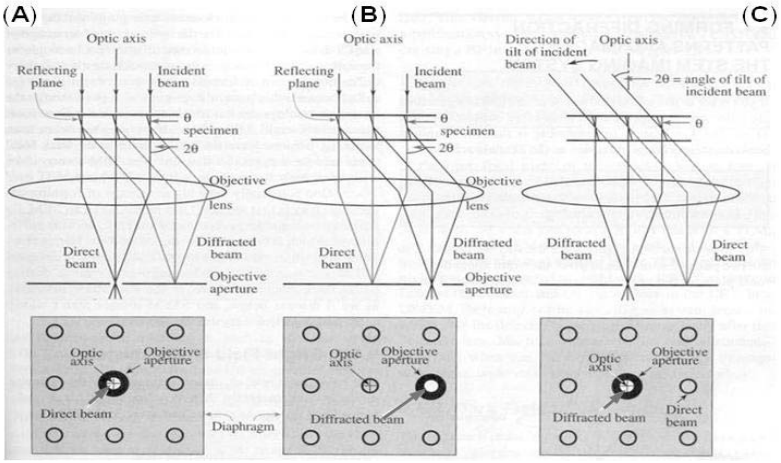

Fig.2.12. Ray diagrams showing how the objective lens aperture are used in combination to produce (A) a BF image formed from the direct beam, (B) a displaced-aperture DF image formed with a specific off-axis scattered beam, and (C) a CDF image where the incident beam is tilted so that the scattered beam remains on axis [45]

Phase Contrast and High Resolution TEM (HRTEM)

Phase contrast is formed when the transmitted and diffracted beams recombine, as shown in the figure 2.13. The recombination of the two beams preserves their amplitudes and phases. This way lattice images or even structure images can be formed. If details in the structure such as atomic structure, atomic positions, and defects in that structure are to be seen or to obtain higher resolution images, higher angles information in reciprocal space has to be included, i.e. images should be taken with as many beams as possible. One of the approaches to model the image formation in atomic resolution mode, or high resolution mode is to consider the transmission electron microscope as a linear system [46]. This approach is called the information theory approach. For a linear system $\alpha S_0 + \alpha S_{0'} \rightarrow \beta S_1 + \beta S_{1'}$, where the expression on the left is the input signals, and that on the right side is output signal. Linear combination of input signals is transmitted by the system as a linear combination of output signals. The analogy from the information theory is shown in figure 2.14. The input signal is the object phase shift which is the phase shift in the electron wave function cause by the specimen in TEM. The action of the transmission system is to take this input signal from the real space and transform it to Fourier space i.e. consider the input spectrum as object phase shift spectrum in TEM.

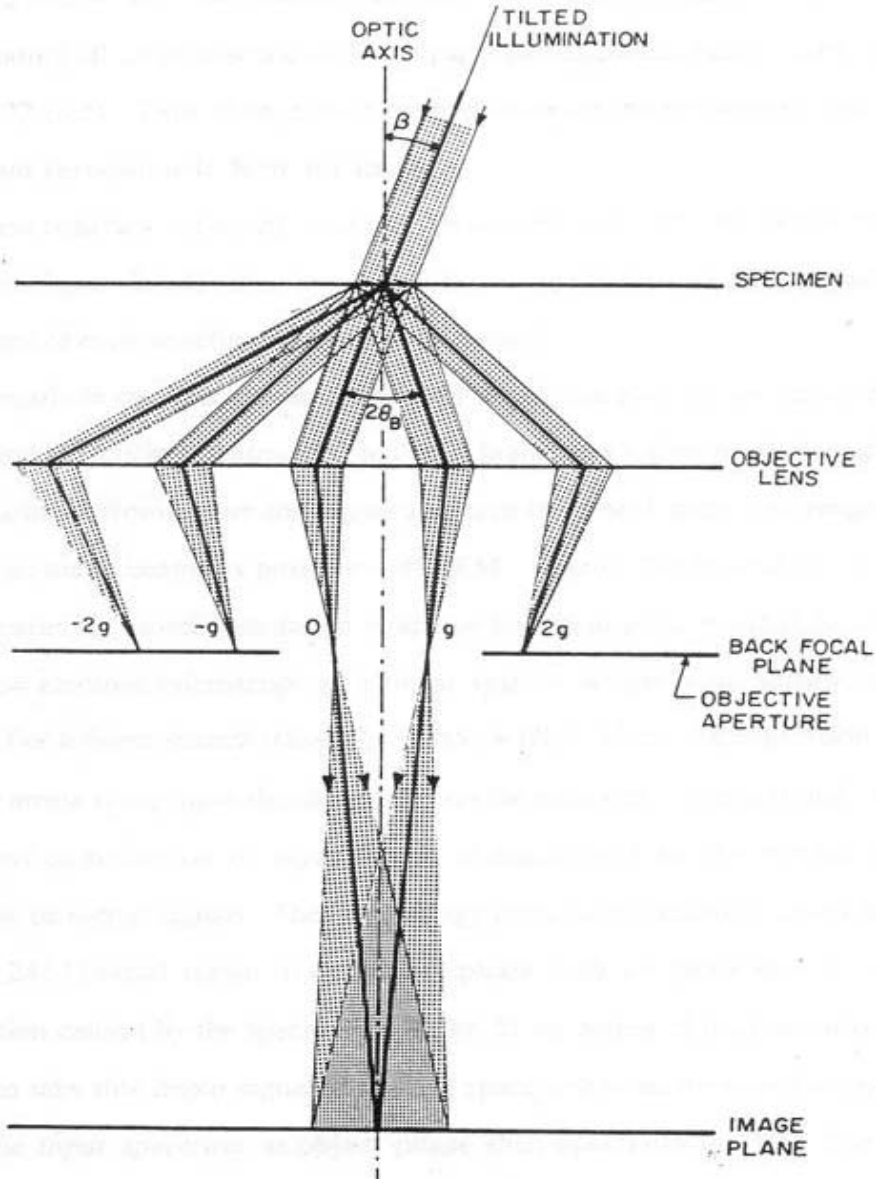

Fig.2.13. Phase contrast imaging from a periodic object. The diffracted and transmitted beams recombine at the image plane [47]

Through Fourier Transform the input signal is transformed into input spectrum. Then by multiplying the image spectrum by transfer function or phase contrast transfer function

the output spectrum is achieved in TEM. Finally the image contrast is achieved through inverse Fourier Transform of the output signal. This scheme from the information theory can be used to explain the contrast in TEM.

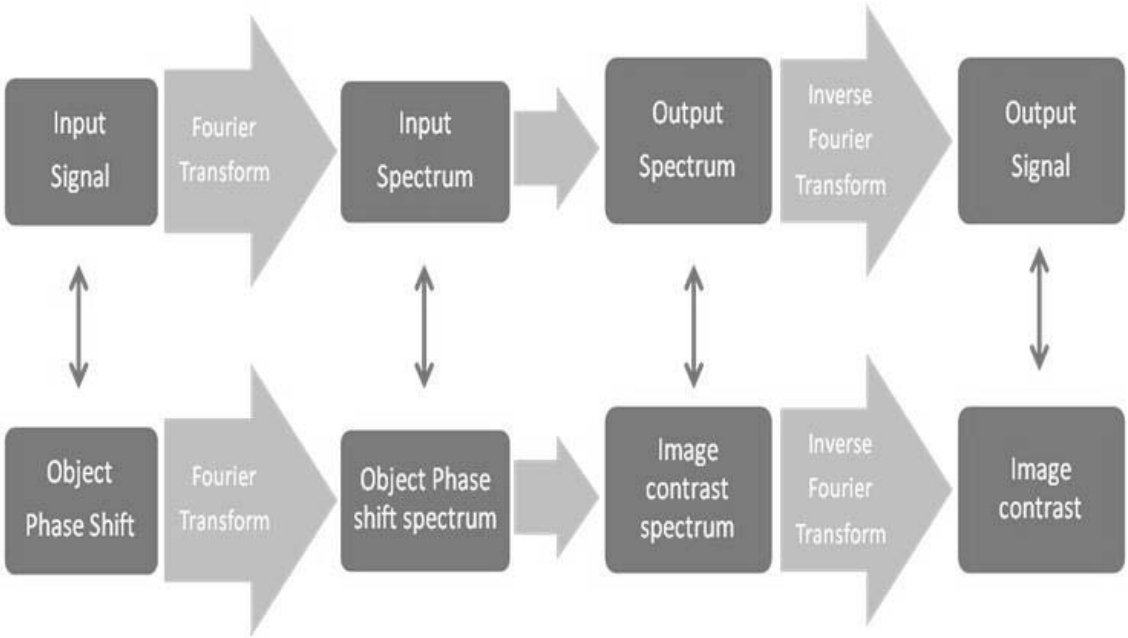

Fig.2.14. Schematic representation of TEM as a transmission system

Diffraction Mode and Selected Area Diffraction

The most common diffraction mode is the parallel beam mode with 10^{-4}~10^{-5} radian angular dispersion. While in convergent mode the angular aperture is in the order of 10^{-2} radian for specific applications. The main features of the electron diffraction are as follows. Electrons have very small wavelength compared to lattice parameters and this

results in small diffraction angles. Thus the Bragg equation becomes: $2\theta = n\lambda / / d_{hkl}$, at the diffraction angle $2\theta \cong 1^{o}$. Electrons interact very strongly with the matter so the kinematic approximation does not apply. Very thin specimen is used in transmission electron diffraction and the resulting diffraction domains are in the form of fine rods perpendicular to the specimen. To achieve a *hkl* reflection, the reflection sphere has to intersect the corresponding diffraction domain. The observed reflections have the incident direction [uvw] as a zone axis relative to the lattice planes (hkl) and therefore the reflection indices obey the following expression for the zero Laue zone:

$$hu + kv + lw = 0 \tag{2.10}$$

This is an equation of the reciprocal lattice plane (uvw) passing through the origin and containing lattice point hkl.

Selected Area Electron Diffraction (SAD)

Depending on the adjustment of the post objective lenses such as intermediate lens and diffracted lens on one of the planes, either the electron diffraction pattern or the electron image of the object is displayed on the final viewing screen or the film. The selected aperture inserted into the image plane limits the diameter $d_{s'}\left(=d_s m\right)$ of an image selection area. Choosing a given aperture results in selecting a specific area of the specimen. The active area of SAD is in the order of micrometer (d_s=1μm), so with magnification of the objective lens 100 (m=100), the image selection area $d_{s'}$ is 100 μm. The diffraction length L is not directly expressed. If we know that ΔL=*dR* the diffraction constant or camera constant K (=ΔL), which describes the magnification of the diffraction pattern, can be determined from standard specimen. Where *R* is the distance between the transmitted beam and the diffracted spot corresponding to interplanar distance d. The diffraction mode can be utilized in many other sub modes such as selected-area electron diffraction, micro diffraction or nano diffraction, and convergent beam electron diffraction etc.

2.2.3 Scanning Transmission Electron Microscopy (STEM): Structural and Elemental Analysis Using Z-Contrast

In scanning transmission electron microscopy (STEM), Z-contrast techniques can provide strong compositional sensitivity results at atomic level. To achieve bright field STEM image transmitted beam is used. To obtain Z-contrast dark field images high-angle Rutherford-scattered electrons are collected by high angle annular dark field detector. In obtaining atomic resolution Z-contrast image probe size is critical. STEM imitates the parallel beam in a TEM by scanning strictly parallel to the optical axis at all times. The key feature of STEM is that the scanning beam does not change direction when the beam is scanned. Fig. 2.15 illustrates how the STEM achieves the parallel beam. Two pairs of scan coils are used to pivot the beam about the front focal plane of the upper objective (C3) pole piece. Then the C3 lens ensures all electrons emerging from the pivot point to be brought parallel to the optic axis and the C1 lens crossover image is formed in the specimen plane. If the objective lens is symmetrical then a stationary diffraction pattern is formed on the back focal plane. One big advantage of forming images this way is that there is no need for lenses in an SEM so defects in the imaging lenses do not affect image resolution. Image resolution is controlled by beam only [48-52].

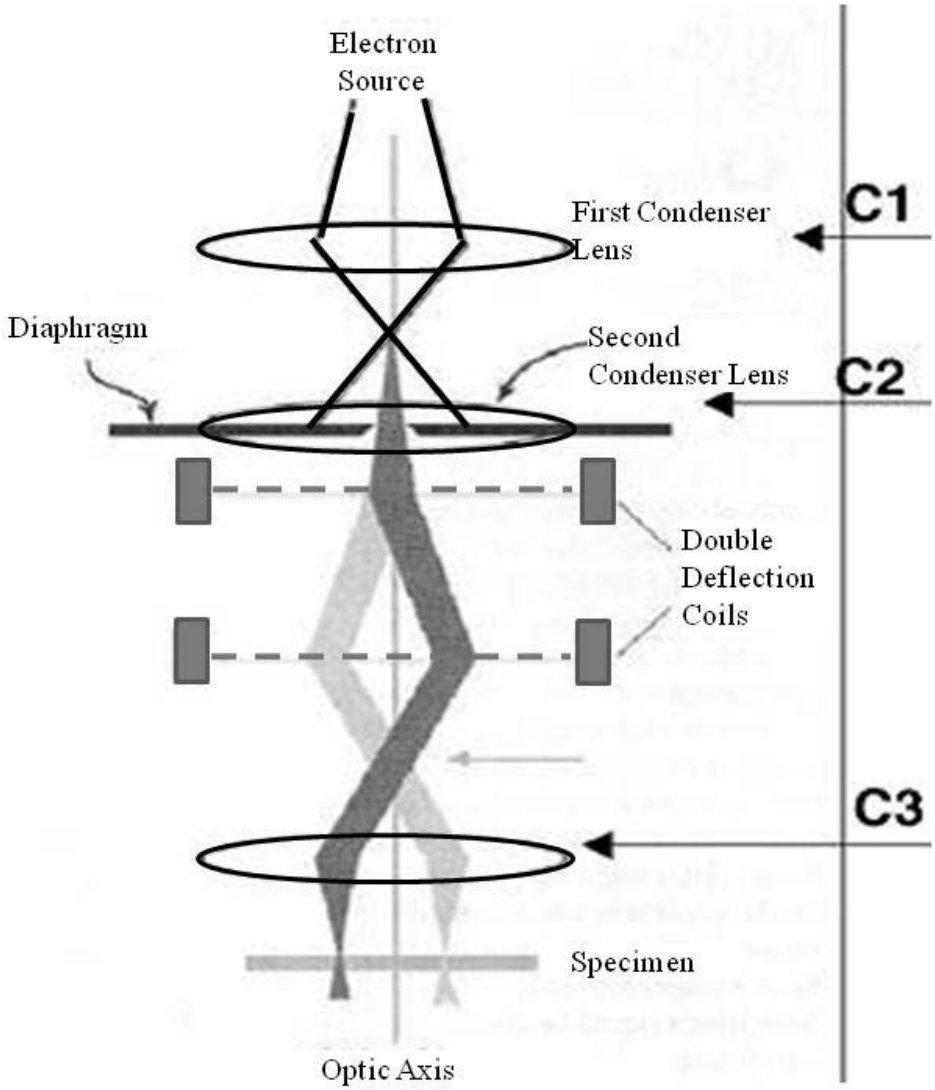

Fig.2.15. Scanning the convergent probe for STEM image formation using two pairs of scan coils between the C2 lens and the upper objective polepiece. The probe remains parallel to the optic axis as it scans [52]

Therefore, chromatic aberration can not limit the STEM resolution unlike the case in TEM imaging system and this is advantageous if you are dealing with a thick specimen.

Similar to TEM techniques, STEM can form its own bright field (BF) and dark field (DF) images.

Bright Field STEM Images

The basic principle of image formation in the scanning mode is fundamentally different from that of a static beam TEM imaging system. In the TEM, a portion of the electrons transmitted through an area of the specimen is selected and the distribution is projected onto a screen. While in STEM, by adjusting the scan coils the specimen is scanned by the beam. These same coils are used to scan the CRT synchronously. The electron detector is used as a interface between the electrons coming from the specimen and the image viewed on the CRT. Since it scans up to 2048 scan lines to construct an image on the CRT, the whole process of the STEM imaging is much slower than TEM imaging. In order to form a BF image in TEM an aperture is inserted into the plane of the TEM diffraction pattern and only the electrons direct through it are allowed into the imaging system [53-55]. In STEM mode an electron detector is used in exactly the same way as the aperture in TEM. The detector only allows the desired electrons to hit the detector to constitute the image.

Annular Dark Field Images

Annular dark-field (ADF) imaging is a method of mapping samples in a scanning transmission electron microscope (STEM). Images are formed by collecting scattered electrons with an annular dark-field detector in scanning transmission electron microscopes [52].

For dark field imaging, the annular dark field detector collects a much larger number of electrons than conventional dark field imaging in the TEM. This gives advantages of signal collection efficiency and as a result lower electron dose required. As opposed to Bragg scattered electrons, an annular dark field images, Z-contrast images, formed only from very high angle and incoherently scattered electrons are highly sensitive to variations in the atomic number of atoms in the sample. This technique is also known as high angle ADF (HAADF). Annular detector, which surrounds the BF detector, is used to collect the scattered electrons [56,57]. ADF detector is centered on the optics axis and has a hole in the middle, within which the BF detector sits as shown in Fig. 2.16a. Fig. 2.16b shows the complementary ADF (c) and BF (d) images.

Magnification in STEM

Scanning images are not magnified by lenses. STEM magnification is controlled by the scan dimensions on the specimen. This is an essential difference between scanning imaging and static imaging. If the scanned area on the specimen is 1cm × 1cm, and the

resultant image displayed on a CRT is 10cm ×10 cm then the magnification is 10. If the scan dimension is reduced to 10nm, the magnification is 10^7 times.

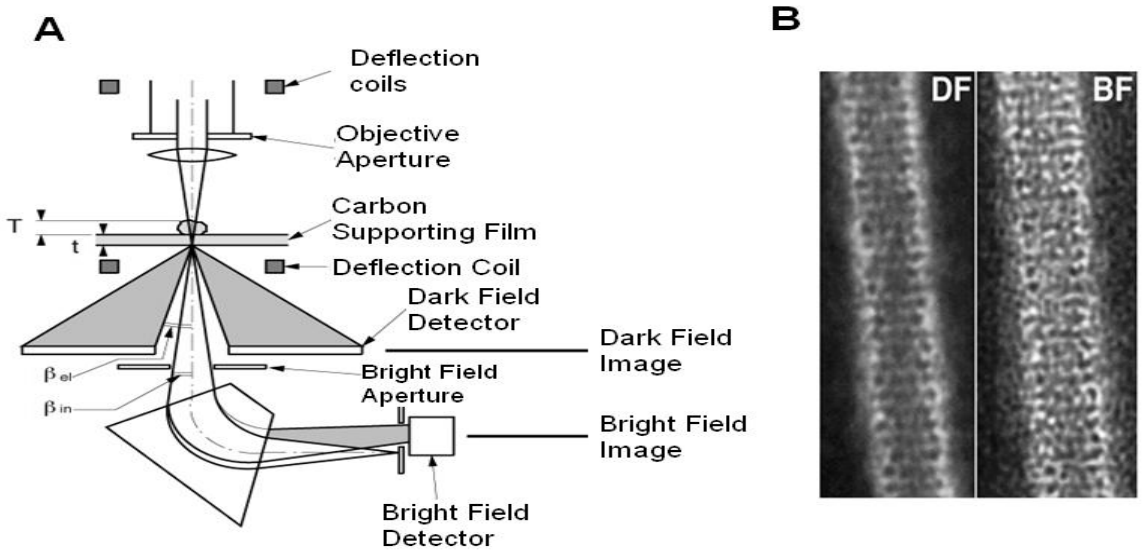

Fig.2.16. STEM image formation: (A) Schematic diagram of STEM (B) complementary ADF and BF images [52]

Atomic Structure Determination

Using the HAADF or Z-contrast imaging technique atomic structure determinations can be made. Each atom can be considered to scatter independently with a cross section approaching Z^2 dependence on atomic number if we detect the scattering at high angles and over a large angular range. An object function that is strongly peaked at the atom sites can be derived successfully from this cross section. The detected intensity thus

consists of a convolution of this object function and the probe intensity profile. The spatial resolution is limited only by the probe size of the microscope due to the small width of this object function (~ 0.1Å) [58]. For a crystalline material in a zone-axis orientation the atomic columns can be illuminated individually because of the greater size of atomic spacing than the probe size. As the probe scans over the specimen an atomic resolution compositional map is generated where the intensity depends on the root mean square of atomic number of the atoms in the columns. If dynamic diffraction only results in columnar channeling and simply scales the scattering cross sections of the object function according to thickness then even for thicker specimens the same result holds. The advantage of this methodology is that the changes in focus and thickness do not cause contrast problems in the atomic resolution image [59]. So the atomic column sites can be identified unambiguously during the experiment. With this method atomic columns at grain boundaries can be located without the need for simulated images.

2.2.4 Electrochemical Impedance Spectroscopy

Fuel cell analysis for performance evaluation and optimization is very important in developing cost effective and stable fuel cell systems. Among the major fuel cell testing methods electrochemical impedance spectroscopy has been widely used for this purpose [60-62]. The AC impedance method can give information on oxygen reduction reaction kinetic, mass-transfer, and electrolyte membrane resistance losses [63-69]. Application areas include single cell optimization and fabrication, electrolyte conductivity, fuel cell impedance, and fuel cell localized impedance. In the optimization of fuel cell performance, the major focuses of the AC impedance approach have been the temperature [70-73] and the microstructure [74-76].

General Concept of AC Impedance of SOFC

As shown in Fig. 2.17, a single cell consists of porous anode and cathode and an oxide ion conducting solid electrolyte membrane. The operation principles of a SOFC involve the mass transport process of oxygen and fuel on each side of electrode and the reduction of oxygen molecule at the cathode and the diffusion of the produced oxygen ions through an oxygen electrolyte into the anode. At the anode side the diffused oxygen ions react with fuel gas to produce high temperature water vapor. During this reaction, electrons flow from the anode to the cathode through an external circuit to generate power. In this way, the chemical energy converted into electrical energy.

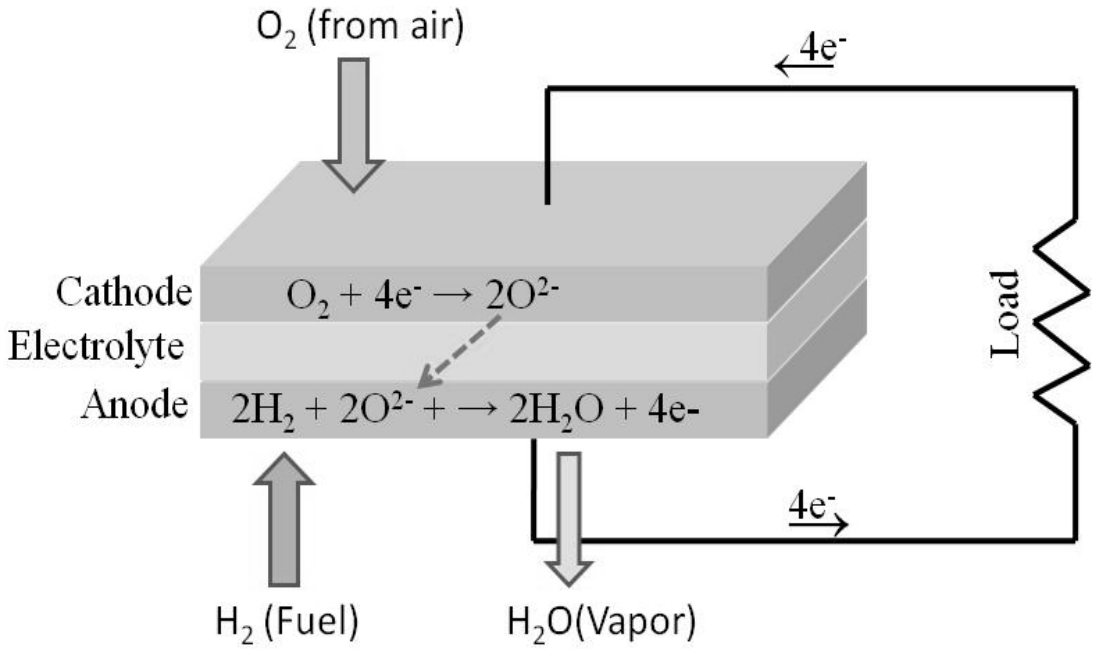

Fig.2.17. SOFC single cell configuration

In the diagnosis of fuel cells impedance spectroscopy has become an essential methodology. AC impedance is a more general concept of resistance. Its modulus and phase depend on the excitation frequency. In the following, a simple one-to-one mapping method is adopted to express the impedance of $Z(j\omega)$. If we use a sinusoidal voltage perturbation $e(t) = E_0 \sin(2\pi ft + \phi)$, during measurements to excite a linear time-invariant (LTI) circuit system then according to linear system theory [68, 77], we can get an AC current response, $i(t) = I_0 \sin(2\pi ft + \psi)$, which has the same frequency as $e(t)$. E_0 and ϕ denote the amplitude and the initial phase of $e(t)$ respectively. In the

same way, I_0 and ψ denote the amplitude and the initial phase of $i(t)$ respectively. Normally, the expressions of voltage and current can be mapped and converted from a time domain to a complex domain, $e^*(t) = E_0 \exp(2\pi ft + \phi)$ and $i^*(t) = I_0 \exp(2\pi ft + \varphi)$, respectively, where $e(t)$ and $i(t)$ are the real part of complex number $e^*(t)$ and $i^*(t)$ respectively. Therefore, a simple one-to-one mapping between the time domain and the complex domain where we can access the frequency information is possible. If we denote $2\pi f$ as ω and define as an angle frequency then the transform functions can be expressed as follows:

$$A(j\omega) = \frac{i^*(t)}{e^*(t)} = \frac{I_0}{E_0} \exp\left(j(\psi - \varphi)\right) \tag{2.11}$$

$$Y(j\omega) = \left|Y(j\omega)\right| \exp(j\phi) = \left|Y(j\omega)\right| \cos(\phi) + j\left|Y(j\omega)\right| \sin(\phi) \tag{2.12}$$

$$\left|Y(j\omega)\right| = \frac{I_0}{E_0} \text{ and } \phi = \psi - \varphi \tag{2.13}$$

where $|Y(j\omega)|$ represents the modulus of $Y(j\omega)$ and corresponds to the amplitude transfer function between the excitation and response signals according to a frequency of f, and Φ represents the phase of $Y(j\omega)$ and corresponds to the phase transfer function between the excitation and response signals according to a frequency of f. If $i(t) = I_0 \sin(2\pi ft + \psi)$ is used as an excitation signal and, similarly, $e(t) = E_0 \sin(2\pi ft + \phi)$ is used as an output signal, we can define the following:

$$Z(j\omega) = \frac{\left(e^{*}(t)\right)}{\left(i^{*}(t)\right)} = \frac{E_0}{I_0} e^{(j(\varphi-\phi))} \tag{2.14}$$

$$Z(j\omega) = \left|Z(j\omega)\right| \exp(j\phi) = \left|Z(j\omega)\right| \cos(\phi) + j\left|Z(j\omega)\right| \sin(\phi) \tag{2.15}$$

Both the modulus $|Z(j\omega)|$ and the phase angle φ of $Z(j\omega)$ are functions of frequency. In general, $Z(j\omega)$ is the AC impedance and $Y(j\omega)$ is the admittance which are the inverse of each other as in $Y(j\omega) = 1/Z(j\omega)$. In fact, SOFC devices are complicated systems containing chemical, electrochemical, and multiple mass-transfer processes. The coupling of these complex processes makes the systems nonlinear. The relationship between the voltage and the current at different frequencies in such a nonlinear system does not directly follow the expressions obtained from a LTI system. For example, under large excitation of the amplitude of voltage or current SOFC systems tend to show strong nonlinear behavior in their interfacial responses. But if the applied AC voltage amplitude Δe is less than a given thermal voltage [64] then the system can be considered as a linear system since the basic differential equations that govern the response of the fuel cell system become nearly linear. The approximate linearization can also be derived based on the nonlinear circuit system analysis [68].

If the equivalent linear equations are known at every point of the steady-state characteristic then the behavior of a non-linear system can be defined entirely in linear terms [78, 79]. Hence, the local analysis of a non-linear system can be confined to the field of linear system theory. From an experimental point of view, it is satisfactory to

measure the impedance of an electrochemical cell about a given polarization point (E_0, I_0) by using a perturbation signal of very low amplitude. If the voltage–current (V–I) curve of a SOFC system satisfies the relationship shown in Fig. 2.18, and the low amplitude of the sinusoidal voltage, $\Delta E \sin\left(2\pi ft + \phi\right)$, is superimposed on the DC voltage of E_0 at a static working point Q(E_0, I_0) then a low amplitude of sinusoidal current change, $\Delta I\sin(2\pi ft + \psi)$, will be observed, which is superimposed on the DC current of I_0 at the same static working point.

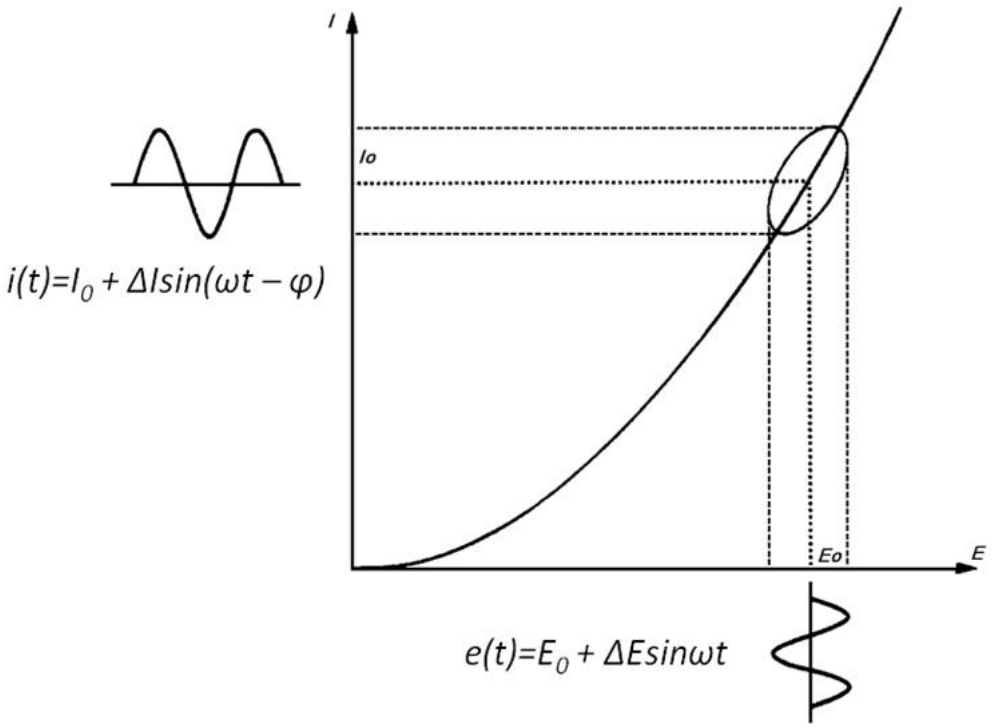

Fig.2.18. A Lissajous ellipse is observed on an X-Y recorder when a sine wave voltage is superimposed on the dc polarization voltage

When we focus on the vicinity of a static work point (E_0, I_0) of the nonlinear system, the Taylor expansion of the voltage, e, can be expressed as

$$\Delta e = \left(\frac{de}{di}\right)_{(E_0,I_0)} \Delta i + \frac{1}{2}\left(\frac{d^2e}{d^2i}\right)_{(E_0,I_0)} \Delta i^2 + \cdots \qquad (2.16)$$

If the amplitude of the perturbation signal is small enough, the higher order terms in Eq. 2.16) will be negligible compared to the first term. Therefore, Eq. (2.16) can be reduced approximately to the first term of the expression, $\Delta e = \left(de/di\right)_{(E_0,I_0)} = \Delta i$, and de/di is roughly regarded as a constant around the static work point of Q(E_0, I_0). This process is known as quasi-linearization. Therefore, under the condition that the amplitude of the perturbation signal is smaller than the required value a SOFC may be treated as a linear system with respect to the AC impedance measurement [64]. If the two sine waves are plotted on an X-Y recorder, a Lissajous figure (ellipse) similar to that shown in Fig 2.18 can be observed. Hence by measuring the electrochemical impedance all along the polarization curve we can perform a complete characterization of the interface and this will enable us to compare the data with a model.

When an excitation current or voltage signal is supplied to a SOFC, a corresponding output signal, which is determined by the coupling of electrical, chemical, electrochemical, and mass transport processes, gives a characteristic impedance, $Z(j\omega) = Z' + jZ''$. $Z(j\omega)$ is also called the transfer function of the SOFC system, and it represents

the amplitude and the phase shift relationship between the excitation and response signals in terms of the frequency of ω $(=2\pi ft)$ [63].

Theoretically, this transfer function $Z(j\omega)$ will have physical meaning only under the following preconditions [80-82]. First, the response of the system must be related to the excitation signal only. Second, $Z(j\omega)$ is meaningful only when the excitation/response of the system is described by a set of 'linear' differential laws. This means the impedance of the system must be independent of the excitation signal magnitude. Third, the system must be able to return to its original state when the perturbation is removed and the system is stable. Forth, the impedance must be finite for all values of ω, including $\omega \rightarrow 0$ and $\omega \rightarrow \infty$. Because of high complexity of a SOFC system fitting all these preconditions perfectly may not be possible. Therefore, when EIS is used for SOFC diagnosis some special issues must be considered in advance.

The physicochemical processes within a SOFC can be divided into two categories as internal factors and external factors. Materials and their composition, microstructures, and component sizes are internal factors on the other hand factors such as temperature, pressure, mass transport and concentrations can be categorized into external factors. The measured impedance '$Z(j\omega)$' is the overlapped responses of both the internal and external factors and this implies that there is an inherent relationship between $Z(j\omega)$ and SOFC characteristics. For example, the measured impedances can give information about fuel cell reaction kinetics such as reaction activation, electrolyte resistance, mass-

transfer efficiency, and operation conditions. With all these data SOFC performance and failure modes can be diagnosed. Based on the diagnosis, fuel cell performance can be improved by proper choice of material, microstructure engineering of the component materials and component structure optimization. In addition, the failure mode identification can be used to improve our fundamental understanding of the SOFC operating mechanism and can be used for further improvement of the system. Since the SOFC system has its own limitation in meeting the requirements of the transfer function '$Z(j\omega)$', one has to be sure that the approximations are rational when processing the AC impedance data.

Measurement of SOFC AC Impedance

Generally, four types of impedance data are measured. The four types are the time/frequency domain measurement [64,77], in/ex situ measurement [64, 68], static and instantaneous impedance measurement [83-87], and linear/non linear measurement [88, 89]. Rapid advances in digital signal processing techniques in recent years have made possible the time domain method. However, measuring in the frequency domain by the analog technique still remains more popular. Nowadays, the use of very powerful digital computers and digital signal processing technique made the automatic data acquisition of AC impedances, which were once a bottleneck in the diagnosis process, simple and easy process. On the contrary, due to the complexity, impedance modeling and validation are becoming the hardest steps. In particular the frequency range measurement, perturbation of signal amplitudes, use of reference electrodes, and noise elimination require special

attention although we can trust the accuracy and reliability of data acquired from some commercially available equipment.

Frequency Range

Commercially available AC impedance instruments such as Solartron and Gamry products can operate at a wide range of frequencies. The typical operating range is from 0.1 MHz to 30MHz [68]. This allows the synchronized analysis of several overlapping responses, such as resistance, electrochemical reaction kinetics, gas phase diffusion, and gas molecular adsorption and desorption. The typical frequency range chosen for SOFC measurements is in the range of 0.01 Hz to 1.0MHz.

Perturbation Amplitude

In order to meet the linearity requirement of the transfer function '$Z(j\omega)$' the amplitude of the perturbation signal must be small enough. Based on the well known linear system theory which can be employed either in the time domain or the frequency domain we can analyze the small amplitude signal perturbation. On the contrary, for the case where the amplitude of the perturbation signal is large a nonlinear analysis must be employed. Despite of the complexity of the large amplitude perturbation analysis, non linear analysis can provide additional useful information [68, 89]. Typical perturbation voltage signal amplitude range for SOFC AC impedance measurements is 10 to 50mV [68, 90].

Reference Electrode

Reference electrode geometry and position in the cell greatly affect the accuracy of the results for SOFC AC impedance measurements. To deal with this challenge, Nagata et al. [91] studied the relationship between the overpotential and the reference electrode position in a solid electrolyte. The configuration effect of the reference electrode position and its function in eliminating and diminishing measurement errors is described in detail in the discussion of Adler [92] and Hsieh et al. [93-96]. Fig. 2.19 shows a three electrode measurement configuration, together with a schematic Nyquist impedance diagram [97]. Where RE, CE, and WE stand for the reference electrode, counter electrode and working electrode, respectively. On the other hand R_E, R_{DC}, and R_P denote the electrolyte resistance, total resistance and polarization resistance, respectively. Another well-known issue between the working electrode (WE) and the reference electrode (RE) is the uncompensated impedance. This can cause a large error in the controlled electrode potential. The optimization in the size and geometry of a reference electrode and the arraigning of a reference electrode with respect to the working electrode are still challenges in the elimination or alleviation of measurement errors [98-100].

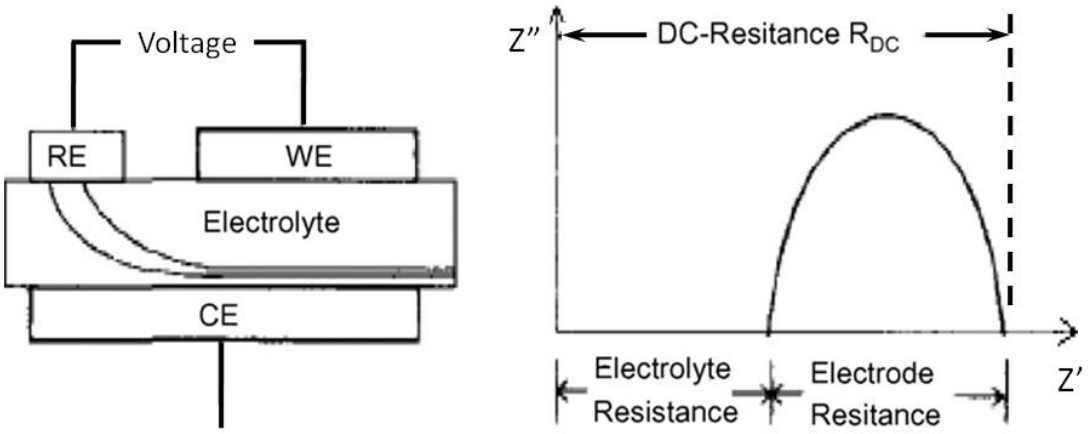

Fig.2.19. Three-electrode measurement configuration and a schematic Nyquist impedance diagram

Signal-to-Noise Ratio

Because the AC impedance measurement is a very noise sensitive process to facilitate obtaining reliable data a reasonably high signal-to-noise ratio is required and shielding and grounding is one of the most popular methods to reduce noise. To monitor noise level an oscilloscope is often connected to the SOFC current collectors [68]. In addition, the approach for electric wiring between the fuel cell and the impedance measurement instruments should deal with different measurement situations and noise reduction, although the measurement itself is implemented automatically. Calibration using a pre-constructed equivalent circuit, which has similar AC impedance values to the actual fuel cell, is essential for measurement validation.

Limitation of AC Impedance

AC impedance, $Z(j\omega)$, can be expressed as $Z(j\omega) = \mathrm{Re}(Z) + \mathrm{Im}(jZ)$, where $\mathrm{Re}(Z)$ is the real part and often expressed as Z' and $\mathrm{Im}(jZ)$ is the imaginary part as known Z" [77]. The plot of Z' versus Z" is called a Nyquist plot. Since from the Nyquist plot no corresponding frequency data can be found for any data point on the plot another popular presentation method for the impedance plot, the Bode plot, is also used complementally. To represent the frequency data the impedance is plotted with the log frequency on the *x*-axis and both the log absolute value of the impedance $|Z(j\omega)|$ and the phase-shift on the *y*-axis. Unlike the Nyquist plot, the Bode plot can explicitly show frequency information. Detailed examples of Nyquist and Bode plots were shown in Fig. 2.20. Most of the time, to give a clearer picture of the AC impedance Nyquist and Bode plots are presented together. Three dimensional plotting is another alternative method for impedance display [64].

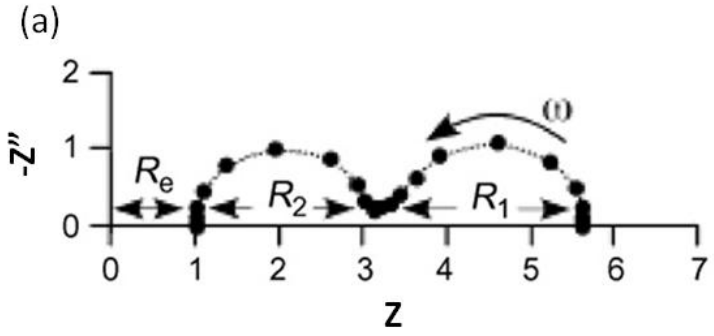

Fig.2.20. AC impedance of a SOFC. (a) Nyquist diagram of Impedance Z and (b) bode plot of impedance 'Z'

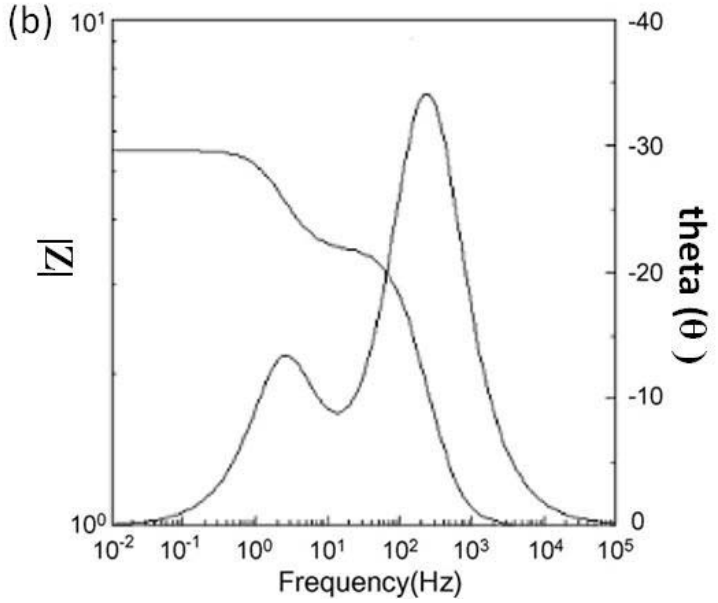

Fig.2.20. Continued,

The variation of many factors and parameters in SOFCs decides the impedance plot shapes and based on this shpe useful information such as material composition, microstructure, and electrochemistry of the fuel cell components can be obtained. It is well known that the electrode microstructures play a significant role in the electrochemical reaction because the different microstructures of electrodes can result in different EIS plot shapes. Therefore, if a relationship between microstructure and electrochemical kinetic parameters can be made well then the information about the SOFC microstructure properties could be obtained through EIS modeling. However, due to the lack of a simple correlation between the impedance plot and SOFC properties, it is

very difficult to come to a complete agreement on the interpretation of the impedance data, especially those from the intermediate to high frequency arcs regime [101-103].

AC impedances '$Z(j\omega)$' are the averaged results of all electrochemical processes consist of the internal and external factors of a SOFC system. And it is also true that there is a possibility a fuel cell could exhibit an identical impedance plot under completely different internal and/or external factors. Consequently, it is a challenging work to explain the transport and reaction mechanisms using only impedance plots. Hence, impedance plots and other analysis techniques must be used all together in order to obtain more complete and reliable information [104-107].

AC Impedance Advantages in SOFC Diagnosis

For the past three decades the AC impedance technique has been widely used in fuel cell characterization. In SOFC characterization, the AC impedance technique provides a very powerful methode to investigate the reaction kinetics and to optimize cell and material design and fabrication. This electrochemical impedance measurement technique has major advantages over other methodologies as stated next. It is nondestructive in the sense that only small amplitude electronic perturbation is applied and the response is measured [108, 109]. The AC impedance method can be used to study the individual processes in SOFCs. It can separate a single process from many other processes concurrently exist. The transport and reaction processes are considered to take place at the three-phase boundaries in between the electrode and electrolyte layers, where gas, ionic species, and electronic species come into contact. These processes involve charge-

transfer at the electrode/electrolyte interface, mass diffusion, and electrochemical and chemical interface reactions. For example, in the case of the reference electrode configuration [110-112], it is possible to separate electrode overpotential loss process from the other processes of the electrolyte. Furthermore, by applying proper impedance models, mass transport and charge-transfer contributions to the whole polarization can be separated [113]. Similarly, when the symmetrical electrodes are used where both electrodes are supplied with identical fuel or oxidant gas [114] then the same separation results can be acquired. This is the case for the reference electrode configuration. In general, since the polarization resistance of cathode is far greater than that of the anode the anode polarization loss [115] can be ignored as shown in Figure 2.21. Figure 2.21 b verifies far greater cathode impedance compared with that of the anode and reference. The last advantage of using impedance analysis is that the resolutions of EIS data are very high and accurate due to the availability of high performance computer.

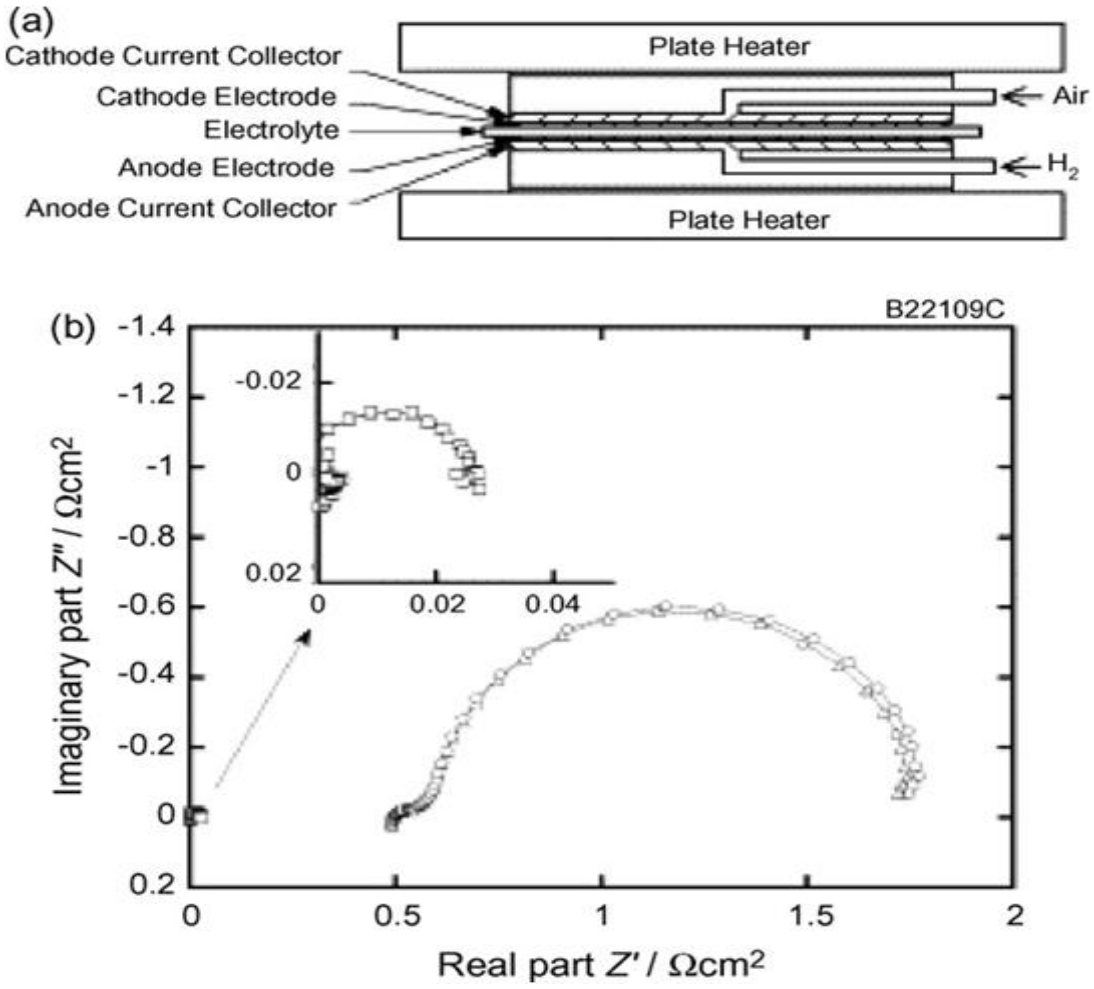

Fig.2.21. (a) Whole cell with a two-electrode configuration and (b) the corresponding Nyquist plot

CHAPTER III

NANOSTRUCTURED CATHODE THIN FILMS WITH VERTICALLY-ALIGNED NANOPORES FOR THIN FILM SOFC AND THEIR CHARACTERISTICS*

3.1 Overview

Nanostructured cathode thin films with vertically-aligned nanopores (VANP) were processed using a pulsed laser deposition technique (PLD). These VANP structures enhance the oxygen-gas phase diffusivity, thus improve the overall thin film SOFC performance. $La_{0.5}Sr_{0.5}CoO_3$ (LSCO) and $La_{0.4}Sr_{0.6}Co_{0.8}Fe_{0.2}O_3$ (LSCFO) were deposited on various substrates (YSZ, Si and pressed $Ce_{0.9}Gd_{0.1}O_{1.95}$ disks). Microstructures and properties of the nanostructured cathodes were characterized by TEM, HRTEM, SEM and electrochemical measurements. Additionally these well aligned VANP structures relieve or partially relieve the internal thermal stress and lattice strain caused by the differences of thermal expansion coefficients and lattice mismatch between the electrode and the electrolyte.

---

*This chapter is reprinted with permission from "Nanostructured Cathode Thin Films with Vertically Aligned Nanopores for Thin Film SOFC and Their Characteristics" by J. Yoon, R.Araujo, N Grunbaum, L. Baque´, A Serques, A. Caneiro, X. Zhang, H. Wang, Appl. Surf. Sci. 254 (1) (2007) 266-269. Copyright 2007 by Elsevier.

3.2 Introduction

Thin film solid oxide fuel cells (SOFCs) have attracted world-wide research interest for compact and high-efficiency stationary power applications since they have potentially high energy-density but high operating temperature. Recent research efforts have been focused on decreasing the SOFC operating temperature and increasing cell performance [116,117], which may allow mobile power applications. To achieve the goal of processing high performance fuel cells operating in the temperature range of 550 °C $\leq$ T $\geq$ 750 °C, many new materials have been explored for the electrolyte and electrode. For example, Gadolinia-doped ceria $Ce_{0.9}Gd_{0.1}O_{1.95}$ (CGO) is one of the best candidates for the electrolyte to replace Yttria stabilized Zirconia (YSZ) [116-118]; $La_{0.5}Sr_{0.5}CoO_3$ (LSCO) and $La_{1-x}Sr_xCo_{0.8}Fe_{0.2}O_3$ (LSCFO) are considered to be promising cathode materials because of their high electronic (σ_e) and ionic (σ_i) conductivities [119,120], high oxygen permeability, good catalytic power [121], and excellent compatibility with CGO. It was reported that the material characteristics including grain size, surface morphology, porosity, path tortuosity, material composition and defects play an important role on the properties of the cathode layer and the kinetics of the oxygen reduction reactions taking place at the cathode. For example, the ionic conductivity σ_i increases with the Sr and Co compositions in LSCO and LSCFO at the cost of chemical stability. However, increasing Sr and Co contents increases the thermal expansion coefficient of the cathode layer and therefore leads to higher thermal mismatch between the electrolyte (CGO) and cathode layers [122]. To increase the ionic conductivity of the

electrode, another approach is to increase the effective surface area of the triple phase boundary (TPB) [123]. To achieve this goal, we propose to introduce large amount of TPBs by synthesizing nanopores in the thin film cathode by promoting the columnar growth of the cathode layer. In this paper, we report our recent efforts on the growth of nanostructured cathode layer with vertically-aligned nanopores (VANP). These VANPs increase the oxygen permeability and at the same time relieve or partially relieve the internal thermal stress and lattice strain caused by the differences of the thermal expansion coefficients and the lattice mismatch between the electrode and the electrolyte.

3.3 Experimental

Deposition of the cathode thin films of LSCO and LSCFO was performed in a chamber with a KrF excimer laser (Lambda Physik 210 λ= 248 nm, 10 Hz). Various substrates including YSZ, Si and pressed $Ce_{0.9}Gd_{0.1}O_{1.95}$ disks were selected for this experiment. The laser beam was focused to obtain an energy density of approximately 10 J cm^{-2} at 45° angle of incidence. The targets were hot-pressed LSCO and $La_{0.4}Sr_{0.6}Co_{0.8}Fe_{0.2}O_3$ (LSCFO) disks prepared using a mixture of La_2O_3, $Sr(NO_3)_2$, Co3O4 and Fe_2O_3 powders in stoichiometric amounts. LSCO (about 1–2 μm) and LSCFO (about 1–2 μm) were deposited under the Zone I conditions of the ‘‘Structure Zone Model’’ as discussed in the literatures [124-128]. The typical growth rate for these thin films is about 1 nm/s with an oxygen partial pressure of about 200 mTorr. The substrate temperature was varied from 100–500 °C to optimize the film crystallinity and the nanopore size.

Microstructural characterization of these films was performed by cross-sectional transmission electron microscopy (TEM) using a JEOL3000F analytical electron microscope with a point to point resolution of 0.18 nm. Surface morphology for the thin films was conducted using scanning electron microscopy (SEM). Impedance spectroscopy measurements were carried out on heating from 400 to 750 °C in air or over oxygen partial pressures ranging from 10^{-3} to 1 atm, by steps of 50 °C, by using a potentiostat/impedance analyzer Autolab (Eco Chemie BV) between 10^{-3} and 10^{4} Hz. The electrochemical cell was prepared with the symmetrical configuration and platinum grids, slightly pressed on porous electrodes, were used as current collectors.

3.4 Results and Discussion

Cross-sectional view and surface morphology of one such LSCO thin film are shown in the SEM images in Fig. 3.1a–c. Figure 3.1a shows the cross-sectional view of the LSCO deposited at 300 °C on Si substrate. In SEM, the sample was tilted 45° in angle in order to view both the cross-sectional and surface structures. The LSCO layer has columnar grains with average grain size of 100–200 nm. Vertically-aligned nanopores can be clearly observed (marked as white arrows) (Fig. 3.1a). The film thickness in this sample is about 1 μm. High magnification SEM image (Fig. 3.1c) on the surface shows the nanopores in between columns. It is interesting to note that by controlling the deposition temperature, the microstructure of the films can be varied from dense and epitaxial film

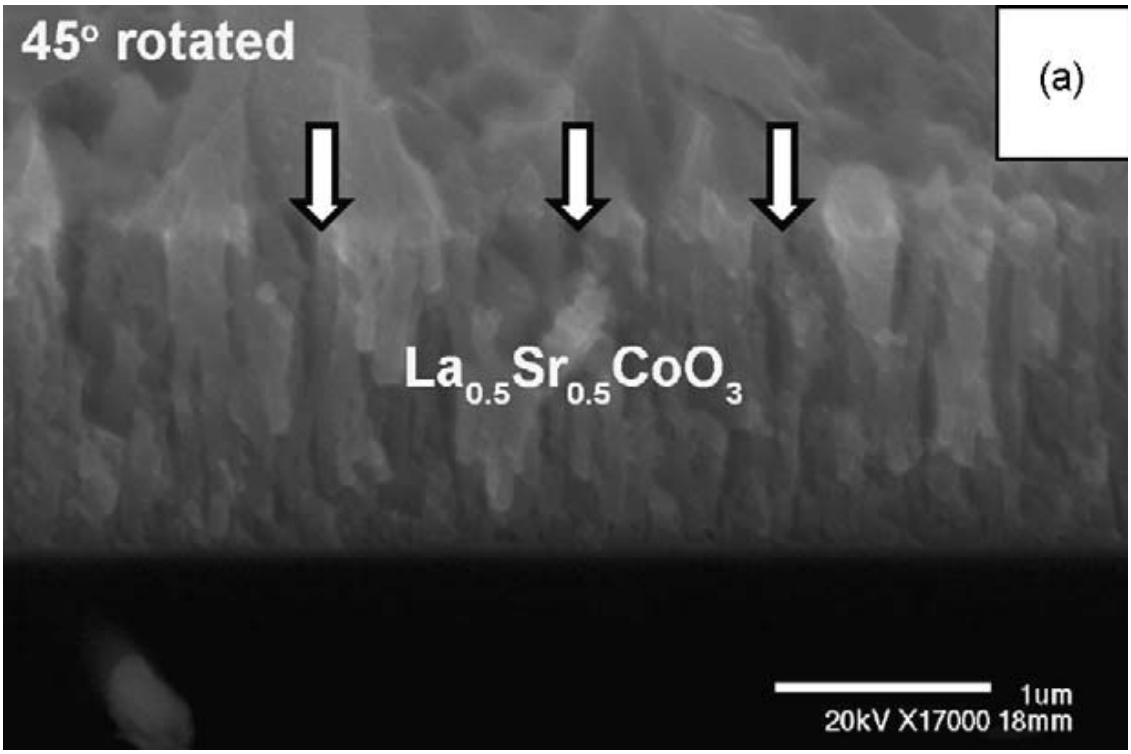

Fig.3.1. SEM images of (a) cross-sectional view and (b) low and (c) high magnifications of surface morphology of a LSCO cathode grown by PLD on Si substrate

to porous and textured film with controllable nanopore size. From the low magnification SEM image on the film surface in Fig. 3.1b, no microcrack was observed in the film with VANP structures. We believe that these nanoscale pores effectively relieve the thermal stress and the strain caused by the lattice mismatch between the thin film cathode and the underlying substrate.

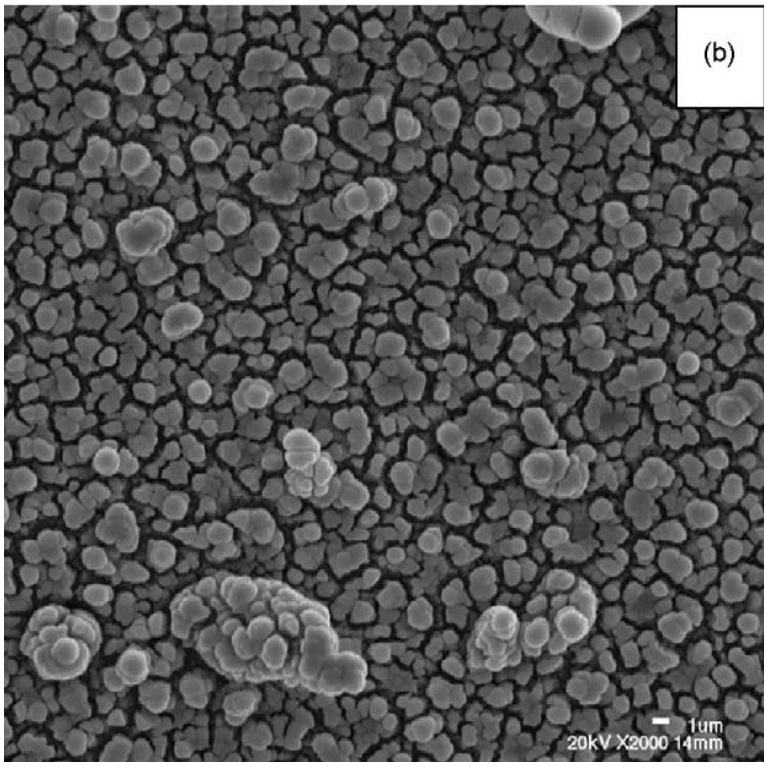

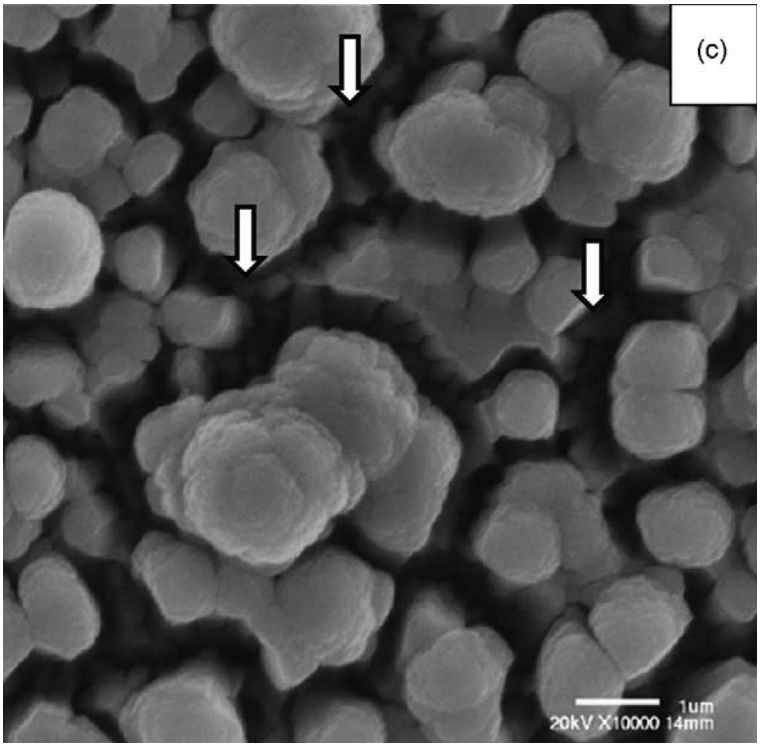

Fig.3.1. Continued,

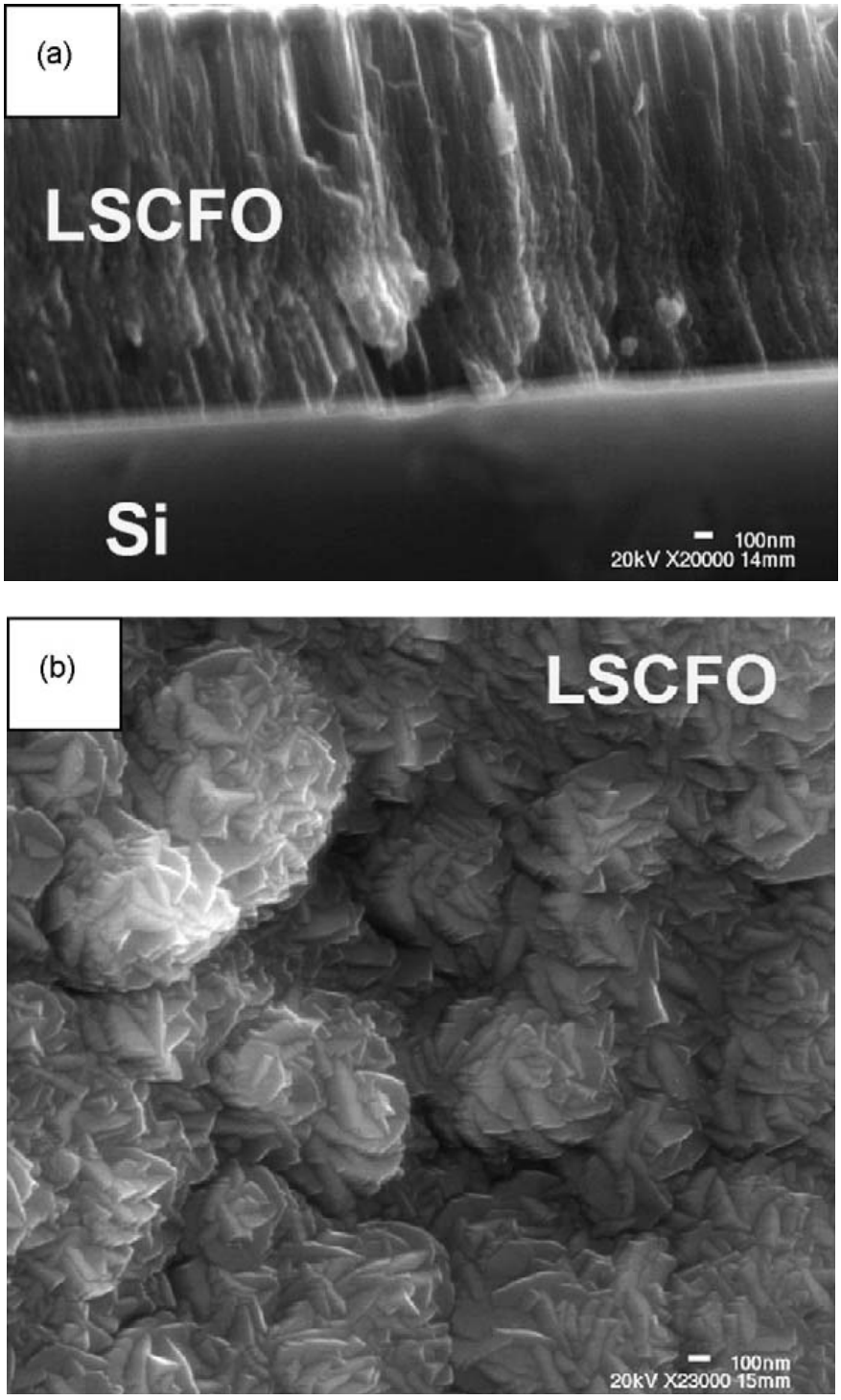

Fig.3.2. SEM images of (a) cross-section surface of LSCFO on Si substrate deposited at the same run with LSCFO on CGO disks, and (b) its corresponding surface SEM

Fig. 3.2a and b show the cross-section view and surface morphology of LSCFO grown on Si substrates. This typical sample was grown at the same deposition run with the LSCFO on CGO disks for the following impedance measurements. This sample was deposited at 500 °C. The VANP structures were observed in the cross-section view (Fig. 3.2a). The LSCFO film has clear columnar grain structure formed with nanopores extend through out, which is very similar to the LSCO case. However, the surface morphology of LSCFO is quite different compared with the LSCO. It shows a flower-like surface morphology in each individual grain. In this sample, there was no thermal-stress-induced crack observed. We performed a cross-sectional TEM analysis on several of the LSCO and LSCFO thin films which have VANP structure according to SEM study. Low magnification cross-section TEM image (Fig. 3.3) from one such LSCO film (~2 μm) confirms the existence of the VANP structures (marked as vertical arrows). In certain regions, these pores are as small as few nanometers. These nanopores extend all the way from the film-substrate interface to the film surface which is about 2 μm in this case. These additional vertically-aligned grain boundaries and nanopores could dramatically increase the amount of the TPBs (gas–cathode–electrolyte boundaries) at the interface between the cathode and the electrolyte and enhance the oxygen gas phase diffusion by decreasing the path tortuosity, thus improving the kinetic performance. In order to test the performance of these cathode thin films with VANP structure, we deposited LSCFO layers on both sides of a pressed CGO disk to form a whole cell structure. The film thickness is about 1 μm for both sides and we used the same deposition conditions to achieve identical properties for both layers.

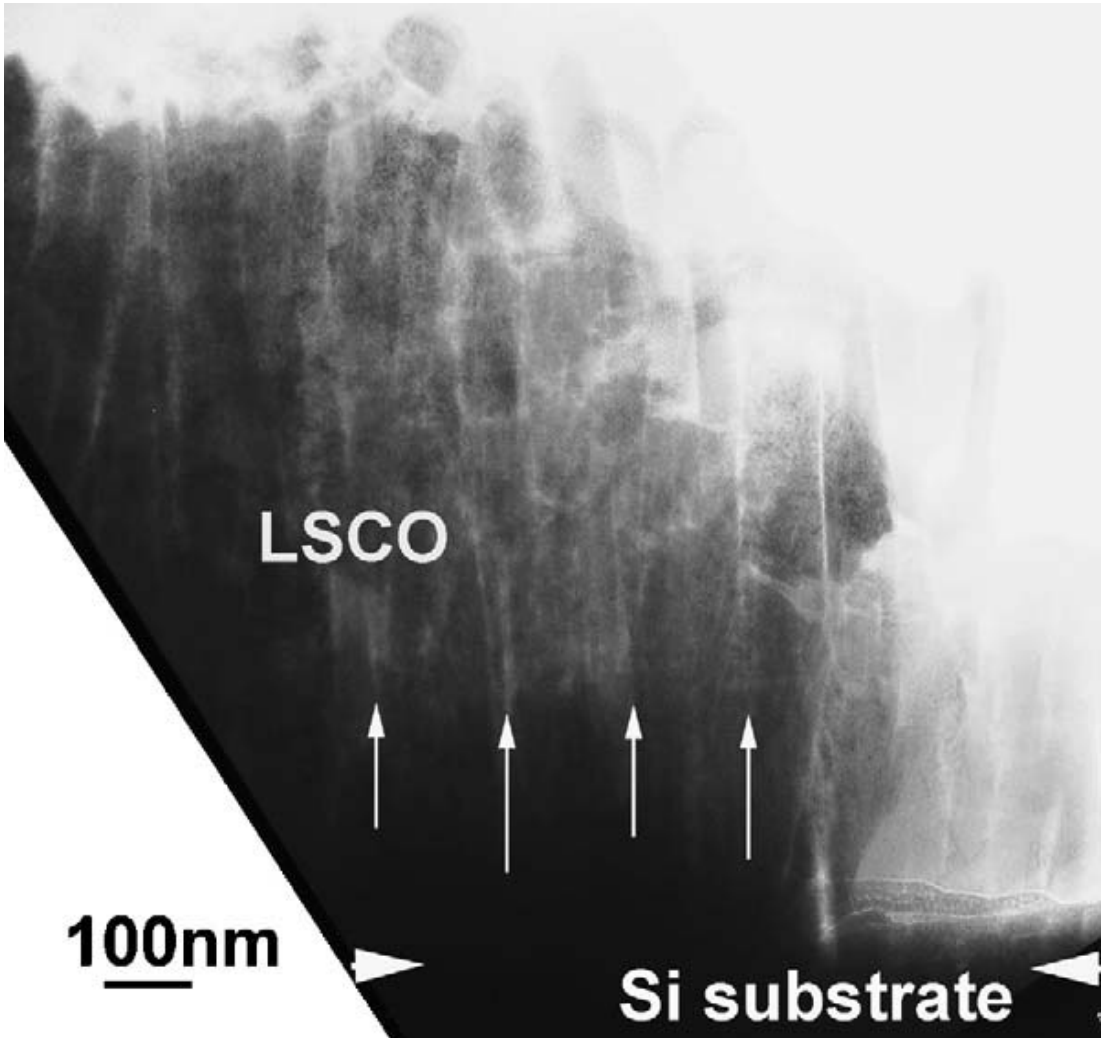

Fig.3.3. Low magnification cross-section TEM image of one such porous LSCO on Si substrates with vertical-aligned nanopores (marked as vertical arrows)

We measured the complex impedance spectra in oxygen in the range 400–750 °C. Arrhenius plot of area specific resistance (ASR) of the sample is plotted in Fig. 3.4 (marked as stars) and compared with other cathodes reported in literature (in triangles, circles and squares) [129-131]. Polarization resistance of the cathode in this study is at

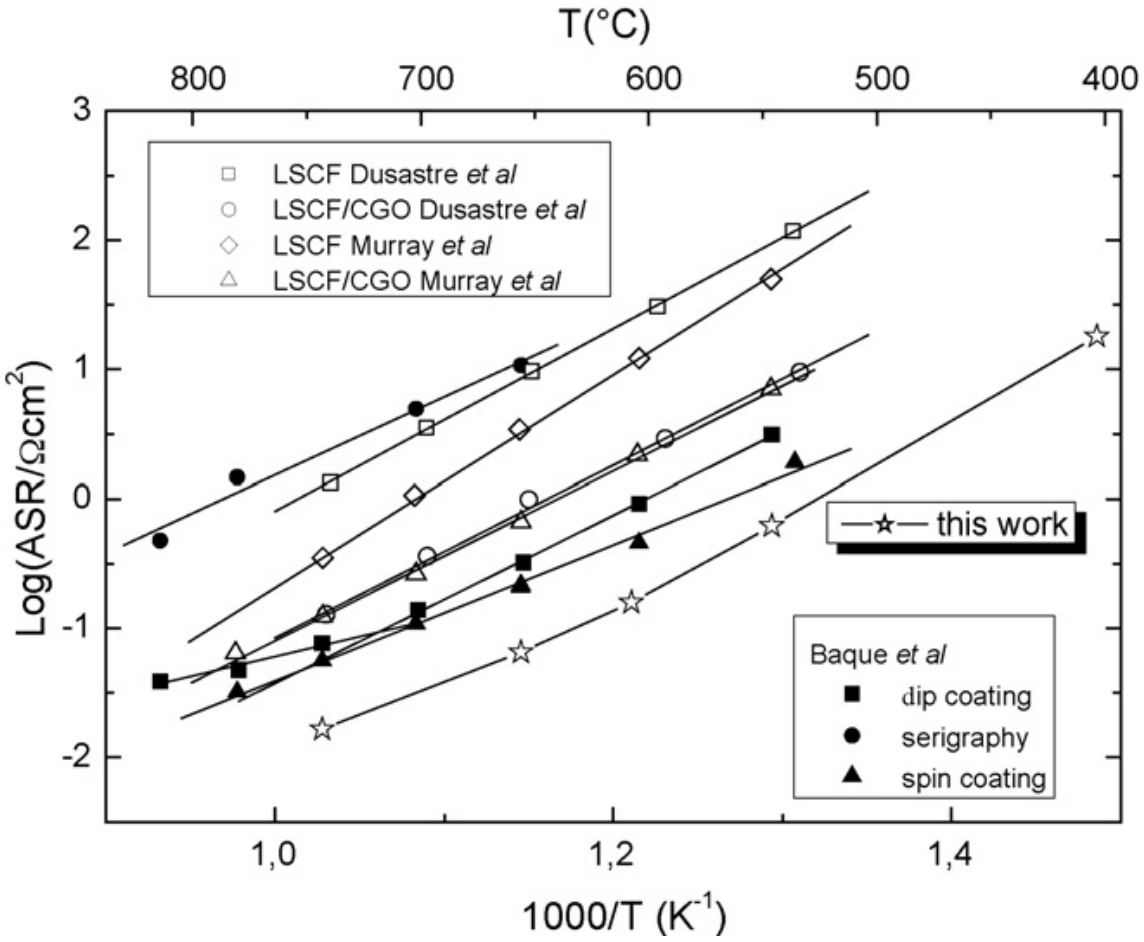

Fig.3.4. Arrhenius plot of area specific resistance (ASR) of LSCFO layer with VANP structure (stars) and other cathodes reported in literature by Dusastre et al. [129], Murray et al. [130] and Baque´ et al. [131]

least one order of magnitude lower than the reported polarization resistance of other cathode thin films with the same composition. This difference is much larger than the expected for the electrode resistance dependence with the film thickness or with oxygen partial pressure (PLD cathode was measured in pure oxygen while the reported polarization resistances of other cathodes were measured in air). A recent study on

numerical modeling of the electrochemically active zone in a mixed SOFC cathode suggests that by increasing the ionic conductivity we can increase the electrochemically active zone [123].

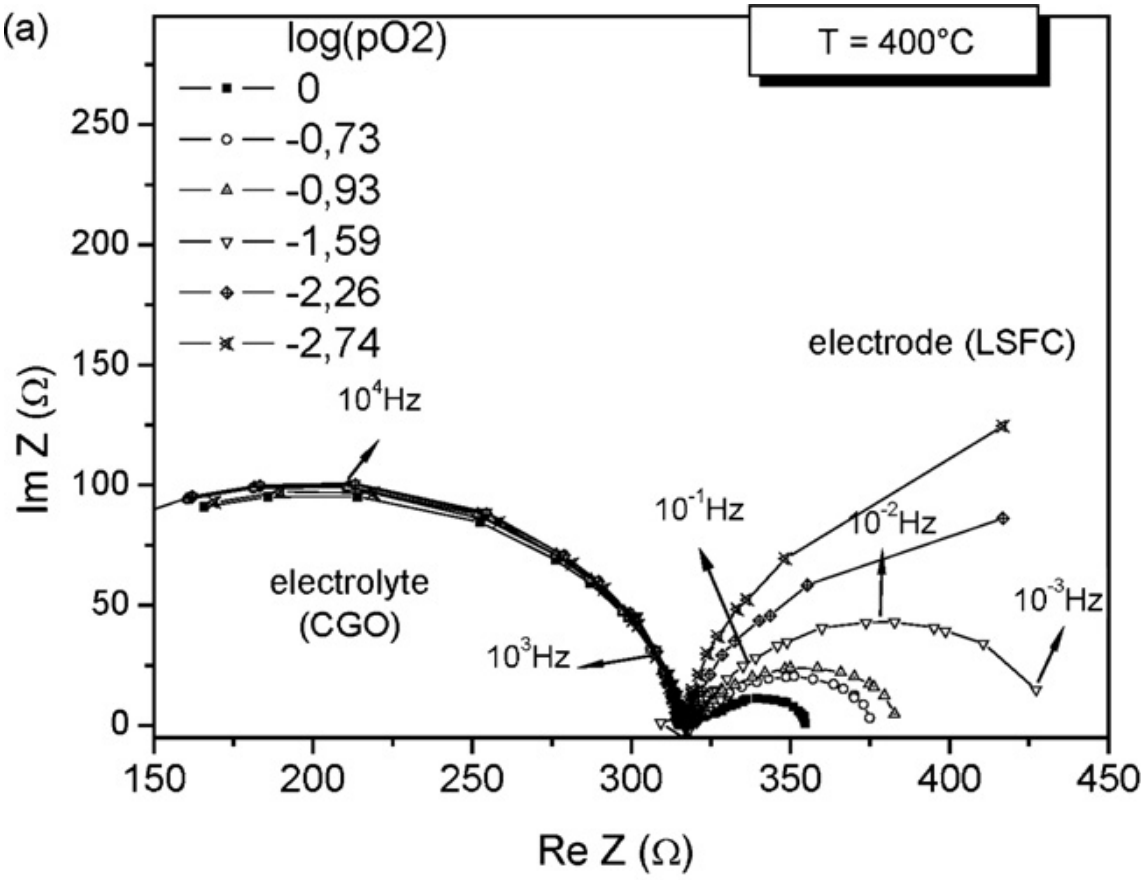

Fig.3.5. (a) Complex impedance spectra under different pO_2 values (ranging from 1 atm to 10^{-3} atm). (b) R_W, R_{LF} parameters and total polarization resistance, Rp, as a function of log(pO2). The dot-line is the linear fitting corresponding to log $R_{LF} \sim (PO_2)^{-m}$ (m = 0.495). The inset shows the equivalent circuit used for modeling the RIS data

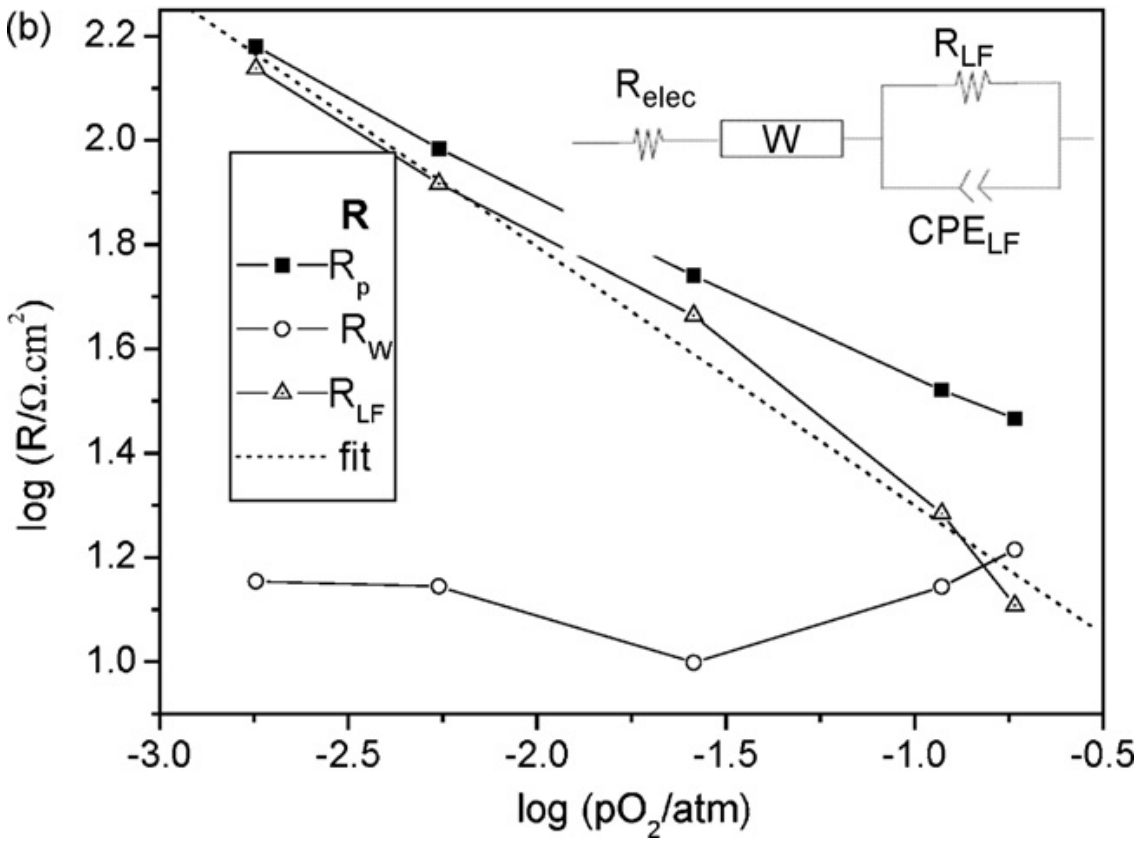

Fig.3.5. Continued,

It also implies that enhanced ionic conductivity will decrease the electrode polarization losses, which is evidenced by the low polarization resistance observed in our samples. The electrochemical oxygen surface exchange reaction at a mixed conducting electrode is a complex process comprising several individual steps in cathodic polarization, O_2 molecules from the gas phase diffuse to the gas/electrode interface, adsorb on the electrode surface and dissociate into two oxygen atoms. Finally, the oxygen is incorporated as O^{2-} into a vacancy in the first layer of the mixed conducting electrode. We have measured the complex impedance spectra under different pO_2 values (ranging

from 1 atm to 10^{-3} atm) at 400 °C to determine which of these processes is limiting the electrode reaction (shown in Fig. 3.5a). Using an equivalent circuit (insert in Fig. 3.5b) [132]. We found that the low frequency resistance fits the usual form log $R_{LF} \sim (PO_2)^{-m}$ with m ~ 0.5, expected for a dissociative surface-adsorption limited behavior, whereas according to some models, m = 1 is expected for an oxygen diffusion limited mechanism [133-134]. This indicates that a significant portion of the electrode surface is active for oxygen reduction. Impedance measurements for various nanopore size and densities samples are in progress to further understand this complex process.

3.5 Summary

We have successfully processed nanostructured LSCO and LSCFO cathode thin films for thin film SOFC. All the films grow as columnar grains, which leaves nanopores in between the grains. The unique VANP structures in these cathode thin films penetrate throughout the film thickness as deep as 2 μm and produce enhanced oxygen conductance in the cathode layer. Additionally impedance measurements demonstrate that the cathode thin films with VANPs have low polarization resistance values and enhanced kinetic performance in the low temperature regime (400–700 °C).

CHAPTER IV

VERTICALLY ALIGNED NANOCOMPOSITE THIN FILM AS CATHODE ELECTROLYTE INTERFACE LAYER FOR THIN FILM SOLID OXIDE FUEL

4.1 Overview

A thin layer of vertically-aligned nanocomposite (VAN) structure was deposited in between the electrolyte $Ce_{0.9}Gd_{0.1}O_{1.95}$ (CGO), and the thin film cathode layer $La_{0.5}Sr_{0.5}CoO_3$ (LSCO) for thin film solid oxide fuel cells (SOFCs). The VAN structure consists of the electrolyte and the cathode materials in the composition of $(CGO)_{0.5}$ $(LSCO)_{0.5}$. The self-assembled VAN nanostructures contain highly ordered alternating vertical columns formed through a one-step thin film deposition using a pulsed laser deposition technique (PLD). These VAN structures significantly increase the interface area between the electrolyte and the cathode as well as the area of active triple phase boundary (TPB), thus improve the overall thin film SOFC performance at low temperatures, as low as 400^{o}C, demonstrated by electrochemical impedance spectroscopy measurements. In addition, the binary VAN interlayer could act as the transition layer that improve the adhesion and relieve the thermal stress and lattice strain between the cathode and the electrolyte.

4.2 Introduction

Thin film solid oxide fuel cells (SOFCs) have been extensively researched because of their potentials in compact and high-efficiency energy conversion applications. SOFCs are the most promising alternate energy sources among other fuel cell types because they have wider fuel options and higher fuel efficiency when combined with heat processors. Although current SOFC technology made great progress, there are several technical challenges need to be addressed. For example, conventional SOFCs require relatively high operating temperatures, around 700~1000 ºC because of the low ionic conductivity of electrolyte at low temperature regime. This temperature limitation imposes a considerable amount of constraint on selecting cell component materials such as interconnect, electrode, and gasket materials, and ensuring structural integrity of a cell even after many thermal cycles. Further more, in order to achieve cost effectiveness and expand cell life time, it is also necessary to decrease the cell operating temperature down to 500ºC or lower [135]. However, at low temperature regimes the ionic conductivity of electrolyte decreases significantly. Recently the most promising way to regain the ionic conductivity at low temperature regimes has been reducing the electrolyte thickness, which is quite difficult to achieve for electrolyte-support SOFCs. In addition, as the electrolyte thickness decreases, the current flow between the anode and the cathode through the electrolyte can happen and the possibility of the fuel-oxygen intermixing increases. In this study, we introduce an alternate approach to this problem where a conventional electrolyte-support structure can still be used.

In this paper, a vertically aligned nanocomposite (VAN) layer in between the cathode and the electrolyte was intentionally built to effectively reduce the polarization resistance at the cathode/electrolyte interface. It was previously reported that the microstructural variations in the electrolyte and the electrode could affect the reaction kinetics of thin film SOFCs dramatically [136-141] and the main part of power losses in planar SOFCs occurs as a result of the polarization resistance at the cathode/electrolyte interface. The binary VAN interlayer is a composite of cathode and electrolyte materials, in our case, $La_{0.5}Sr_{0.5}CoO_3$ (LSCO) and $Ce_{0.9}Gd_{0.1}O_{1.95}$ (CGO). It is processed through a single step deposition without any additional lithography patterning steps. A schematic sketch of the binary VAN interlayer is given in Fig. 4.1a and b. This layer effectively increases the cathode-electrolyte interface area in a controllable way, and thus lowers the polarization resistance of the cathode/electrolyte interface and improves the kinetic performance of the cathode. These all lead to the improvement in the overall thin film SOFCs performance.

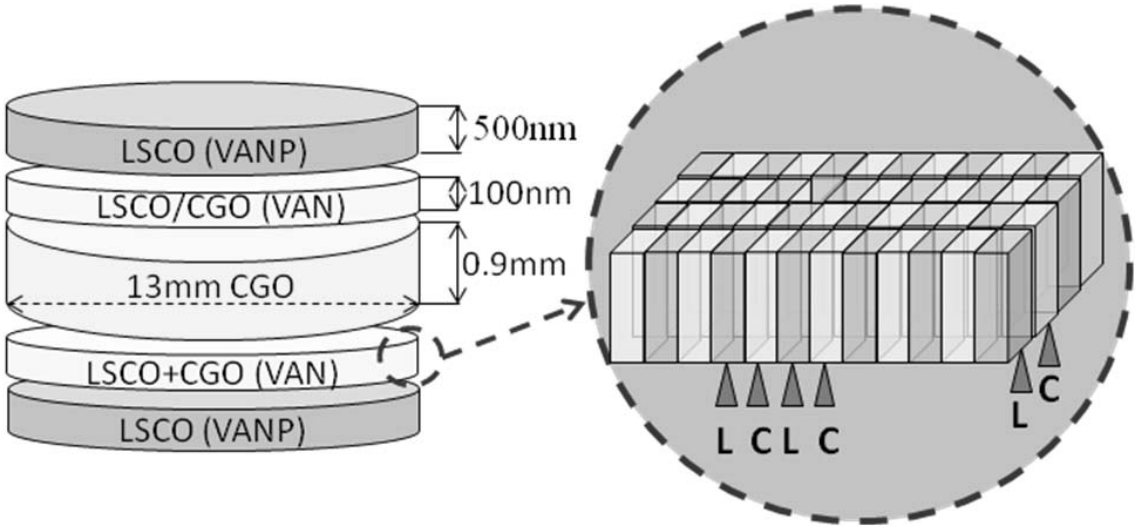

Fig.4.1. (a) Schematic diagram of a symmetric cell and (b) VAN interlayer where "L" and "C" stand for LSCO and CGO columns, respectively

4.3 Experimental

Pulsed laser depositions (PLD) of the LSCO/CGO VAN interlayer and the following LSCO cathode layer were performed in a multitarget chamber with a KrF excimer laser (Lambda Physik 210, λ = 248 nm, 5-10 Hz). Various substrates including Yttria-stabilized Zirconia (YSZ), $SrTiO_3$ (STO) and pressed CGO disks were selected for this work. The laser beam was focused to obtain an energy density of approximately 10J cm^{-2} at 45º angle of incidence. The hot-pressed targets including LSCO and LSCO+CGO (50:50), and CGO electrolyte disks were all prepared by mixing the stoichiometric amounts of powders including La_2O_3, $Sr(NO_3)_2$, Co_3O_4, CeO_2 and Gd_2O_3. LSCO/CGO VAN interlayers (about 50–100 nm) were processed through one-step thin film

deposition. Subsequent LSCO thin film cathode layer with vertically aligned nanopores (about 500nm) (VANP) was deposited under the condition stated in our previous work [142]. The growth rate for these thin films was controlled at about 1 nm/s for LSCO cathode layer and 0.1 nm/s for LSCO/CGO VAN interlayer at an oxygen partial pressure of about 200 mTorr. The substrate temperature was varied from 300–700 ºC to optimize the film crystallinity and the nanopore size of the cathode layer. Four symmetrical working cells with different VAN thicknesses were prepared to study the effects of interlayer thickness on cell performance. Microstructural characterizations of these films were performed by cross-sectional transmission electron microscopy (TEM) using a JEOL2010 analytical electron microscope and a JEOL3000F analytical electron microscope with a point to point resolution of 0.18 nm. Scanning transmission electron microscopy (STEM) was performed by a FEI Tecnai F20 with a point to point resolution of 0.27nm. Surface morphology study for the thin films was conducted by scanning electron microscopy (SEM). Impedance spectroscopy measurements were carried out on heating from 400 to 600 ºC in pure oxygen by steps of 50 ºC, by using a potentiostat/impedance analyzer Autolab (Eco Chemie BV) between 10^{-3} and 10^{6} Hz. Each temperature was measured after 3-8 hours waiting until the system was stable. The electrochemical cells were prepared with the symmetrical configuration and platinum grids, slightly pressed on porous electrodes, were used as current collectors.

4.4 Results and Discussion

Cross-sectional TEM images of a typical LSCO/CGO VAN interlayer structure are shown in the TEM images in Fig. 4.2a and 4.2b. Fig. 4.2a shows the large areal view of the VAN structure deposited at 650 ºC on STO substrate.

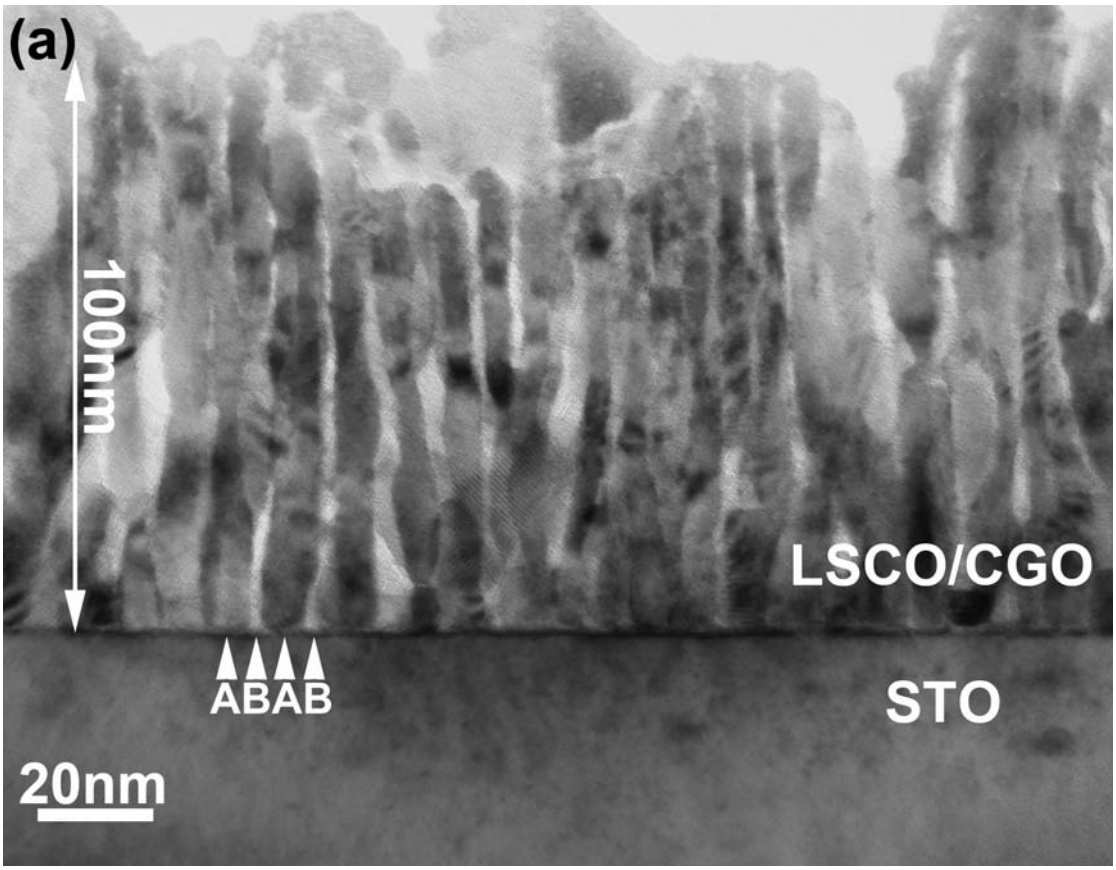

Fig.4.2. Cross-sectional (a) low magnification and (b) high resolution TEM images, and (c) STEM image of a typical LSCO/CGO VAN structure grown by PLD on STO substrate

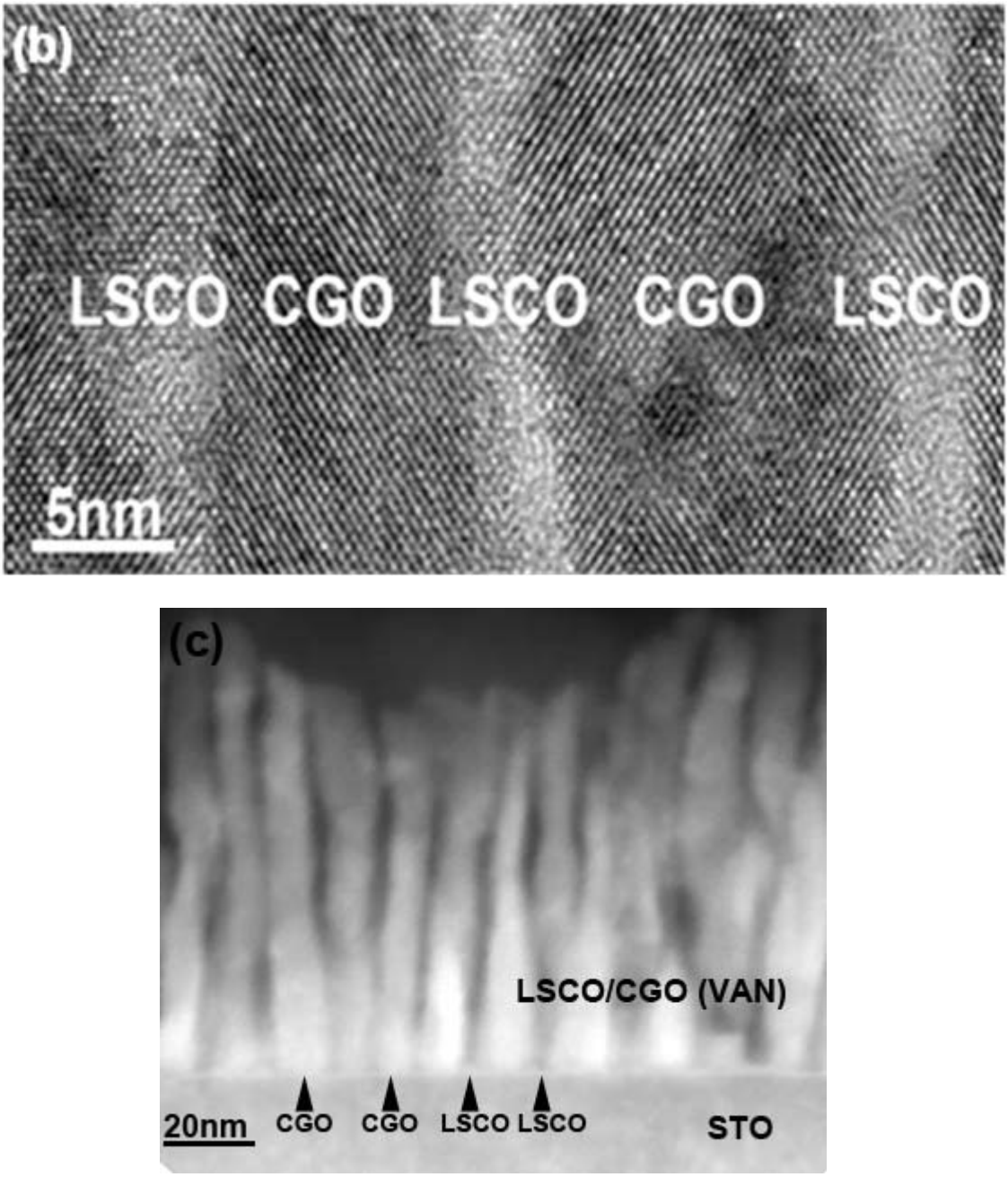

Fig.4.2. Continued,

It is clear that CGO and LSCO grains grow as alternating vertically aligned columns over a large area. Each of the columns is around 10 nm in diameter. The VAN structure extends all the way through the film thickness, in this case, 100 nm. The reason that we chose single crystal YSZ and STO substrates first to grow the VAN structure is to demonstrate the growth of the binary VAN structures of LSCO/CGO. LSCO has a perovskite structure with a lattice parameter of 0.381 nm and CGO is face-centered cubic with a lattice parameter of 1.084 nm (2×0.542 nm). Both of them match well with YSZ (a= 0.515 nm) and STO (a=0.390 nm), either through direct cube-on-cube matching or after 45^o rotation. Another important consideration is that the possibility of intermixing between LSCO and CGO is rather small as their cations are rather big and the interstitial sites are relatively small. Previously we have successfully demonstrated the growth of $BiFeO_3$ / Sm_2O_3 VAN structure on STO substrate and LSMO/ZnO VAN structure on sapphire with similar materials selection criteria [143-145]. A high resolution TEM image covering a set of VAN columns is shown in Fig. 4.2b. LSCO/CGO binary VAN structure can be clearly observed (labeled as LSCO and CGO) based on their contrast difference.

To confirm that LSCO and CGO grow as alternative columns without intermixing, we conducted STEM study under the high angle annular dark field (HAADF) condition. This is also called Z-contrast, where the contrast is roughly proportional to Z^2 (more accurately, $Z^{1.7}$). A typical Z-contrast image over a large area of the LSCO/CGO VAN structure is shown as Fig. 4.2c. Because of higher Z numbers of Ce and Ga, CGO

columns have much higher contrast (brighter columns) than LSCO columns. The CGO and LSCO columns are clearly vertically aligned and alternating with each other with an average column size of 5-10 nm. The vertical column interfaces are sharp and clean. We also conducted a detailed EDX mapping over the same area (not shown here) and no obvious intermixing was detected under the EDX detecting sensitivity.

In order to measure the electrochemical characteristics and test the performance of the cathode structure with the VAN interlayer, we processed the symmetric cells with the VAN interlayer deposited on both sides of a pressed CGO disk followed by depositing thin film cathode with VANP as illustrated in Fig.4.1. The total cathode thickness is about 600 nm on both sides. We used the same deposition conditions to ensure the identical properties for both sides of the cells. Four button cells with different VAN interlayer thicknesses were prepared in order to investigate the relationship between the VAN thickness and the electrochemical performance of the cells. The VAN structure can effectively increase the cathode-electrolyte interface area in a controllable way. The information on the VAN film thickness and the ratio between the interface area densities with and without the VAN layer is summarized in Table 4.1. For example, the 100nm-thick VAN structure can increase the interface area 25 times compared with the case without the VAN interlayer. By controlling the interlayer thickness, one can systematically vary the interface area density. For this typical VAN structure, the average width of these nano-columns are about 5~10 nm. It is interesting to note that by controlling the deposition conditions such as temperature and the stoichiometry of the

binary target, it is possible to vary the width of the VAN structure [145]. JY133 is a reference cell with only the VANP structure, while JY125, JY128, and JY129 have both the VANP and VAN structures. JY128 has twice of the VAN layer thickness as that of JY125 and JY129 has the same VAN thickness as the JY125 but with an additional thin film CGO layer (~500 nm) in between the VAN interlayer and the CGO disk. The additional thin film CGO layer serves as a seed layer for the subsequent VAN interlayer and provides a much smoother surface for the growth of the subsequent thin film VAN interlayer.

Table 4.1

List of the VAN layer thickness and the ratio of the interface area density between with and without the VAN layer for different samples

Sample ID	**Thin Films on CGO disk**	**Film Thickness**			**Ratio of the interface area density**
		VANP (nm)	**VAN (nm)**	**CGO (nm)**	
JY125	VANP/VAN	500	50	0	13.7
JY128	VANP/VAN	500	100	0	25.3
JY129	VANP/VAN/CGO	500	50	500	13.7
JY133	VANP	500	0	0	1

Cross-sectional TEM images of one of the symmetric cells, JY128 (LSCO / LSCO+CGO / CGO disk), are shown as Fig. 4.3a and b. Fig. 4.3a shows a cross-sectional TEM image of the LSCO cathode and VAN interlayer deposited at 300 ºC and 650 ºC, respectively, on a CGO disk. It shows that, over a large area, the VAN interlayer grows as a smooth and dense layer with the film thickness of about 100nm thick. On the top of the VAN layer, the LSCO cathode layer grows as porous columnar film with the pores vertically aligned in the film. From Fig. 4.3b an obvious surface roughness is observed in the cathode layer. The roughness is originated from the uneven surface of the CGO disk before deposition. The LSCO cathode layer has columnar grains with an average grain size of 100–200 nm. Vertically-aligned nanopores can be clearly observed (marked as white arrows) (Fig. 4.3b). The total cathode thin film thickness including VAN interlayer in this sample is about 600 nm. A typical SEM image (Fig. 4.3c) on the surface of the top cathode layer (JY128) shows the grain structure with nanopores in between the columnar grains. From the view area, no micro crack was observed at the film surface after the thermal cycle during thin film depositions. We believe that the binary VAN interlayer acts as a transition layer thus effectively relieve or partially relieve the internal thermal stress and lattice strain between the cathode layer and the electrolyte. The interlayer can also improve the adhesion between the cathode and the electrolyte.

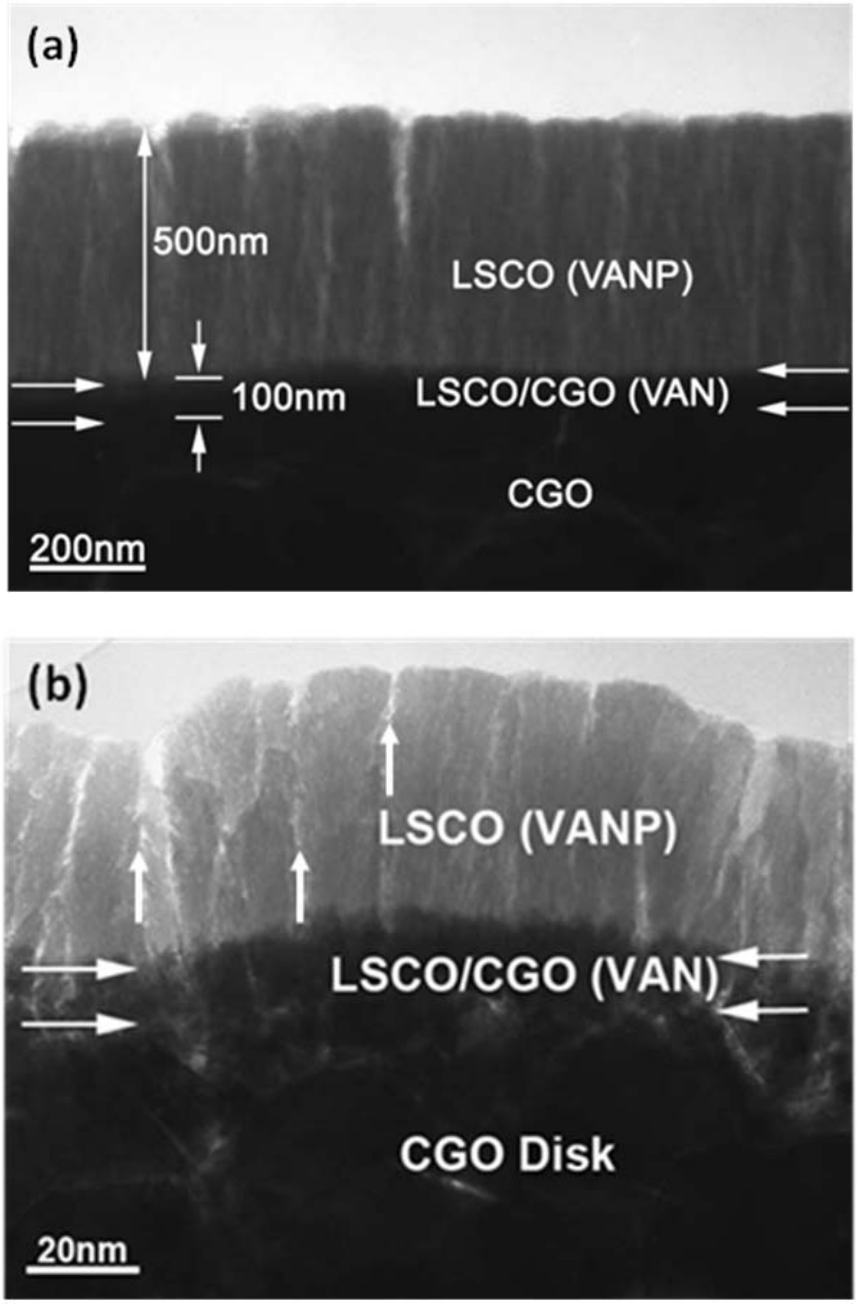

Fig.4.3. (a) Low magnification cross-sectional TEM image of a LSCO cathode and VAN interlayer on a pressed CGO disk, (b) a closer view of the VAN interlayer structure on the CGO disk, and (c) SEM image showing a smooth surface of the cathode layer without microcrack formation

To test the performance of the thin film cathode with binary VAN interlayer, we measured the complex impedance spectra in oxygen in the range 400–600 °C for all the symmetric cells. The criteria adopted for electrode polarization resistance determination is shown in Fig. 4.4. The beginning of the electrode polarization resistance was determined by fitting the electrolyte spectrum with a circuit consisting of a resistance and constant phase element (CPE) connected in parallel. Fitting was performed with the ZView 2.8d program. For higher temperatures (higher than 550-600°C), when electrolyte spectrum is not observed, the beginning of the electrode polarization resistance was considered as the high frequency interception of the spectrum with the Z' axis. The end of the polarization resistance was calculated as the average of low frequency impedance module, when it becomes approximately constant. Error was estimated taking into account the error of electrolyte fitting and the difference between the average and the extreme value (maximum or minimum) of data considered to calculate the end of the electrode polarization resistance. Area specific resistance (ASR) of cathodes was determined according to the following formula for a symmetric cell:

$$ASR = R_p\, A/2$$

Where, R_p the cathode polarization resistance and A is the geometrical cathode area.

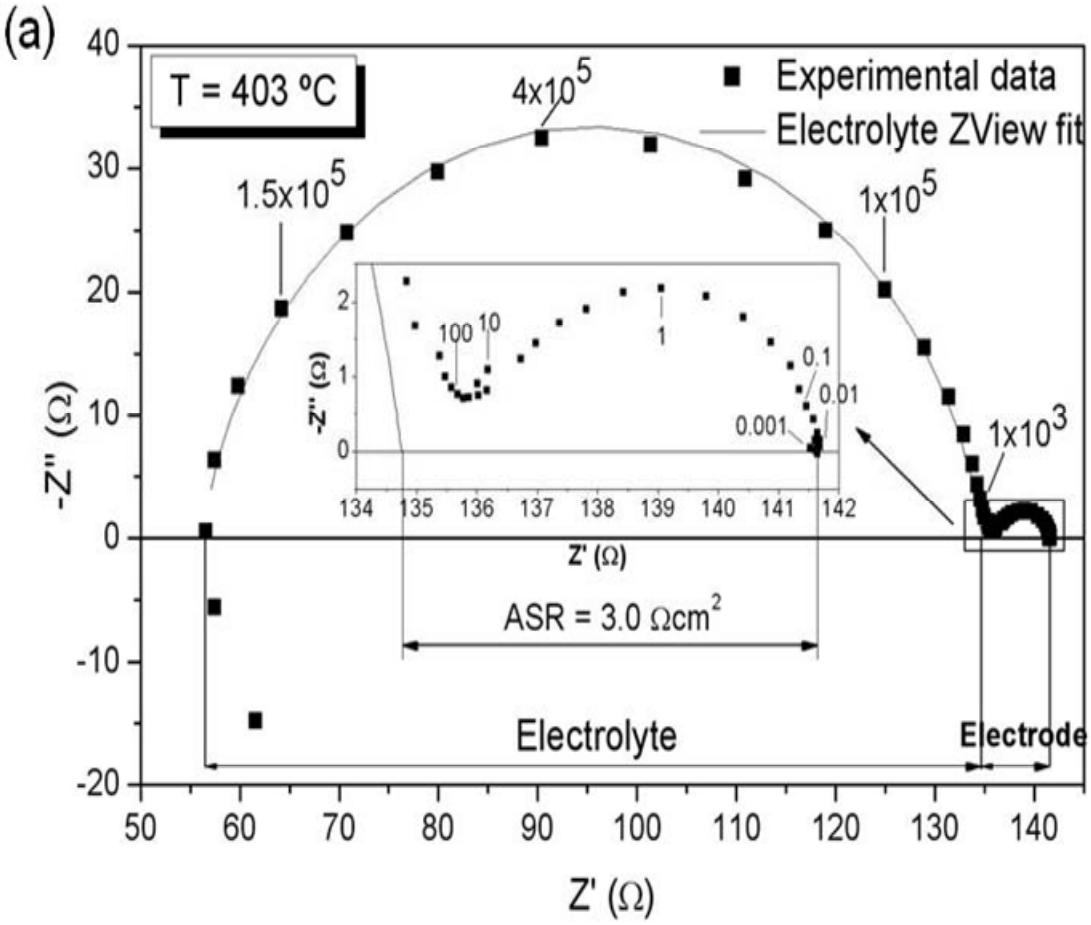

Fig.4.4. Criteria adopted for electrode polarization resistance determination (A) Nyquist plot. Inset shows a zoom of electrode spectra. Numbers in spectra indicate measuring frequency. (B) Bode plot

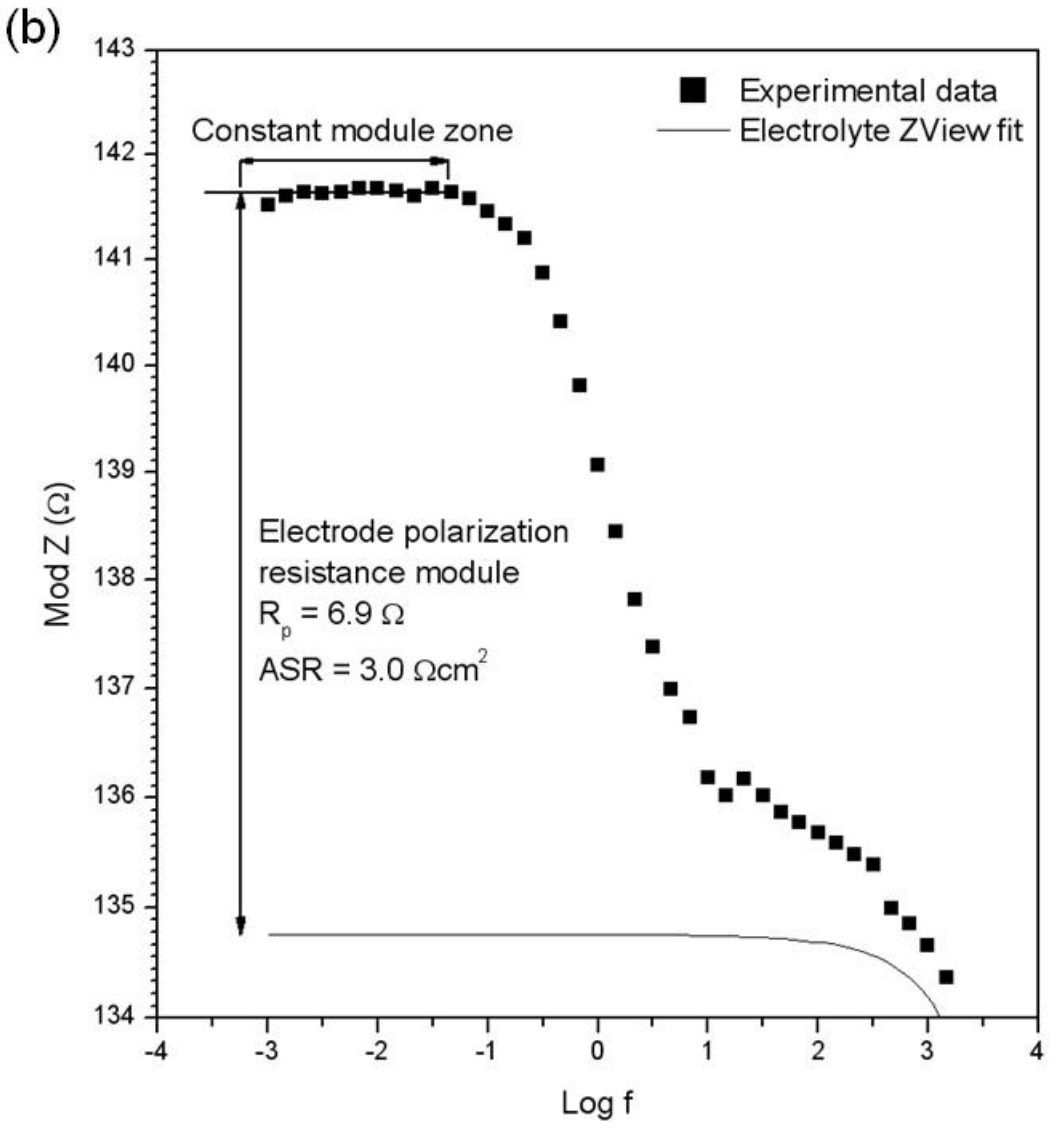

Fig. 4.4. Continued,

Arrhenius plot of area specific resistance (ASR) versus temperature of all the samples with different VAN interlayer thicknesses is plotted in Fig. 4.5 and compared with our previous work (VANP cathode layer only, marked as black triangles)[142]. In our previous work we have demonstrated that VANP structure can help oxygen gas phase

diffuse to reaction sites thus enhance the total electrochemical activity at the reaction sites. It is obvious that, at 400 ^{o}C, the ASR is only about 3.5Ωcm^2 for JY128 with a 100nm VAN interlayer. Hence, in this work we have further lower the ASR at

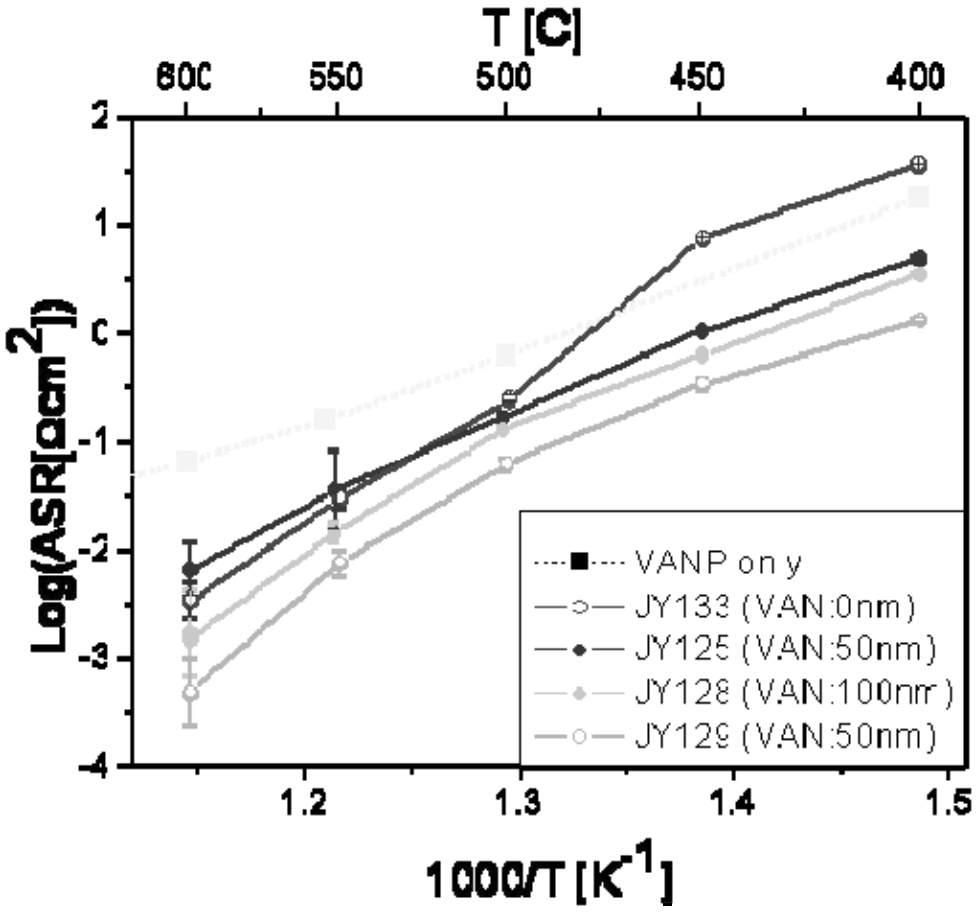

Fig.4.5. ASR of symmetrical cells with VANP/VAN structures on CGO disks grown by PLD

least one order of magnitude than our previous work by including the binary VAN interlayers. Data measured above 550 °C have a big error due to the small resistance. Considering the fact that iron or manganese doped LSCO cathodes demonstrate better performance than simple LSCO cathodes, this work suggests that doped LSCO cathodes can improve the fuel cell performance even further by inserting the VAN interface layer. Fig. 4.5 indicates the general trend of ASR as a function of the VAN thickness, i.e., the ASR plot shifts to lower values as the VAN interlayer thickness increases. This suggests that the VAN interlayer indeed plays a very important role in the ASR decrease. As listed in Table 4.1, the cathode / electrolyte interface area density increases as the VAN interlayer thickness increases. Therefore the VAN interlayer enhances the catalytic reaction probability of TPBs (gas–cathode–electrolyte boundaries) by increasing the effective area of the TPBs, and thus decreases the cathode resistance and lowers the polarization resistance of the cathode/electrolyte interface, which leads to the overall improved thin film SOFC performance. It is noted that, the results reproduce well at different temperatures after the high temperature thermal cycles during the measurement. We can therefore conclude that, there is no significant structural degradation (second phase formation or interface diffusion) for the cells with the VAN interlayer and the VAN structure is stable after thermal cycles.

JY129 (with an additional CGO seed layer) shows the lowest ASR, which is about 35% lower than that of JY125 (no CGO seed layer). This supports the effectiveness of the additional thin film CGO layer. The possible functions of the CGO seed layer are: (1)

improving the gas tightness of hot pressed 0.9mm thick CGO electrolyte, (2) preventing interface reactions, such as the formation of insulating La-composite at the interface between electrolytes and cathode materials, and possibly, (3) improving the charge transfer process at the electrode and the electrolyte interface [146]. The effect of the CGO layer became more obvious at lower temperature regime than that at the high temperature regime. This is because that, the grain boundary effects become significant at the intermediate temperature regime, 400 ºC to 600 ºC, since the grain boundary region has lower ionic conductivity and higher activation energy than the bulk lattice[147]. However, at higher operating temperature, above 700 ºC, the grain boundary effect can be negligible because of high enough temperatures to overcome the high activation energy.

4.5 Summary

We have successfully processed binary VAN interlayer of $(LSCO)_{0.5}$ $(CGO)_{0.5}$ in between the cathode and electrolyte for high efficiency thin film SOFC. This unique binary VAN structured interlayer effectively increases the cathode/electrolyte interface area density (by 14~25 times depending on the interlayer thickness) and thus significantly lowers the polarization resistance present at the cathode/electrolyte interface. Hence a low cathode polarization resistance ($9x10^{-4}$ Ω at 599^{o}C, 2.39 Ω at 400^{o}C) was achieved at low operation temperatures based on the impedance measurements at low temperature regime (400~600 ºC). The interface area density can

be systematically controlled by varying the VAN interlayer thickness and column width, which can be achieved through tuning the deposition parameters. As the VAN thickness increases, the ASR shifts to lower values. By combining a CGO seed layer with the VAN interlayer, we have demonstrated a record low ASR (4.84×10^{-4} Ωcm^2 at 599°C, 1.25 Ωcm^2 at 400°C).

CHAPTER V

MICROSTRUCTURAL STUDY OF THIN FILM $Ce_{0.90}Gd_{0.10}O_{1.95}$ (CGO) AS ELECTOROLYTE FOR SOLID OXIDE FUEL CELL APPLICATIONS

5.1 Overview

The microstructural properties and growth mechanisms of $Ce_{0.90}Gd_{0.10}O_{1.95}$ (CGO) thin film as electrolyte prepared by pulsed laser deposition technique were investigated. The CGO thin films on single crystal Yittria-stabilized Zirconia (YSZ) substrates with the film thickness from 1.5μm to 6.7μm were prepared. Thin film CGO electrolytes with different grain sizes and crystal structures were prepared under different deposition conditions. The effect of the deposition conditions, such as substrate temperature, oxygen partial pressure, target repetition rate, and laser ablation energy on the microstructural properties of these films are examined using X-ray diffraction (XRD), transmission electron microscopy (TEM), scanning electron microscopy (SEM), and optical microscopy. CGO thin film deposited above 500 ºC starts to show epitaxial growth on YSZ substrates. The present study suggests that substrate temperature significantly influences the microstructure of the films especially film grain size.

5.2 Introduction

Solid oxide fuel cells (SOFCs) offer an environmentally friendly alternative to conventional energy conversion devices [148]. A typical SOFC consists of two electrodes (anode and cathode) separated by an electrolyte. Yttria-stabilized zirconia (YSZ) is considered to be the most reliable candidate as the electrolyte and has been widely used. However, for YSZ to acquire sufficiently high oxygen ion conductivity, a high operating temperature, typically around 1000 ˚C, is required, which severely limits the component material selections and decrease the long term performance stability of SOFCs [149]. Therefore, it is necessary to lower the operating temperature from the traditional 1000 ˚C to an intermediate/low temperature range of 400–700 ˚C. The lower temperature of application provides a greater flexibility in the choice of electrode and interconnects materials, reduction in thermal stresses in active ceramic structures, as well as a longer lifetime of the cells. However, significant barriers to intermediate/low temperature SOFCs are the increase of electrolyte resistance and high electrode overpotentials. There have been three different approaches to address these problems: the first is to decrease the electrolyte thickness [150-152] and the second is to develop new electrolyte materials with high ionic conductivity at low temperature regime such as $Ce_{0.90}Gd_{0.10}O_{1.95}$ (CGO) or $LaGaO_3$ [153-160] and the last is to reduce the electrode polarization resistance [161-162]. So far the most successful approach to obtain the required reduction in the operating temperature is to combine the thin film fabrication

technique with the employment of electrolyte materials having higher oxide ion conductivity [163].

Considerable effort has been made on the development of low temperature SOFCs based on thin film electrolyte of doped ceria (CeO_2) [157, 158]. The use of thin film electrolyte has been considered as a promising approach for improving fuel cell performance by reducing the overall device resistance and the operation temperature. Electrolyte materials are desired to be dense and highly conductive for specific ions because electrolyte serves as a gas tight membrane to separate fuel from air and selective ion conductor which can only conduct oxygen ions therefore it has to be a dense as well as thin layer. However it is usually difficult to obtain a dense structure of thin film CGO electrolyte using conventional methods such as tape casting, screen printing, dip coating, or dry pressing if any property of the doped ceria powder is not properly controlled.

Pure cerium oxide is not a fast oxygen ion conductor unless it is doped with divalent or trivalent cations, especially trivalent rare earth ions. The introduction of these cations to the host lattice can increase the oxygen vacancy concentration and at the same time improve oxide ion conductivity in cerium oxide. Y_2O_3, Gd_2O_3, and Sm_2O_3 are the usual dopants, which can significantly enhance the ionic conductivity of cerium oxide [164]. CGO has given much attention because of its great potential application as the electrolyte in intermediate temperature SOFCs [165]. In comparison with YSZ, CGO has significantly higher ionic conductivity at temperature range below 600 ˚C where the

electronic contribution in reducing condition is small. The addition of gadolinia into ceria can be written in Kroger–Vink notation [166] as in equation 5.1.

$$Gd_2O_3 \rightarrow 2Gd_{Ce} + 3O_O^X + V_O^{"} \qquad (5.1)$$

It is generally accepted that the ionic conductivity is at its maximum at a certain doping level and above this level of doping the ionic conductivity decreases because of defect ordering, vacancy clustering, or electrostatic interaction. At a grain boundary the dopant concentration is higher than the matrix because of lower energy state for the dopant atoms therefore the ionic conductivity is lower in CGO with larger grain boundary than the ones with bigger grain boundary.

In this report we prepared CGO thin films with different grain sizes by pulsed laser deposition (PLD) technique. The effects of substrate temperature on microstructural properties including grain size, crystal orientation, and surface morphology are investigated.

5.3 Experimental

Depositions of the CGO thin film electrolyte layer were performed in a vacuum chamber with a KrF excimer laser (Lambda Physik 210, λ = 248 nm, 5 Hz). The energy range used for the target ablation was 390 ~400 mJ/pulse and the laser beam incident angle

was kept at 45˚. The focused laser beam energy density is approximately 10 J cm^{-2}. During deposition target was rotated and height of the target was adjusted for uniform deposition rate through out the deposition process.

Yttria-stabilized zirconia (YSZ) single crystal substrate was selected for this experiment because of its close lattice parameter match with CGO. The hot-pressed CGO target was prepared by mixing the stoichiometric amounts of powders including CeO_2, and Gd_2O_3. All of the compounds were mixed and ground in a mortar and pestle with 1 wt% of poly-ethylene glycol (PEG) as a binder for one hour and then ball milled for another two hours. The ball milled powders were then uniaxially pressed into pellets of 33mm diameter and 6mm in thickness at a pressure of 5tons/cm^2 using hydraulic press. These pellets were sintered at 1200 °C in a tube furnace for 10 hours in air at a ramping rate of 3˚C/min.

Thin film CGO electrolyte layers (about 1.5 μm–6.7 μm) were deposited through one-step thin film deposition using pulsed laser deposition technique. The growth rate for these thin films was controlled at about 1.7~7 nm/s at an oxygen partial pressure of about 200 mTorr. The substrate temperature was varied from room temperature (RT) to 700 ºC to study the temperature effect on the microstructural change and the grain size change of the of the thin film electrolyte layer. Microstructural characterization of these thin films were performed by cross-section transmission electron microscopy (TEM) using a JEOL2010 analytical electron microscope, a JEOL3000F analytical electron

microscope with a point to point resolution of 0.18 nm and X-ray diffraction (XRD) to study the film orientations and crystallinity. The thicknesses of the deposited films were measured using TEM images. The deposition parameters used are given in table 5.1.

Table 5.1

Typical deposition parameters

Parameters	**Deposition Conditions**
Laser	KrF excimer (λ=248 nm)
Pulse duration	25 ns
Repetition rate	5Hz
Laser energy	390–400 mJ/pulse
Energy density	10 J/cm^2
Target	Sintered 10 mol% Gd-doped CeO_2
Substrate	YSZ single crystal
Substrate temperature	300–973 K
Target-substrate spacing	45 mm
Base pressure	2.5x10^{-6} mbar
Oxygen partial pressure	200mTorr

5.4 Results and Discussion

Thin films of CGO were prepared at different substrate temperatures. All the films were deposited at 390~400 mJ/pulse laser energy, 200mTorr background O2 pressure, and 5Hz repetition rate for 15 minutes. Table 5.1 summarizes the detailed deposition conditions. The typical thicknesses of the films deposited on YSZ substrates under the above deposition conditions were about 1.5~6.7 μm. In PLD each laser pulse provides target material with sufficient energy to grow only a sub monolayer of the desired phase. The film growth mechanism depends on multiple factors such as target to substrate distance, substrate temperature, laser ablation energy, and background oxygen pressure. Among those process factors the substrate temperature is one of the most critical factors in deciding film growth mechanism.

In this work, 10 mol% doping is chosen because at this doping level CGO shows the highest lattice ionic conductivity around 500 ºC region even though the maximum grain boundary conduction occurs at a composition of around 25% $GdO_{1.95}$. We are focusing on growing defect free epitaxial layer. It is known that the grain boundary region has a lower ionic conductivity than the lattice and higher activation energy. Operating temperature above 700 ºC these grain boundary effects become insignificant because of high enough temperature to overcome high activation energy but in the intermediate temperature regime, 400 ºC to 600 ºC it becomes significant. However, electrolyte

materials deposited at lower temperature has smaller grain size than the ones deposited at higher temperature because adatoms have lower mobility at lower temperature.

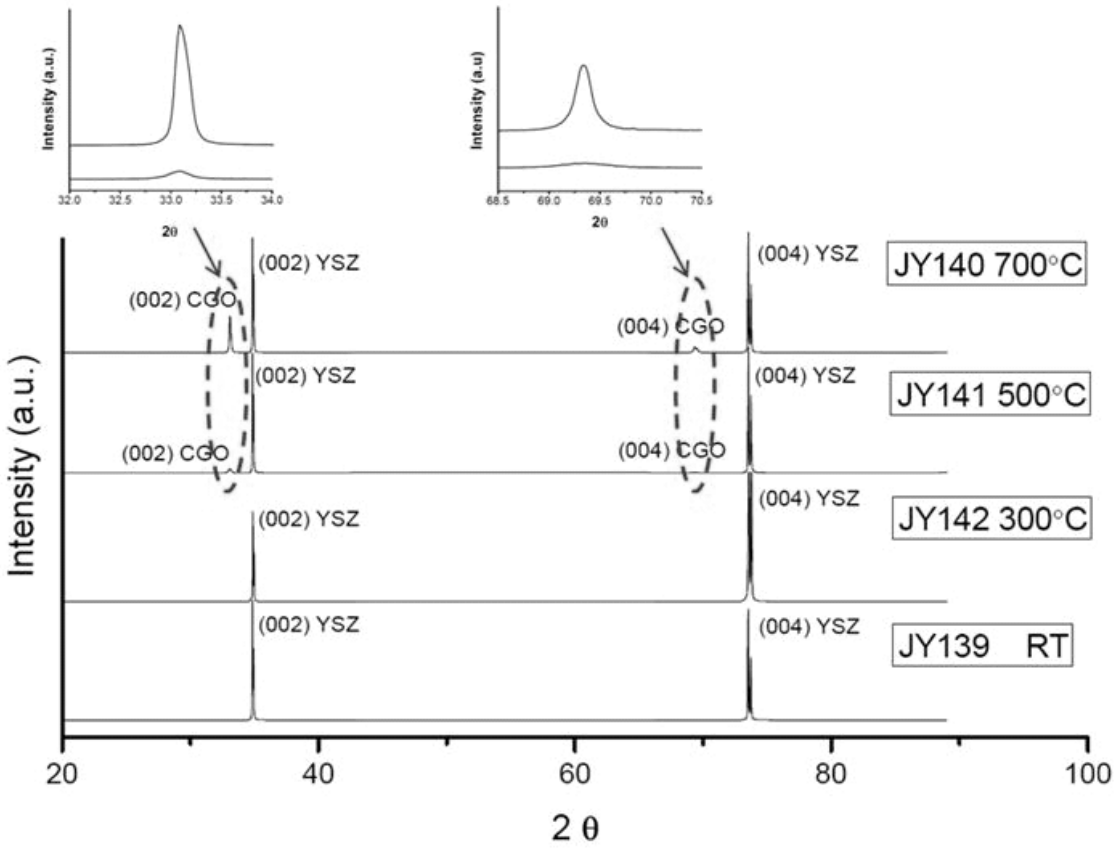

Fig.5.1. XRD patterns of $Ce_{0.9}Gd_{0.1}O_{1.95}$ thin film deposited on YSZ substrate at different temperatures

Figure 5.1 shows the XRD patterns for the CGO thin film samples containing 10 mol% of gadolinia deposited at RT, 300 ºC, 500 ºC, and 700 ºC on YSZ (100) single crystal substrate. The XRD pattern revealed textured growth starts at 500 ºC and strong (002)

and (004) CGO peaks can be observed at 700 ºC. Insets show enlarged images of the CGO peaks. No secondary or impurity phases were observed for the high temperature depositions. It suggests that for the given doping concentration of gadolinia, the deposition temperature of 500 ºC is adequate to ensure the formation of epitaxial CGO thin films. The crystallinity of the films increases with increasing substrate temperature. The YSZ substrate with <001> orientation has a close matching with CGO, the substrate peaks are found to match with CGO for (002) and (004) reflections. The lattice parameter of CGO and YSZ is 0.5418 nm and 0.5148 nm respectively therefore, YSZ will have a close match with CGO with a cube-on-cube matching relation. The resulted mismatch is about 5%.

The surface morphology of as-deposited CGO thin films were studied by optical microscopy. Figure 5.2a - d, show the optical micrographs of CGO thin films deposited at four different temperatures. The images show that the grain size increases as the deposition temperature increases because of the increased adatom mobility with increasing substrate temperature. At room temperature the average grain sizes are about 5 μms and at 300 ºC the sizes increased to 10 μm. Unlike the samples of low temperature conditions from those samples deposited at 500 ºC and 700 ºC no detectable grain boundaries could be found from optical microscope observations.

Large area cross section TEM images of the all four samples can be seen from figure 5.3. These images show the actual film thicknesses of the each sample. From this figure we

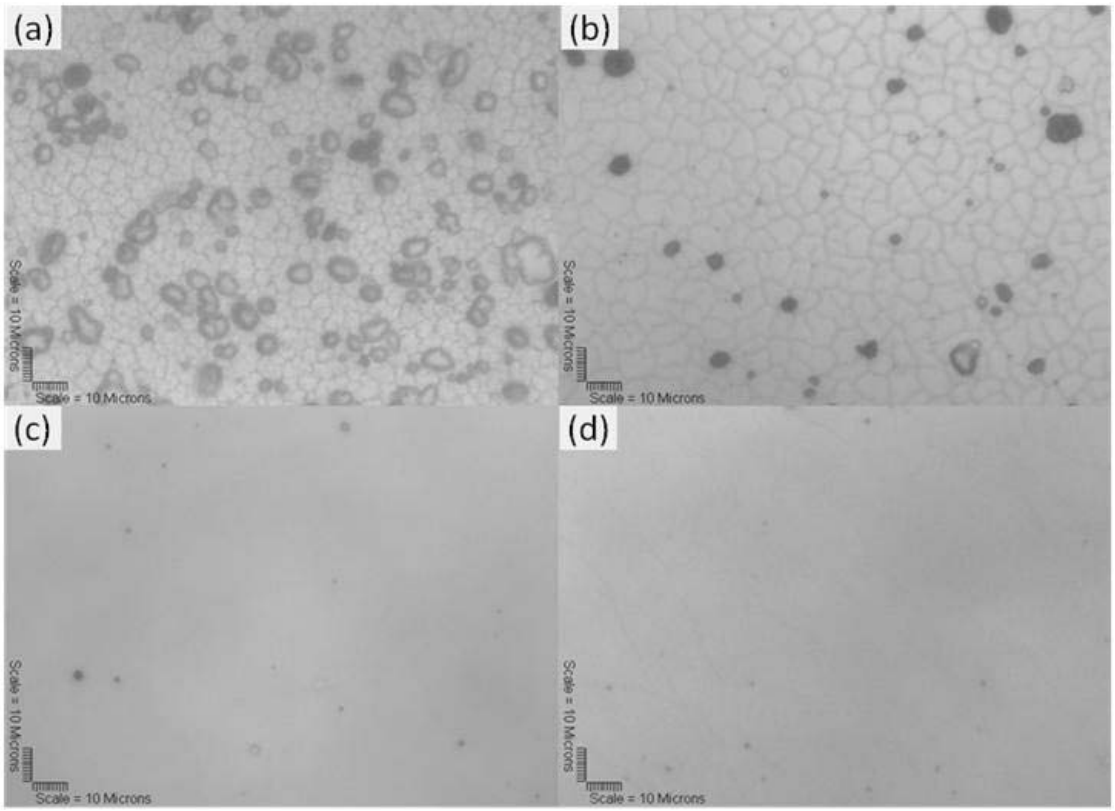

Fig.5.2 Optical images of microstructure of as deposited CGO thin films deposited at (a) RT, (b) 300 ºC, (c) 500 ºC, and (d) 700 ºC on YSZ substrates

can calculate the growth rate at each temperature. Table 5.2 lists typical growth rates of the thin CGO films at different temperatures. At low temperature regime growth rate is as high as 7.4 nm/s. This is due to low density of the film deposited at low temperature. Again as deposition temperature increases film density also increases and this can be assumed from highly epitaxial TEM images of samples JY141 and JY142. Figure 5.4 is the corresponding plot of the growth rate as a function of the deposition temperature.

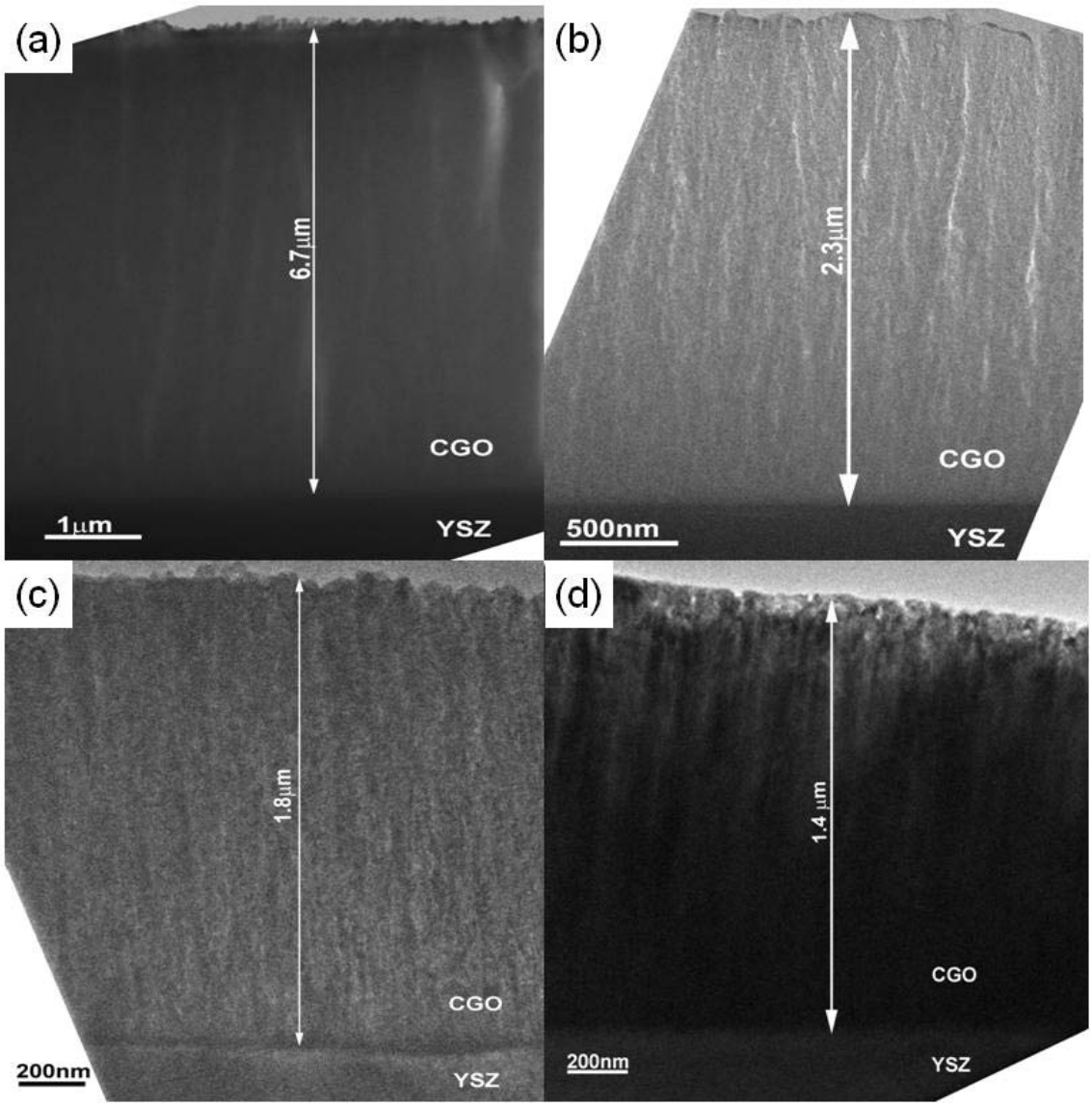

Fig.5.3. Low magnification cross section TEM images of CGO thin films deposited at (a) RT, (b) 300 ºC, (c) 500 ºC, and (d) 700 ºC

As the deposition temperature increases the growth rate decreases fast and above 500 °C it shows very slow decrease because of increased crystallinity.

Table 5.2

Film thicknesses and growth rate at different temperatures

Sample ID	Deposition Temperature	Film Thickness	Deposition time [mins]	Deposition Rate [nm/s]
JY139	RT	6.7µm	15	7.4
JY140	700ºC	1.5µm	15	1.7
JY141	500ºC	1.8µm	15	2
JY142	300ºC	2.3µm	15	2.6

.

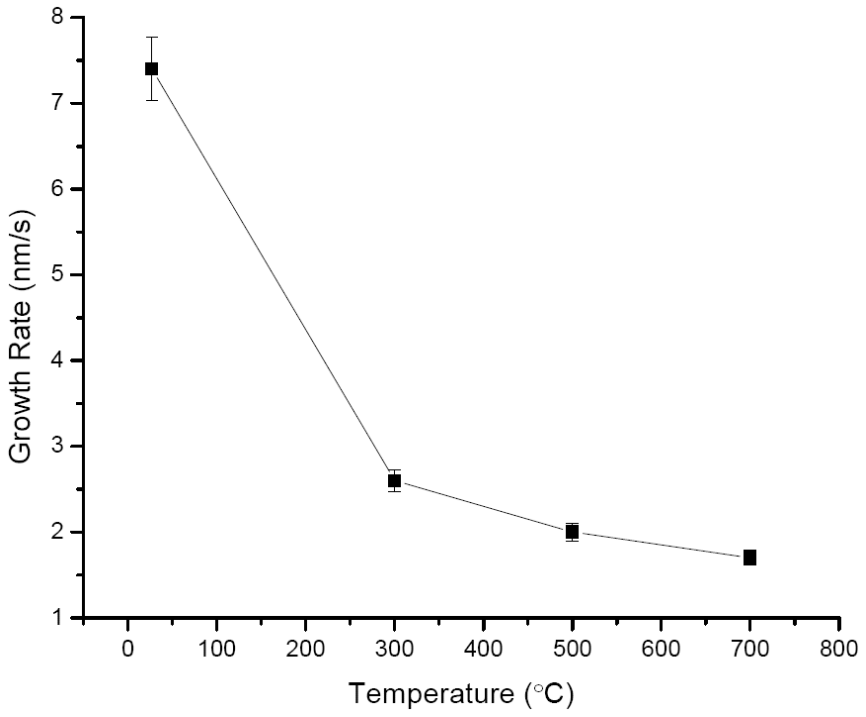

Fig.5.4. Film growth rate vs. deposition temperature

Figure 5.5 shows the high magnification cross section TEM images of the films deposited at all four temperatures. As can be verified from the Fig. 5.5a - d, at low substrate temperature film grew as poly crystalline and the growth mechanism changes to textured film growth at 300 ºC. From figure 4c and d, we can observe the highly epitaxial films grown on YSZ substrates. It is interesting to note that the films are very dense and free from cracks, and pores even from the sample deposited at RT. The X-ray diffraction patterns enclosed in the figures also evidence the actual microstructures and orientations of the films. The crystallinity of the films has been found to increase with increasing substrate temperature.

5.5 Summary

We have successfully processed fully dense thin film CGO electrolyte with different grain size. The crystallinity of the films has been found to increase with increasing substrate temperature. CGO thin film deposited above 500 ºC starts to show epitaxial growth on YSZ substrates. This dense CGO thin layer can increase gas tightness and can decrease the interface charge transfer resistance by decreasing grain boundary size. Hence lower total interface resistance between the electrolyte and cathode/anode layers. The present study suggests that substrate temperature significantly influences the microstructure of the films especially film grain size, and appropriate selections of the process parameters are required to achieve CGO films with desired properties for high efficiency SOFC applications.

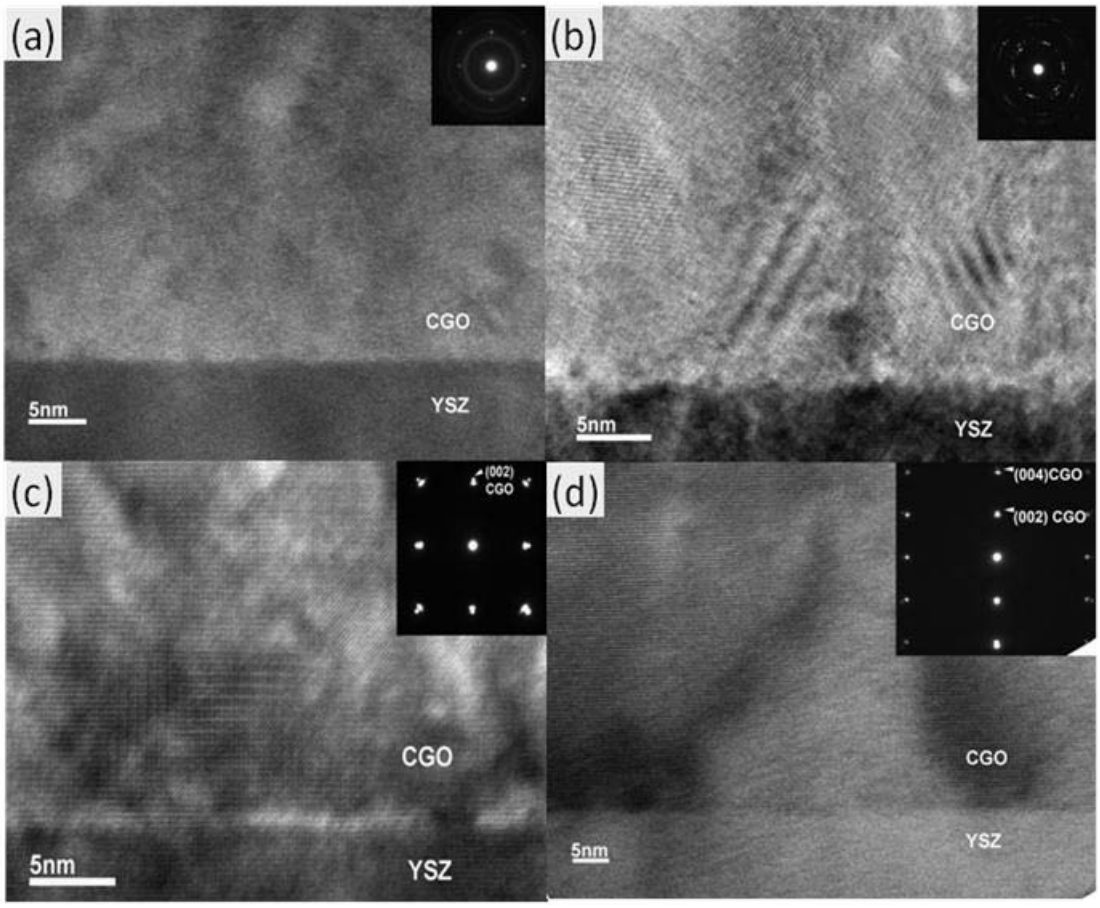

Fig.5.5. High magnification crossection TEM images of CGO thin films deposited at (a) RT, (b) 300 ºC, (c) 500 ºC, and (d) 700 ºC

CHAPTER VI

SUMMARY

The following list summarizes:

VANP: We have successfully processed nanostructured LSCO and LSCFO cathode thin films for thin film SOFC. All the films grow as columnar grains, which leaves nanopores in between the grains. The unique VANP structures in these cathode thin films penetrate throughout the film thickness as deep as 2 μm and produce enhanced oxygen conductance in the cathode layer. Additionally impedance measurements demonstrate that the cathode thin films with VANPs have low polarization resistance values and enhanced kinetic performance in the low temperature regime (400–700 °C).

VAN: We have successfully grown binary VAN interlayer of $(LSCO)_{0.5}$ $(CGO)_{0.5}$ in between the cathode and electrolyte for high efficiency thin film SOFC. This unique binary VAN structured interlayer effectively increases the cathode/electrolyte interface area density (by 14~25 times depending on the interlayer thickness) and thus significantly lowers the polarization resistance present at the cathode/electrolyte interface. Hence a low cathode polarization resistance ($9x10^{-4}$ Ω at 599°C, 2.39 Ω at 400°C) was achieved at low operation temperatures based on the impedance measurements at low temperature regime (400~600 ºC). The interface area density can be systematically controlled by varying the VAN interlayer thickness and column width, which can be achieved through tuning the deposition parameters. As the VAN thickness

increases, the ASR shifts to lower values. By combining a CGO seed layer with the VAN interlayer, we have demonstrated a record low ASR (4.84 $x10^{-4}$ Ωcm^2 at 599^oC, 1.25 Ωcm^2 at 400^oC).

Electrolyte: We have successfully processed fully dense thin film CGO electrolyte with different grain size. The crystallinity of the films has been found to increase with increasing substrate temperature. CGO thin film deposited above 500 ºC starts to show epitaxial growth on YSZ substrates. This dense CGO thin layer can increase gas tightness and can decrease the interface charge transfer resistance by decreasing grain boundary size. Hence lower total interface resistance between the electrolyte and cathode/anode layers. The present study suggests that substrate temperature significantly influences the microstructure of the films especially film grain size, and appropriate selections of the process parameters are required to achieve CGO films with desired properties for high efficiency SOFC applications.

REFERENCES

[1] Nat. Oceanic and Atmos. Admin. Clim. of 2001; Ann. Rev. (http://lwf.ncdc.noaa.gov/oa/climate/research/2001/preann2001/preann2001.html).

[2] Nat. Center for Atmos. Res. News release (2001) O259.

[3] Energy Information Agency (EIA). (2001) (http://www.allbusiness.com/utilities/392265-1.html).

[4] A.B. Stambouli, E. Traversa, Renew. and Sustainable Eng. Rev. 6 (2002) 433.

[5] US Dept. of Eng. Ann. Rev. of Eng. and Envrmnt V.26 (2001) 213.

[6] W.R. Grove, Philos Mag. 14 (1839) 127.

[7] W. Z. Nerst, Electrochem. 6 (1899) 41.

[8] J.J. Bezian, Centre d'Energetique de l'Ecole des Mines de Paris (1998) 44.

[9] Data from The InterNat. Fuel Cells, a United Tech. Company. Fuel Cells Rev. (2000) 543.

[10] E. Baur, H.Z. Preis, Electrochem. 43 (1937) 727.

[11] Nat. Museum of Am. Hist., Behring Center, Smithsonian Ins. Science History (2001) (http://www.si.edu/ofg/Units/sorsnmah.htm).

[12] US Dept. of Eng., Office of Fossil Eng. (2002) (http://www.fossil.energy.gov/programs/powersystems/fuelcells/fuelcells_solidoxide.html).

[13] Q.M. Nguyen, J. Am. Ceram. Soc. 76(3) (1993) 563.

[14] N. Q. Minh, J. Am. Ceram. Soc. 76 (1993) 563.

[15] S. S. Liou, W. L. Worrell, Appl. Phys. A, 49 (1989) 25.

[16] M. Kertesz, I. Riess, D. S. Tannhauser, R. Langpape, F. J. Rohr, J. Sol. State Chem. 42 (1982) 125.

[17] O. Yamamoto, Y. Takeda, R. Kanno, M. Noda, Solid State Ionics 22 (1987) 241.

[18] Y. Ohno, S. Nagata, H. Sato, Solid State Ionics 3 (1981) 439.

[19] J. Mizusaki, Y. Mima, S. Yamauchi, K. Fueki, H. Tagawa, J. Solid State Chem. 80 (1989) 102.

[20] J. Mizusaki, J. Tabuchi, T. Matsuura, S. Yamauchi, K. Fueki, J. Electrochem. Soc. 136 (1989) 2082.

[21] Nextech Mater., Fuel Cell Mater. (2001) 256.

[22] E. S. Putna, J. Stubenrauch, J. M. Vohs, R. J. Gorte, Langmuir 11 (1995) 4832.

[23] J. T. S. Irvine, D. P. Fagg, J. Labrincha, F. M. B. Marques, Catal. Today 38 (1997) 467.

[24] E. P. Murray, T. Tsai, Nature 400 (1999) 649.

[25] S. Park, R. Craciun, V. Radu, R. J. Gorte, J. Electrochem. Soc. 146 (1999) 3603.

[26] B.C.H. Steele, A. Heinzel, Nature 414 (2001) 345.

[27] X. Chen, N.J. Wu, Z. H. Zhang, A. Ignatiev, Thin Solid Films 350(1-2) (1999) 1 30.

[28] C.C Sun, E.W. Hawk, E.F. Sverdrup, J. Electrochem. Soc. 119 (1972) 1433.

[29] G.F. Carini, H.U. Anderson, D.M. Aparlin, M.M. Nasrallah, Solid State Ionics 49 (1991) 233.

[30] R. Brawn, Rept. from the Solar Eng. Lab., Renewable and Sustainable Energy Reviews, 6 (2002) 433.

[31] A.J. Mc Evoy, Lab. de Photonique et des Interfaces. Ecole Polytechnique Fe´derale de Lausanne, Fuel cell tech. stat. and prosp. (1998) 154-158 (http://sel@sel.me.wisc.edu/).

[32] Global Thermoelectric Inc. Ann. Rept. (2001) 32-37 (http://www.globalte.com /pdf/ar.pdf).

[33] Mater. Sci. and Res. Inc. 2000 Fuel Cell Seminar, Portland, OR. (2000) 212.

[34] California Energy Commission. (2001) 286 (http://www.accessmylibrary.com/ coms2/summary_0286-10717979_ITM).

[35] S. A. Boudghene, E. Traversa, Proc. of the Premier Seminaire (2001) 631.

[36] D. B. Chrisey, G. K. Hubler, Pulsed Laser Deposition, Wiley-InterSci., New York (1994) 5.

[37] R. K. Singh, D. H. Lowndes, D. B. Chrisey, E. Fogarassy, J. Narayan, Mater. Res. Soc. 526 (1998) 47.

[38] J. E. Mahan, Wiley-InterSci., New York (2000) 133-151.

[39] R. K. Singh, J. Narayan, A. K. Singh, J. Krishnawmy, Appl. Phys. Lett. 54 (1989) 2271.

[40] R. K. Singh, O. W. Holland, J. Narayan, J. Appl. Phys. 68 (1) (1990) 233.

[41] R. K. Singh, J. Narayan, Phys. Rev. B. 41 (13) (1990) 8843.

[42] B. D. Cullity, Elements of X-Ray Diffr., Addison-Wesley, Inc. MA (1982).

[43] L. Azaroff, R. Kaplow, N. Kato, R. Weiss, A. Wilson, R. Young, X-ray Diffr., McGraw-Hill, Inc. New York (1974).

[44] D. B. Williams, Pract. Anal. Elec. Microsc. in Mater. Sci., Philips Elec. Ic. Instrum., Inc. Elec. Opt. Publishing Group, New York (1984).

[45] D. B. Williams, and C. B. Carter, Trans. Elec. Microsc., Plenum Press, New York (1996).

[46] J. Spence, Exp.al High Resolut. Elec. Microsc., Oxford Univ. Press, New York (1988).

[47] J. W. Eddington, Pract. Elec. Microsc. in Mater. Sci., V.11 (1976) 133.

[48] S.J. Pennycook, D.E. Jesson, UltraMicrosc. 37 (1991) 14.

[49] D.B. Williams, C.B. Carter, Trans. Elec. Microsc., Plenum Press, New York (1996) 22.

[50] C.E. Hall, Intro. to Elec. Microsc., McGraw Hill, New York (1953) 229.

[51] L.M. Brown, J. Yuan, N.D. Browning, S.J. Pennycook, Char. of High Tc (Tc: Critical Temperature) Mater. and Dev. by Elec. Microsc., Cambridge Univ. Press, Cambridge (2000) 40

[52] D.B. Williams, C.B. Carter, Trans. Elec. Microsc., Plenum Press, New York (1996) 147.

[53] D.B. Williams, C.B. Carter, C. B, Trans. Elec. Microsc., Plenum Press, New York (1996) 79.

[54] R. W. Carpenter, Elec. Microsc. in Mater. Sci, (Ed. P. G. Merli) 315 (1991) 81.

[55] N.D. Browning, S.J. Pennycook, J. Microsc. 180 (1995) 230.

[56] M. Haider, J. Zach, Elec. Microsc. 1 (1998) 53.

[57] O. L. Krivanek, N. Dellby, A. J. Spence, L. M. Brown, Elec. Microsc. 1 (1998) 55.

[58] A. R. Lupini, O. L. Krivanek, Elec. Microsc. 1 (1998) 59.

[59] D.B. Williams, C.B. Carter, Trans. Elec. Microsc., Plenum Press, New York (1996) 359.

[60] H. Yokokawa, N. Sakai, T. Horita, K. Yamaji, M.E. Brito, H. Kishimoto, J. Alloys Compd. 433 (2007) 193.

[61] B. Butz, P. Kruse, H. St¨ormer, D. Gerthsen, A. M¨uller, A. Weber, E. Ivers-Tiff´ee, Solid State Ionics 177 (2006) 3275.

[62] D. Larrain, J. V. Herle, D. Favrat, J. Power Sources 161 (2006) 392.

[63] J.R. Macdonald, Impedance Spectrosc.—Emphasizing Solid Mater. and Sys., John Wiley & Sons, New York (1987).

[64] J.R. Macdonald, Impedance Spectrosc.—Theory Exp. and Appl., John Wiley & Sons, New York (2005).

[65] Z. Stoynov, D. Vladikova, Differ. Impedance Anal., Marin Drinov Acad. Publishing House, Sofia (2005).

[66] Z. Stoynov, B. Grafov, B. S. Stoynova, V. Elkin, Electrochem. Impedance, Publishing House “Nauka”, Moscow (1991).

[67] A. Lasia, in: B.E. Conway, J. Bockris, R. White (Eds.), Electrochem. Impedance Spectrosc. and its Appl.-Modern Aspects of Electrochem., Kluwer Acad., Plenum Publishers, New York, vol. 32 (1999).

[68] C. Gabrielli, Ident. of Electrochem. Processes by Freq. Response Anal. Tech. Rept. 004/83 (1998).

[69] C. Gabrielli, Use and Appl. of Electrochem. Impedance Tech., Tech. Rept. 24 (1997).

[70] A. Barbucci, P. Carpanese, G. Gerisola, M. Viviani, Solid State Ionics 176 (2005) 1753.

[71] K. Huang, J. Electrochem. Soc. 151 (5) (2004) A716.

[72] K. Huang, J. Electrochem. Soc. 151 (5) (2004) H117.

[73] J.W. Kim, A.V. Virkar, K.Z. Fung, K. Mehta, S.C. Singhal, J. Electrochem. Soc. 146 (1) (1999) 69.

[74] A.V. Virkar, J. Chen, C.W. Tanner, J.W. Kim, Solid State Ionics 131 (1–2) (2000) 189.

[75] S.H. Chan, K.A. Khor, Z.T. Xia, J. Power Sources 93 (2001) 130.

[76] S.H. Chan, Z.T. Xia, J. Appl. Electrochem. 32 (2002) 339.

[77] J. Bard, L.R. Faulkner, Electrochem. Methods—Fundam. and Appls., John Wiley & Sons, New York (2001).

[78] J.W. White, Proc. IEEE 59 (1971) 98.

[79] J.W. White, Proc. of the 6th Ann. Princeton Conf. on Inf. Sci. and Sys. (1972) 173.

[80] R. de, L. Kronig, J. Opt. Soc. Am. 12 (1926) 547.

[81] H.A. Kramers, Z. Phys. 30 (1929) 521.

[82] H.W. Bode, Network Anal. and Feedback Amp. Des. (1945) Chapter 14.

[83] Z. Stoynov, Electrochim. Acta 38 (1993) 1919.

[84] K. Darowicki, J. Electroanal. Chem. 486 (2000) 101.

[85] K. Darowicki, J. Orlikowski, G. Lentka, J. Electroanal. Chem. 486 (2000) 106.

[86] S. Rosvall, M. Honeychurch, D. Elton, A. Bond, J. Electroanal. Chem. 515 (2001) 8.

[87] K. Darowicki, P. ´ Slepski, Electrochim. Acta 49 (2004) 763.

[88] K. Darowicki, Corros. Sci. 37 (1995) 913.

[89] J.R. Wilson, D.T. Schwartz, S.B. Adler, Electrochim. Acta 51 (2006) 1389.

[90] J.R. Macdonald, D.R. Franceschetti, J. Chem. Phys. 68 (1978) 1614.

[91] M. Nagata, Y. Itoh, H. Iwahara, Solid State Ionics 67 (1994) 215.

[92] S.B. Adler, J. Electrochem. Soc. 149 (2002) E166.

[93] G. Hsieh, S.J. Ford, T.O. Mason, L.R. Pederson, Solid State Ionics 91(1996) 191.

[94] G. Hsieh, T.O. Mason, L.R. Pederson, Solid State Ionics 91 (1996) 203.

[95] G. Hsieh, T.O. Mason, E.J. Garboczi, L.R. Pederson, Solid State Ionics 96 (1997) 153.

[96] G. Hsieh, S.J. Ford, T.O. Mason, L.R. Pederson, Solid State Ionics 100 (1997) 297.

[97] F.P.F.V. Berkel, F.H.V. Heuneln, J.P.P. Huijamans, Solid State Ionics 72 (1994) 240.

[98] G.W. Walter, J. Electroanal. Chem. 118 (1981) 259.

[99] G.W. Walter, Corros. Sci. 26 (1986) 681.

[100] Gamry Instrum., Electrochem. Impedance Spectrosc. Theory: A Primer, (http://www.gamry.com/App Notes/EIS Primer/EIS Primer.htm), (1997–2005).

[101] J.D. Kim, G.D. Kim, J.W. Moon, Y. Park, W.H. Lee, K. Kobayashi, M. Nagai, C.E. Kim, Solid State Ionics 143 (2001) 379.

[102] S.Z. Wang, Y. Jiang, Y.H. Zhang, J.W. Yan, W.Z. Li, Solid State Ionics 115 (1998) 291.

[103] E.P. Murray, T. Tsai, S.A. Barnett, Solid State Ionics 110 (1998) 235.

[104] J.P. Diard, B. Le Gorrec, C. Montella, J. Electroanal. Chem. 205 (1986) 77.

[105] J.P. Diard, P. Landaud, B. Le Gorrec, C. Montella, J. Electroanal. Chem. 352 (1993) 1.

[106] J.P. Diard, B. Le Gorrec, C. Montella, J. Electroanal. Chem. 326 (1992) 13.

[107] J.P. Diard, B. Le Gorrec, C. Montella, C. Montero-Ocampo, J. Electroanal. Chem. 352 (1993) 1.

[108] J.I. Gazzarri, O. Kesler, J. Power Sources 167 (2007) 100.

[109] J.I. Gazzarri, O. Kesler, J. Power Sources 167 (2007) 430.

[110] A. Barbucci, R. Bozzo, G. Gerisola, P. Costamagna, Electrochem. Acta 47 (2002) 2183.

[111] A. Barbucci, M. Viviani, P. Carpanese, D. Vladikova, Z. Stoynov, Electrochim. Acta 51 (2006) 1641.

[112] T. Kato, K. Nozaki, A. Negishi, K. Kato, A. Momma, Y. Kaga, S. Nagata, K. Takano, T. Inagaki, H. Yoshida, K. Hosoi, K. Hoshino, T. Akbay, J. Akikusa, J. Power Sources 133 (2004) 169.

[113] A. Liliya, Y.X. Dunyushkina, S.B. Lu, Adlera, J. Electrochem. Soc. 152 (2005) A1668.

[114] H. Kuboyama, T. Shoho, M. Matsunaga, Electrochem. Proc. 97 (1997) 404.

[115] T. Kato, K. Nozaki, A. Negishi, K. Kato, A. Momma, Y. Kaga, S. Nagata, K. Takano, T. Inagaki, H. Yoshida, et al., J. Power Sources 133 (2004) 169.

[116] S.J. Skinner, Int. J. Inorg. Mater. 3 (2001) 113.

[117] B.C.H. Steele, J. Mater. Sci. 36 (2001) 1053.

[118] J.M. Ralph, A.C. Schoeler, M. Krumpelt, J. Mater. Sci. 36 (2001) 1161.

[119] Y. Teraoka, T. Nobunaga, N. Yamazoe, Chem. Lett. (1988) 503.

[120] Y. Teraoka, H.M. Zhang, K. Okamoto, N. Yamazoe, Mater. Res. Bull. 23 (1988) 51.

[121] Y. Matsumoto, S. Yamada, T. Nishida, E. Sato, J. Electrochem. Soc. 127 (1999) 2360.

[122] A. Petric, P. Huang, F. Tietz, Solid State Ion. 135 (2000) 719.

[123] J. Fleig, J. Power Sources 105 (2002) 228.

[124] P.B. Barna, M. Adamik, Thin Solid Films 317 (1998) 27.

[125] I. Petrov, P.B. Barna, L. Hultman, J.E. Greene, J. Vac. Sci. Technol. A21 (5) (2003) 5117.

[126] S. Mahieu, et al. Thin Solid Films 515 (4) (2006) 1229.

[127] B.A. Movchan, A.V. Demchishin, Phys. Met. Mettalogr. 28 (1969) 83.

[128] J.A. Thornton, J. Vac. Sci. Technol. 11 (4) (1974) 666.

[129] V. Dusastre, J.A. Kilner, Solid State Ion. 126 (1999) 163.

[130] E.P. Murray, M.J. Sever, S.A. Barnett, Solid State Ion. 148 (2002) 148.

[131] L. Baque, A. Serquis, N.Grunbaum, F. Prado, A. Caneiro, Mat. Ges. Soc. Symp, Proc. 928 (2006), 16.

[132] N. Grunbaum, et al. Solid state Ion. 177 (2006) 907.

[133] M. Kleitz, T. Kloidt, L. Dessemond, (1993) 89.

[134] S.B. Adler, Chem. Rev. 104 (2004) 479.

[135] H. Apfel, et al. J. Power Sources 154 (2) (2006) 370.

[136] B. Kenney, K. Karan, Solid State Ionics 178 (3-4) (2007) 297.

[137] M.H. Hung, M.V.M. Rao, D.S. Tsai, Mater. Chem. Phys. 101 (2-3) (2007) 297.

[138] J. Deseure, et al. J. Appl. Electrochem. 37 (1) (2007) 129.

[139] M. Sase, et al. Solid State Ionics 177 (19-25) (2006) 1961.

[140] E. Koep, et al. J. Power Sources 161 (1) (2006) 250.

[141] S.P. Yoon, et al. J. Power Sources 136 (1) (2004) 30.

[142] J. Yoon, et al. Appl. Surf. Sci. 254 (1) (2007) 266.

[143] B.S. Kang, et al. Appl. Phys. Lett. 88 (19) (2006).

[144] J.L. MaCmanus-Driscoll, et al. Nat. Mater. 7 (4) (2008) 314.

[145] Z. Bi, J. Lee and H. Wang, in preparation for Appl. Phys. Lett. (2008)

[146] A.O. Stoermer, J.L.M. Rupp, L.J. Gauckler, Solid State Ionics 177 (19-25) (2006) 2075.

[147] B.C.H. Steele, Solid State Ionics 129 (1-4) (2000) 95.

[148] C.R. Doshi, V.I. Richards, J.D. Cartex, X.P. Way, M. Krumpett, J Electrochem. Soc. 146(4) (1999) 1273.

[149] B.C.H. Steel, Solid State Ion 129(1–4) (2000) 95.

[150] S. de Souza, S.J. Visco, L.C. de Jonghe, Solid State Ionics 98 (1997) 57.

[151] J.W. Kim, A.V. Virkar, K.Z. Fung, K. Mehta, S.C. Singhal, J. Electrochem. Soc. 146 (1999) 69.

[152] J. Will, A. Mitterdorfer, C. Kleinlongel, D. Perednis, L.J. Gauckler, Solid State Ionics 131 (2000) 79.

[153] R. Maric, S. Ohara, T. Fukui, H. Yoshida, M. Nishimura, T. Inagaki, K. Miura, J. Electrochem. Soc. 146 (1999) 2006.

[154] T. Ishihara, T. Shibayama, M. Honda, H. Nishiguchi, Y. Takita, J. Electrochem. Soc. 147 (2000) 1332.

[155] K. Wang, J.H. Wan, J.B. Goodenough, J. Electrochem. Soc. 148 (2001) A788.

[156] J.W. Yan, Z.G. Lu, Y. Jiang, Y.L. Dong, C.Y. Yu, W.Z. Li, J. Electrochem. Soc.149 (2002) A1132.

[157] R. Doshi, V.L. Richards, J.D. Carter, X. Wang, M. Krumpelt, J. Electrochem. Soc. 146 (1999) 1273.

[158] C. Xia, F. Chen, M. Liu, Electrochem. Solid-State Lett. 4 (2001) A52.

[159] S.P. Jiang, Y.J. Leng, S.H. Chan, K.A. Khor, Electrochem. Solid-State Lett. 6 (2003) A67.

[160] E.P. Murray, M.J. Sever, S.A. Barnett, Solid State Ionics 148 (2002) 27.

[161] V. Dusastre, J.A. Kilner, Solid State Ionics 126 (1999) 163.

[162] C. Xia, M. Liu, Adv. Mater. 14 (2002) 521.

[163] T. Ishihara, K. Sato, Y. Takita, J. Am. Ceram. Soc. 79 (1996) 913.

[164] J.A. Kilner, Solid State Ion 129 (2000) 13.

[165] J.A. Kilner, R.J. Brook, Solid State Ionics 6(3) (1982) 237.

[166] F. Kroger, H.J. Vink, F. Seitz, D. Turnbull(eds), Solid State Phys., Academic Press, New York (1965).

VITA

Name: Jongsik Yoon

Address: Department of Electrical and Computer Engineering,
Texas A&M University,
706 Jack E. Brown Engineering Bld.,
College Station, TX 77843

Email Address: jsyoon@tamu.edu

Education: B.S., Chemistry, Yonsei University, Korea 1999
M.S., Electrical Engineering, University of Southern California, 2004
Ph.D., Electrical and Computer Engineering, Texas A&M University, 2008

This dissertation was typed by the author.